NRC·CNRC
Canadian
Neutron Beam
Centre

CNRC·NRC
Centre canadien
de faisceaux
de neutrons


# ANNUAL REPORT 2007 RAPPORT ANNUEL

NRC Canadian Neutron Beam Centre
Centre canadien de faisceaux de neutrons du CNRC

National Research Council Canada
Conseil national de recherches Canada

Canada

**National Research Council Canada**
**Canadian Neutron Beam Centre**
**2007 Annual Report to the Canadian Institute for Neutron Scattering**

**Conseil national de recherches Canada**
**Centre canadien de faisceaux de neutrons**
**Rapport annuel 2007 à l'Institut canadien de la diffusion des neutrons**

**http://neutron.nrc-cnrc.gc.ca**

Tel: 1 613 584-8297 ▪ Fax: 1 613 584-4040
Building 459, Station 18, Chalk River Laboratories
Chalk River, Ontario, CANADA K0J 1J0

Tél. : 1 613 584-8297 ▪ Téléc. : 1 613 584-4040
Bâtiment 459, Station 18, Laboratoires de Chalk River
Chalk River (Ontario) CANADA K0J 1J0



The information in this report, which describes the research activities and organization of NRC, is presented in English and French The scientific reports from our community of international users are presented in the language in which they were written.

Les renseignements contenus dans ce rapport, décrivant les activités de recherche et l'organisation du CNRC, sont présentés en anglais et en français. Les rapports scientifiques de notre communauté d'utilisateurs internationaux sont présentés dans la langue dans laquelle ils ont été écrits.

Disclaimer: The experimental reports contained in this document were not subjected to a formal peer review.

Avertissement : Les rapports d'expériences contenus dans le présent document n'ont pas été soumis à un examen formel par des pairs.



## Table of Contents



## Table des matières



John Root,
Director
NRC Canadian
Neutron Beam Centre

John Root, directeur
Centre canadien de faisceaux
de neutrons du CNRC

# Welcome

to the NRC Canadian Neutron Beam Centre (CNBC)

We enable researchers in universities, industries and government laboratories to exploit innovative neutron beam instruments and methods for world-class materials research and education. We also provide leadership to revitalize Canada's capacity for neutron-based science and industry in the coming decades.

# Bienvenue

au Centre canadien de faisceaux de neutrons du CNRC (CCFN)

Nous permettons à des chercheurs de laboratoires universitaires, industriels et gouvernementaux d'exploiter des instruments innovateurs à faisceaux de neutrons et des méthodes pour la recherche sur les matériaux de classe internationale et pour l'éducation. Nous assumons aussi le leadership en matière de revitalisation de la capacité canadienne scientifique et industrielle des prochaines décennies fondée sur les neutrons.

**The** CNBC is managed by the National Research Council Canada (NRC), an agency of the Canadian government, and overseen by the Canadian Institute for Neutron Scattering (CINS), a 400-member organization of neutron-beam users from across Canada and around the world. We are located inside Chalk River Laboratories, which are owned and operated by Atomic Energy of Canada Limited (AECL). This is the home of the NRU reactor, a 120 MW, multipurpose neutron source for neutron beam research, isotope production and the support of Canada's nuclear power technology.

The CNBC is funded from three major sources. In the past fiscal year (April 2007 – March 2008), NRC contributed about 60% of funding, allowing us to maintain a steady foundation of neutron scattering expertise and infrastructure for national strategic goals, including Canadian participation in a global network of major science facilities. Secondly, the Natural Sciences and Engineering Research Council (NSERC) provided about 30% of our funding through a Major Resource Support (MRS) grant, which was administered by McGill University on behalf of the Canadian academic community. This support helped to ensure that the laboratory was maintained in a competitive condition for access by university researchers and students, helping to develop highly qualified personnel. Thirdly, industry clients paid the full cost of accessing our neutron facilities to obtain proprietary information for their businesses.

In 2007, the NRU reactor operated for 253 days and during 87% of this time, the CNBC neutron beam instruments were occupied by the projects of users who came from Canadian universities, foreign institutions, government laboratories or industry. The remaining 13% of beam time was occupied by CNBC-driven projects to develop innovative neutron scattering methods, novel applications to new areas of science, or to contribute to research at the cutting edge of condensed matter science. In all, 114 experiments were completed in the last year, seven of which were associated with five proprietary projects. The public-domain projects involved 75 individual researchers, and supported research from 33 university departments spread among 20 universities in five Canadian provinces (British Columbia, Alberta, Manitoba, Ontario and Quebec). About 16% of beam time was occupied by research projects of foreign institutions in 11 countries (Armenia, Belgium, Germany, Italy, Japan, the Netherlands, Russia, Sweden, Switzerland, the United Kingdom and the United States). There were 42 students who accessed the CNBC for purposes of research and education.

**Le** CCFN est géré par le Conseil national de recherches Canada (CRNC), agence gouvernementale du Canada, et supervisé par l'Institut canadien de la diffusion des neutrons (ICDN), organisme de 400 membres utilisateurs des faisceaux de neutrons provenant du Canada et de l'étranger. Nous sommes situés dans les laboratoires de Chalk River appartenant à Énergie atomique du Canada limitée (EACL) qui les exploite. C'est l'endroit où se trouve le réacteur NRU, source de neutrons polyvalente de 120 MW destinée à la recherche avec des faisceaux de neutrons, à la production d'isotopes et au soutien technologique des centrales nucléaires du Canada.

Le CCFN est financé par trois principales sources. Durant le dernier exercice financier (d'avril 2007 à mars 2008), le CNRC a contribué pour 60 % environ du financement, ce qui nous a permis de maintenir une expertise et une infrastructure en matière de diffusion des neutrons de base solides répondants aux objectifs stratégiques nationaux, y compris la participation canadienne à un réseau mondial d'installations scientifiques majeures. De plus, le Conseil de recherches en sciences naturelles et en génie (CRSNG) a fourni 30 % environ du financement par l'intermédiaire de la bourse d'accès aux installations majeures (Major Facilities Access) qui est administrée par l'université McGill pour le compte de la communauté universitaire canadienne. Ce soutien permet d'assurer au laboratoire une situation concurrentielle quant à l'accès des chercheurs universitaires et des étudiants, ce qui permet de former du personnel hautement qualifié. Enfin, les clients provenant de l'industrie ont remboursé les coûts totaux liés à leur accès aux installations de neutrons pour obtenir des données exclusives pertinentes à leurs entreprises.

En 2007, le réacteur NRU a été exploité pendant 253 jours et, pendant 87 % de ce temps, les instruments de faisceaux de neutrons du CCFN ont été occupés par les projets d'utilisateurs provenant d'universités canadiennes, d'institutions étrangères, de laboratoires gouvernementaux ou de l'industrie. Les 13 % restant du temps de faisceau ont été occupés par des projets propres au CCFN dans le but de mettre au point des méthodes innovatrices de diffusion des neutrons, de développer de nouvelles applications dans d'autres domaines scientifiques ou pour contribuer à la recherche d'avant-garde sur la matière condensée. En tout, 114 expériences ont été effectuées la dernière année; 7 de celles-ci étaient associées à 5 projets exclusifs. Les projets du domaine public ont impliqué 75 chercheurs, et la recherche soutenue par 33 départements universitaires a impliqué 20 universités canadiennes de 5 provinces canadiennes (Colombie-Britannique, Alberta, Manitoba, Ontario et Québec). Environ 16 % du temps de faisceau a été occupé par des projets de recherche d'institutions étrangères de 11 pays (Arménie, Belgique, Allemagne, Italie, Japon, Pays-Bas, Russie, Suède, Suisse, Royaume-Unis et États-Unis). 42 étudiants ont accédé au CCFN à des fins de recherche et d'éducation.

This 2007 annual report includes reports from our users, representing a cross-section of the experiments conducted in 2007. This report also includes a list of publications from 2007, based on research conducted at the CNBC, where CNBC staff members were included as co-authors. In the introductory pages of this report, we highlight CNBC news and accomplishments within the more recent reporting period, April 2007 to March 2008. We are very pleased to note the award of an honorary degree, Doctor of Science, by the University of Aberdeen to Dr. Bill Buyers, recognising his distinguished career in condensed matter physics. Also, we note the production of the Canadian Institute for Neutron Scattering's (CINS) "Plan to 2050 for materials research with neutron beams in Canada." This plan envisions a new Canadian Neutron Centre (CNC) as the centrepiece of the future of materials science in Canada, and as a critical resource to advance Canada's goals in science and technology.

## Our overarching issue and concern remains the long-term prospect of Canada's neutron source.

The NRU reactor at Chalk River has served Canada since 1957, generating medical isotopes, providing a test facility for components and materials for nuclear power generation, and producing thermal neutron beams for advanced materials research.

Over the last several years, AECL has invested considerable resources to upgrade the safety systems of the NRU reactor, which is currently licensed for continued operation until the end of 2011. Further investment and extensions of the license will be needed to allow for some overlap of operation until a replacement facility – the CNC – has been built and operated for an initial period. In the meantime, the CNBC will rejuvenate and expand its competencies in neutron scattering research, by building new neutron beam facilities, developing applications of neutron scattering to new areas of science and technology, and strengthening Canada's neutron user community.

John Root, Director
NRC CANADIAN NEUTRON BEAM CENTRE

Ce rapport annuel 2007 comporte des rapports provenant de nos utilisateurs et représentant un échantillon représentatif des expériences réalisées en 2007. Il comporte aussi une liste des publications de 2007 basée sur une recherche conduite au CCFN et dans lesquelles des membres du CCFN ont été inclus comme co-auteurs. Dans les pages d'introduction de ce rapport, nous soulignons les nouvelles et les réalisations du CCFN pendant la plus récente période du rapport, d'avril 2007 à mars 2008. Nous sommes heureux de mentionner que le docteur Bill Buyers a reçu une distinction honorifique de docteur en sciences de l'université d'Aberdeen en reconnaissance de sa carrière remarquable en physique de la matière condensée. En outre, nous soulignons la production du Plan canadien jusqu'en 2050 pour la recherche sur les matériaux avec des faisceaux de neutrons de l'Institut canadien de la diffusion des neutrons. Ce plan envisage un nouveau Centre canadien de neutrons (CCN) comme une pièce centrale canadienne destinée à la science des matériaux de l'avenir, et une ressource essentielle permettant d'atteindre les objectifs canadiens en matière de science et de technologie.

## Notre question et préoccupation dominantes restent la perspective à long terme d'une source canadienne de neutrons.

Le réacteur NRU de Chalk River dessert le Canada depuis 1957; il a permis de générer des isotopes médicaux, de fournir une installation d'essai pour des composants et des matériaux destinés à la production des centrales nucléaires, et de fournir des faisceaux de neutrons thermiques pour la recherche avancée sur les matériaux.

Pendant les dernières années, EACL a investi des ressources considérables pour mettre à niveau les dispositifs de sécurité du réacteur NRU qui a obtenu une licence de fonctionnement jusqu'en 2011. D'autres investissements et prolongations de la licence seront nécessaires pour permettre un certain chevauchement des opérations jusqu'à la construction et le fonctionnement pendant une période initiale d'une installation de rechange, le CCN. Pendant de temps, le CCFN rajeunira et étendra ses compétences en matière de recherche sur la diffusion des neutrons en construisant des installations de faisceaux de neutrons, développant des applications de la diffusion des neutrons à de nouveaux domaines scientifiques et technologiques, et en renforçant la communauté canadienne des utilisateurs des neutrons.

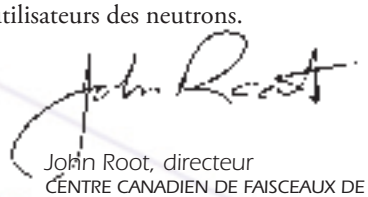

John Root, directeur
CENTRE CANADIEN DE FAISCEAUX DE NEUTRONS DU CNRC

Welcome to CNBC.
Our busy user program, which welcomes scientists from across Canada and around the world every year, is coordinated by the Centre's Administrative Manager, Niki Schrie.

**613-584-8293 ▪ Nicole.Schrie@nrc-cnrc.gc.ca**

Bienvenue au CCFN. Notre programme d'utilisateurs très fréquenté, qui accueille des scientifiques du Canada et du monde entier chaque année, est coordonné par la gestionnaire administrative du Centre, Niki Schrie.

The CNBC

# Neutrons at Work for Canada

The CNBC is a national science facility promoting Canada's federal goals for science and technology, including building our three Science and Technology (S&T) advantages: entrepreneurship, knowledge, and people.

Le CCFN

# Des neutrons au service du Canada

Le CCFN est une installation scientifique nationale qui favorise l'atteinte des objectifs du gouvernement canadien en matière de sciences et technologie, dont l'instauration de nos trois avantages en sciences et technologie : entrepreneuriat, savoir et humain.

## A National Science Facility

The NRC Canadian Neutron Beam Centre (CNBC), like other neutron scattering laboratories worldwide, is a unique and important part of our national infrastructure for science and industry. The CNBC is a major resource for researchers in many scientific disciplines from universities and laboratories in every province. During 2007, scientists from 33 departments of 20 Canadian universities in five provinces used the unique materials research capabilities of the CNBC to support their research programs. The CNBC's mission is aligned with Canada's goals for Science and Technology (S&T) as articulated in Canada's Federal S&T Strategy, which was released in May 2007.[1] These goals are to build Canada's S&T advantages in entrepreneurship, knowledge and people, using four core principles: promoting world-class excellence, focusing on priorities, fostering partnerships, and enhancing accountability.

## Building an Entrepreneurial Advantage

The CNBC builds Canada's entrepreneurial advantage by providing industry access to a facility that provides unique knowledge about materials, to enhance their business competitiveness. Among the international network of neutron scattering laboratories, CNBC is recognized as the world leader in enabling industry clients to investigate stresses in materials and components. Neutrons have some unique properties that make them an ideal probe for industrial research. They penetrate deeply into dense materials such as metals and alloys. They can probe material samples that are held in realistic conditions of pressure, temperature and stress. They are non-destructive; they do not damage the specimen under examination. Automotive, aerospace, power-generation, manufacturing and metal-producing industries have all benefited from access to neutron diffraction at the CNBC. The knowledge provided by neutron diffraction is unique and often leads to enhanced product reliability, greater safety margins, reduced costs of production or maintenance, or to open new markets for products – all contributing to industry competitiveness.

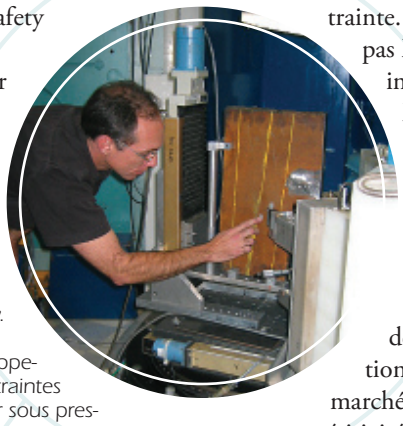

Rod McGregor, Defence Research and Development Canada Engineer, studying residual stress in a section of a pressure hull-plate removed from the submarine *HMCS Victoria*.

Rod McGregor, ingénieur Recherche et développement pour la défense Canada, étudiant les contraintes résiduelles dans une section de bordé extérieur sous pression prélévée sur le sous-marin NCSM Victoria.

## Une installation scientifique nationale

Le Centre canadien de faisceaux de neutrons (CCFN) du CNRC, comme d'autres laboratoires de diffusion des neutrons à travers le monde, est une composante unique et importante de notre infrastructure scientifique et industrielle nationale. Le CCFN est une ressource majeure utilisée par des chercheurs de nombreuses disciplines scientifiques provenant d'universités et de laboratoires de toutes les provinces du pays. En 2007, des scientifiques de 33 départements de 20 universités canadiennes de 5 provinces ont utilisé les installations de recherche sur les matériaux uniques du CCFN dans le cadre de leurs programmes de recherches. La mission du CCFN est alignée sur les objectifs canadiens en matière de science et de technologie (S et T) tels qu'ils sont structurés dans la Stratégie des sciences et de la technologie du gouvernement du Canada, qui a été dévoilée en mai 2007.[1] Ces objectifs visent à réaliser le potentiel des sciences et de la technologie au profit du Canada en matière d'entreprenariat, de savoir et de personnel grâce à la mise en œuvre de quatre principes de base : promotion de l'excellence de classe internationale, concentration des efforts sur les priorités, favoriser les partenariats et augmentation de la responsabilisation.

## Création de l'avantage entrepreneurial

Le CCFN produit un avantage entrepreneurial pour le Canada en permettant à l'industrie d'accéder à une installation procurant une connaissance unique sur les matériaux afin d'améliorer la compétitivité des entreprises. Parmi le réseau international de laboratoires de diffusion des neutrons, le CCFN est reconnu comme le leader mondial permettant à des clients venant de l'industrie d'étudier les contraintes qui s'exercent dans les matériaux et les composants. Les neutrons disposent de propriétés uniques qui en font une sonde idéale pour la recherche industrielle. Ils pénètrent profondément dans des matériaux denses, comme les métaux et les alliages. Ils permettent de sonder des échantillons de matériaux tenus dans des conditions réelles de pression, température et contrainte. Ils sont non destructifs; ils n'endommagent pas le spécimen en observation. Les secteurs industriels de l'automobile, de l'aérospatial, de la production d'électricité, de la fabrication et de la métallurgie bénéficient tous de l'accès à la diffraction des neutrons au CCFN. Les connaissances fournies par la diffraction des neutrons sont uniques et conduisent souvent à des améliorations de la fiabilité des produits, à l'augmentation des marges de sécurité, la réduction des coûts de fabrication ou d'entretien, ou à l'ouverture de nouveaux marchés pour les produits; tout cela contribue à la compétitivité des entreprises.

[1] Industry Canada. *Mobilizing Science & Technology to Canada's Advantage.* Industry Canada Site – Corporate Publications. [Online] 2007. [Cited: April 7, 2008.] www.ic.gc.ca/epublications.

[1] Industrie Canada. *Réaliser le potentiel des sciences et de la technologie au profit du Canada.* Site d'Industrie Canada – Publications sur le Ministère [En ligne] 2007. [Cité : 7 avril 2008.] www.ic.gc.ca/epublications. 2007.

Students learning to conduct an experiment using neutrons.

Étudiants apprenant à effectuer une expérience utilisant des neutrons.

## PARTNERSHIP IN FUNDING AND MISSION

There is a strong culture of partnership at the CNBC, encompassing an ongoing tradition of very strong science, supporting users, recognising the value of outreach and educating young scientists.

Funding to operate the CNBC is derived from three sources, reflecting various aspects of our mission in Canada or internationally, listed in order of support:

(1) NRC owns and operates the centre as a national science facility, available to researchers in universities, industries and government, and a centre of innovation for neutron instruments and methods. The facility helps to connect Canada to a global network of scientists who need neutron beams for materials research.

(2) NSERC funds people and programs in the Canadian university system. By partnering with the Canadian Institute for Neutron Scattering (CINS), which represents the Canadian neutron user community, the CNBC receives funds through the NSERC Major Resource Support (MRS) program. The focus of the NSERC MRS program is to facilitate the effective access of Canadian researchers to major regional, national or international experimental or thematic research resources by financially assisting these resources to remain in a state of readiness for researchers to access. The current MRS grant #236732-2007 "Canadian Neutron Beam Laboratory" covers a five-year term, ending on March 31, 2012.

(3) Industry clients pay the full cost of their access to our neutron facilities to obtain proprietary information to improve their products and services.

## PARTENARIAT DE FINANCEMENT ET DE MISSION

Au CCFN, il existe une solide culture de partenariat, portant sur une tradition toujours vivante d'une science très poussée, d'un soutien attentif apporté aux utilisateurs, de la valeur de l'accessibilité et de la formation des jeunes scientifiques..

Le financement de l'exploitation du CCFN est assuré par trois sources correspondant aux divers aspects de notre mission au Canada et sur la scène internationale. Les voici en ordre :

(1) Le CNRC est propriétaire du centre et l'exploite en tant qu'installation scientifique nationale ouverte aux chercheurs universitaires, de l'industrie et du gouvernement, et centre d'innovation en matière d'instruments et de méthodes neutroniques. L'installation aide à relier le Canada à un réseau mondial de scientifiques qui utilisent des faisceaux de neutrons pour leurs recherches sur les matériaux.

(2) Le CRSNG finance le personnel et les programmes du réseau universitaire canadien. En partenariat avec l'Institut canadien de la diffusion des neutrons (ICDN), qui représente la communauté canadienne des utilisateurs de neutrons, le CCFN reçoit des fonds par l'intermédiaire du programme de soutien aux installations majeures (MRS) du CRSNG. Le programme de soutien aux ressources majeures du CRSNG a pour objectif de faciliter l'accès efficace des chercheurs canadiens à des ressources de recherches expérimentales ou thématiques régionales, nationales ou internationales majeures en aidant financièrement celles-ci à demeurer en état de recevoir les chercheurs qui les utilisent. La bourse actuelle du MRS numéro 236732-2007 « Laboratoire de faisceau de neutrons canadiens » couvre une période de cinq ans se terminant le 31 mars 2012.

(3) Les clients provenant de l'industrie remboursent les coûts totaux liés à leur accès aux installations de neutrons pour obtenir des données exclusives pertinentes à leurs produits et services.

### *Building our Knowledge Advantage*

The CNBC builds Canada's knowledge advantage by enabling fundamental research and by connecting Canadian scientists to the international scientific community. Because neutrons can be used in research on a broad range of materials, the CNBC is a resource for research across many disciplines, such as physics, chemistry, earth science, life science, materials science and engineering. The CNBC makes contributions to research areas aligned with national priorities, such as hydrogen storage materials, nanotechnologies, nuclear safety and drug delivery materials for future clinical applications. There are about twenty neutron scattering laboratories worldwide, supporting a diverse international scientific community. The CNBC is an active participant in this community, hosting collaborative projects involving scientists from about 100 institutions in 20 countries, within a typical five-year period. As members of that international network, Canadian scientists are welcome at foreign neutron laboratories, benefiting from the complementary resources and knowledge of our international counterparts.

### *Création de l'avantage du savoir*

Le CCFN crée l'avantage du savoir du Canada en permettant la recherche fondamentale et en mettant les scientifiques canadiens en relation avec la communauté scientifique internationale. Les neutrons pouvant être utilisés en recherche sur une vaste gamme de matériaux, le CCFN constitue une ressource pour la recherche couvrant de nombreuses disciplines, comme la physique, la chimie, les sciences de la terre, la biologie, la science des matériaux et le génie. Le CCFN contribue dans des domaines de recherche correspondant aux priorités nationales, comme les matériaux de stockage de l'hydrogène, les nanotechnologies, la sûreté nucléaire et les matériaux de relargage de médicament pour de futures applications cliniques. Dans le monde, il existe environ vingt laboratoires de diffusion des neutrons, qui prennent en charge diverses recherches issues de la communauté scientifique internationale. Le CCFN est un participant actif au sein de cette communauté en accueillant habituellement pendant cinq ans des projets de collaboration impliquant des scientifiques provenant de 100 institutions environ de 20 pays. En tant que membres de ce réseau international, les scientifiques canadiens sont les bienvenus dans les laboratoires de neutrons étrangers et bénéficient des ressources et des connaissances complémentaires de nos contreparties internationales.

## Building our People Advantage

The CNBC builds Canada's people advantage by facilitating the training of highly qualified people. Neutrons are a unique probe for materials, often revealing information that is not accessible using other techniques, and therefore contributing to the novelty of research that is crucial for journal publications and thesis programs. Many undergraduate and graduate students as well as post-doctoral researchers visit CNBC for weeks or months to apply neutron instruments and methods to support their research programs. The students and scientists visiting the CNBC come from a broad range of disciplines, creating an environment that is highly creative and that stimulates multidisciplinary discussion and collaboration. The staff of the CNBC provides technical and professional support, supervision of experimental work, and guidance on data analysis and interpretation, as well as follow-up advice at the time of producing the final scientific output. Providing a resource for education and continuing as a resource for research careers is recognized as an essential element of the CNBC's mission in delivering value to Canada.


## World-Class Excellence

The CNBC is competitive on the world stage, illustrated by the number and quality of international scientists who are attracted to Canada for experiments at the CNBC. During 2007, scientists from Armenia, Belgium, Germany, Italy, Japan, the Netherlands, Russia, Sweden, Switzerland, the United Kingdom and the United States were involved in experiments at the CNBC. Some examples of leading researchers and institutions from outside Canada that have recently collaborated with CNBC staff or used CNBC beamtime include Robert J. Birgeneau, Chancellor of the University of California at Berkeley and Collin Broholm from The John Hopkins University, for the study of spin dynamics and phase transitions in superconducting materials; Roger A. Cowley, Emeritus Professor, Oxford University, for the study of quantum fluctuations such as the decay of spin waves in superconducting materials; and Oak Ridge National Laboratory (ORNL) for the development of neutron instruments: Chris Tulk came to the CNBC to test equipment design and components for the development of a Spallation Neutrons and Pressure diffractometer for the Spallation Neutron Source, an instrument for the study of materials under very high pressures. Gene Ice came to the CNBC to show that Kirkpatrick–Baez neutron supermirrors can be used effectively for neutron scattering experiments, a crucial step in developing a polychromatic Laue microbeam diffractometer. The CNBC's competitiveness on the world stage is also illustrated by its high citation rates

## Création de l'avantage humain

Le CCFN créée l'avantage humain du Canada en facilitant la formation de personnes hautement qualifiées. Les neutrons constituent un outil de détection unique pour les matériaux, fournissant souvent des données impossibles à obtenir avec d'autres techniques; ils contribuent ainsi à l'originalité de la recherche, ce qui est essentiel pour les journaux spécialisés et les programmes de thèses. De nombreux étudiants de premier et de deuxième cycles, ainsi que des chercheurs postdoctoraux se rendent au CCFN et y restent pendant des semaines et des mois pour utiliser des instruments neutroniques et des méthodes dans le cadre de leurs programmes de recherche. Les étudiants et les scientifiques invités au CCFN proviennent d'une vaste gamme de disciplines et créent un environnement hautement créatif tout en stimulant les échanges et les collaborations multidisciplinaires. Le personnel du CCFN fournit un soutien technique et professionnel, supervise les travaux expérimentaux, oriente les analyses et l'interprétation des données, et donne des conseils de suivi au moment de la présentation des résultats scientifiques finaux. La fourniture d'une ressource destinée à l'éducation et la permanence d'une ressource pour une carrière en recherche sont reconnues comme des éléments essentiels de la mission du CCFN consistant à générer de la valeur pour le Canada.

## Excellence de classe mondiale

Le CCFN est une installation concurrentielle sur le plan mondial, ce qu'illustre le nombre et la qualité des scientifiques internationaux attirés au Canada pour effectuer des expériences au Centre. Pendant l'année 2007, des scientifiques provenant d'Arménie, de Belgique, d'Allemagne, d'Italie, du Japon, des Pays-Bas, de Russie, de Suède, de Suisse, du Royaume-Unis et des États-Unis ont été impliqués dans des expériences effectuées au CCFN. Voici quelques exemples de chercheurs et institutions d'importance provenant de l'étranger qui ont récemment collaboré avec le personnel du CCFN ou utilisé du temps de faisceau du CCFN : Robert J. Birgeneau, chancelier de l'université de Californie à Berkely et Collin Broholm de l'université John Hopkins, pour l'étude de la dynamique du spin et des transitions de phases dans les matériaux supraconducteurs; Roger A.Cowley, professeur émérite, université d'Oxford, pour l'étude des fluctuations quantiques, comme la décroissance des ondes de spin dans les matériaux supraconducteurs; et le Oak Ridge National Laboratory (ORNL) pour le développement d'instruments neutroniques. Chris Tulk est venu au CCFN pour tester des composants et la conception d'instruments destinés au développement d'un diffractomètre à pression et neutrons à spallation, instrument permettant l'étude de matériaux sous très hautes pressions. Gene Ice est venu au CCFN pour montrer que des supermiroirs à neutrons de Kirkpatrick–Baez peuvent être utilisés efficacement dans des expériences de diffusion des neutrons, étape cruciale dans le développement d'un diffractomètre à microfaisceau Laue polychromatique. La compétitivité du CCFN sur la

for publications of research conducted at the CNBC (the impact factor was 4.5 for its 2001-2005 publications, substantially higher than most physical science journals); these papers are frequently published in high-quality journals (for example, 8% of all its 2003-2005 publications were published in *Physical Review Letters* alone). The CNBC's excellence has been confirmed by international experts who recently rated the CNBC the highest of eleven different elements of the federal S&T infrastructure and regulatory system in conferring advantage to Canada.[2]

## Advancing Canada's Priorities

Canada's federal S&T Strategy identifies four priority areas for research and innovation: health and related life sciences, information and communication technologies, environmental science and technologies, and energy and natural resources. Neutrons can be used for important research in all of these areas. Some examples of recent and current research conducted at the CNBC include the following collaborations:

(1) Dr. Helmut Fritzsche of CNBC with Dr. David Mitlin from the University of Alberta and NRC-National Institute for Nanotechnology, to study hydrogen storage capacities of new materials with an impact on the development hydrogen powered vehicles (see research highlight on page 16); (2) Dr. Ron Rogge of CNBC with Dr. Kelly Conlon from AECL (Atomic Energy of Canada Ltd.), to study nuclear irradiated fuels to improve nuclear energy technologies; (3) Dr. John Katsaras of CNBC with Stephen Wassall from Indiana University-Purdue University Indianapolis, to study biomimetic membranes to understand living-cell membranes, knowledge that is important for drug delivery (see research highlight on page 17); and (4) Dr. Zahra Yamani of CNBC with multiple academic research groups, to perform fundamental studies of quantum materials, including the characterization of superconductors, which is expected to lead to the development of high-temperature superconductors and enormous impacts on lossless power transmission, quantum computing and medical diagnostics.

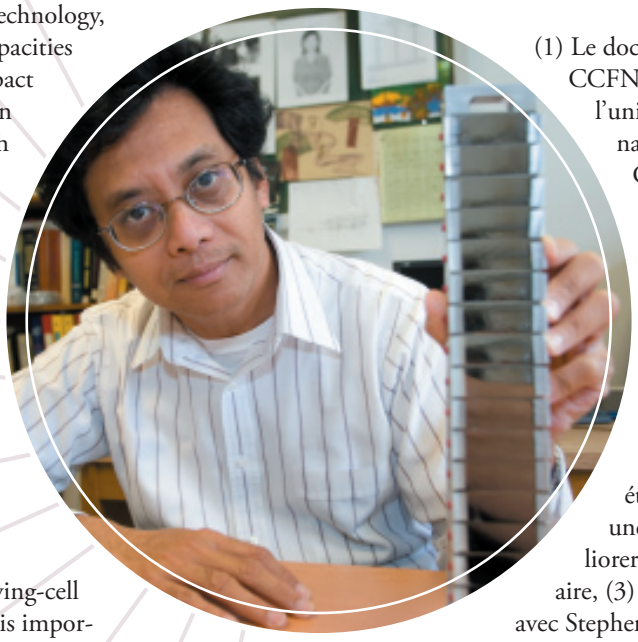

[2] "The State of Science and Technology in Canada," *Report of the Canadian Council of Academies*, ISBN 0-9781778-0-0, **p.108** (2006).

scène mondiale est aussi illustrée par ses taux élevés de citation de publications de recherches effectuées dans ses laboratoires (le facteur d'impact a été de 4,5 pour ses publications 2001-2005, ce qui est substantiellement plus élevé que la plupart des revues scientifiques en physique) et ces articles ont souvent été publiés dans des revues de haute qualité (à titre d'exemple, 8 % de toutes les publications 2003-2005 ont été publiées dans *Physical Review Letters* seulement). Par ailleurs, l'excellence du CCFN' a été confirmée dans des études récentes. À titre d'exemple, des experts internationaux ont récemment classé le CCFN comme le plus important des onze éléments différents de l'infrastructure fédérale en matière de S et T et système de réglementation conférant un avantage au Canada.[2]

## Développement des priorités du Canada

La stratégie gouvernementale en matière de science et de technologie du Canda identifie quatre priorités pour la recherche et l'innovation : sciences et technologies de la santé et sciences de la vie connexes, technologies de l'information et des communications, sciences et technologies environnementales, et énergie et ressources naturelles. Les neutrons peuvent être utilisés pour d'importantes recherches dans ces domaines. Exemples de récentes recherches et de recherches en cours effectuées au CCFN avec les collaborations suivantes :

(1) Le docteur Helmut Fritzsche du CCFN avec le docteur David Mitlin de l'université de l'Alberta et l'Institut national de la nanotechnologie CNRC pour étudier les capacités de stockage de l'hydrogène de nouveaux matériaux et l'impact sur le développement de véhicules propulsés à l'hydrogène (voir les points saillants de la recherche page 16), (2) le docteur Ron Rogge du CCFN avec le docteur Kelly Conlon d'EACL (Énergie atomique du Canada limitée) pour étudier des combustibles ayant subit une irradiation nucléaire pour améliorer les technologies de l'énergie nucléaire, (3) le docteur John Katsaras du CCFN avec Stephen Wassall de la Indiana University-Purdue University Indianapolis pour étudier les membranes biomimétiques afin de comprendre les membranes à cellules vivantes, connaissance importante pour le relargage de médicaments (voir les points saillants de la recherche page 17), et (4) le docteur Zahra Yamani du CCFN avec plusieurs groupes de recherche universitaires pour effectuer des études fondamentales sur les matériaux quantiques, dont la caractérisation de supraconducteurs qui pourrait mener au développement de supraconducteurs à haute température, ce qui aurait un impact considérable sur le transport d'énergie sans perte, l'informatique quantique et les diagnostics médicaux.

[2] « L'état de la science et de la technologie au Canada », *rapport du Conseil des académies canadiennes*, ISBN 0-9781778-0-0, p.**108** (2006).

## Partnerships

The vast majority of research conducted at the CNBC involves collaborators from academia, industries and government laboratories from across Canada and abroad. Since the majority of CNBC users come from Canadian universities, NSERC funds help to support their access to the CNBC through a Major Resource Support (MRS) Grant. The MRS Grant was awarded to applicants from the Canadian neutron scattering community and is administered by McGill University. The CNBC is accessible to external researchers, whether or not they are experts in neutron techniques. CNBC staff scientists typically use about 15% of the facility time pursuing their own research projects. Researchers from industry recognize the value of understanding materials in systems that have significant economic or safety consequences of failure. Industrial clients pay full cost recovery fees for access to CNBC facilities that support their proprietary research. A recent example of a major partnership was the commissioning of the new D3 neutron reflectometer in June 2007. The proposal was led by the University of Western Ontario and supported by 12 other Canadian universities and was funded in a federal-provincial partnership between the Canada Foundation for Innovation (CFI), the province of Ontario (through the Ontario Innovation Trust and the Ministry of Research and Innovation) and NRC.

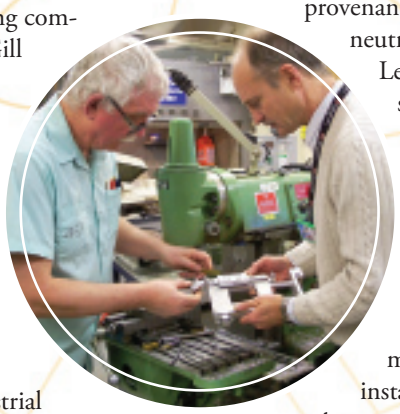

## Accountability

The Canadian Institute for Neutron Scattering (CINS), which represents the Canadian neutron user community, provides a committee to oversee the management of NSERC MRS funds by the CNBC. The CINS Oversight Committee makes site visits to the CNBC and produces an annual report to NSERC, which is a requirement for the release of funds each fiscal year. The CNBC is accountable to the University of Western Ontario, and ultimately to the CFI, for expenditures of CFI Infrastructure Operating Funds associated with operation of the D3 neutron reflectometer. The CNBC is also accountable to the NRC, and ultimately to the government of Canada, through an annual performance report and queries from the office of the Auditor General of Canada. The CNBC is required to demonstrate alignment with NRC's goals, as expressed in its 2006–2011 strategy, *Science at Work for Canada*. Finally, because the CNBC is located on the site of Canada's main nuclear establishment, the facility is accountable for compliance with policies and practices of AECL, overseen by the Canadian Nuclear Safety Commission.

## Les partenariats

La vaste majorité des recherches effectuées au CCFN implique des collaborateurs canadiens et étrangers provenant de laboratoires universitaires, industriels et gouvernementaux. Comme la majorité des utilisateurs du CCFN proviennent d'universités canadiennes, le financement du CRSNG leur permet d'accéder au CCFN grâce à la bourse d'accès aux installations majeures(MRS). La bourse MRS a été accordée à des postulants provenant de la communauté canadienne de diffusion des neutrons; elle est administrée par l'université McGill. Le CCFN est ouvert aux chercheurs externes, qu'ils soient ou non experts en techniques neutroniques. Les scientifiques du CCFN utilisent généralement 15 % du temps des installations pour la réalisation de leurs projets de recherche. Les chercheurs provenant du secteur industriel reconnaissent qu'il est nécessaire de comprendre les matériaux se trouvant dans des systèmes, dont la défaillance peut avoir d'importantes conséquences en matière d'économie et de sécurité. Pour accéder aux installations du CCFN qui leur permettent d'effectuer leurs recherches exclusives, les clients industriels paient les frais de recouvrement complet des coûts. Un exemple récent de partenariat majeur a été la mise en service en juin 2007 du nouveau réflectomètre neutronique D3. Le projet a été conduit par l'université de Western Ontario et a été soutenu par 12 autres universités canadiennes; il a été financé grâce à un partenariat fédéral-provincial avec la Fondation canadienne pour l'innovation (FCI), la province de l'Ontario (par l'intermédiaire de l'Ontario Innovation Trust et du ministère ontarien de la Recherche et de l'Innovation) et le Conseil national de recherches Canada (CNRC).

## Responsabilisation

L'Institut canadien de la diffusion des neutrons (ICDN), qui représente la communauté canadienne des utilisateurs de neutrons, fournit un comité de supervision de la gestion des fonds MRS du CRSNG par le CCFN. Le comité de supervision de l'ICDN effectue des visites au CCFN et produit un rapport annuel destiné au CRSNG, une exigence pour la libération des fonds de chaque exercice financier. Le CCFN est responsable devant l'université de Western Ontario et, ultimement devant la Fondation canadienne pour l'innovation (FCI), des dépenses du budget d'exploitation de la FCI associées au fonctionnement du réflectomètre neutronique D3. Le CCFN est aussi responsable devant le CNRC et, ultimement, devant le gouvernement du Canada, par l'intermédiaire d'un rapport annuel de rendement et des questions provenant du bureau du Vérificateur général du Canada. Le CCFN doit faire la preuve qu'il vise les mêmes objectifs que le CNRC, tel qu'elles sont définies dans sa stratégie 2006-2011, *La science à l'œuvre pour le Canada*. Finalement, le CCFN étant situé sur le site du principal établissement nucléaire du Canada, les installations sont responsables de leur conformité avec les politiques et pratiques d'EACL, supervisées par la Commission canadienne de sûreté nucléaire.

# CNBC News
# Nouvelles du CCFN

## CNBC Scientist Receives Honorary Degree

Dr. Bill Buyers has been awarded the honorary degree of Doctor of Science by his alma mater, the University of Aberdeen. This award recognizes Bill's distinguished career in condensed matter physics, in particular his scientific contributions to the field of magnetism.

Since his arrival to Canada in 1965 as an NRC post-doctoral fellow, Bill has remained at the forefront of research on highly-correlated electron systems. Bill's early work was pivotal in establishing the nature of spin waves and crystal field excitations in magnetic materials, and the nature of impurities in magnetic insulators. He then turned his attention to quantum magnetism. He achieved the first observation of the "Haldane Gap" in the spin spectrum of a spin-1 antiferromagnetic chain compound, confirming a highly controversial speculation by theorist D.M. Haldane. Bill's *tour de force* neutron experiments have spawned a host of experimental and theoretical studies worldwide.

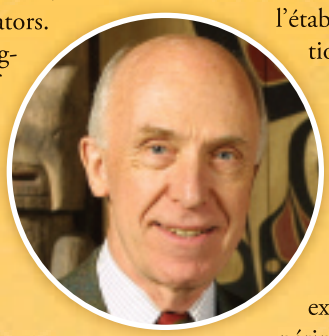

Bill Buyers

Today, as a retired NRC Principal Research Officer, a Guest Researcher with the NRC-CNBC, a member of the Canadian Institute for Advanced Research and a collaborator in many international projects, Bill continues an active research program that focuses on quantum magnetism and high-temperature superconductors.

Over the years, Bill's accomplishments have been celebrated on a number of occasions, the most notable being the Royal Society of Canada's Rutherford Medal (1985), the Gold Medal of the Canadian Association of Physicists (2001) and the Queen's Jubilee Gold Medal (2002). The award ceremonies conferring on Bill the degree of Doctor of Science will take place in November 2008.

## Un scientifique du CCFN reçoit une distinction honorifique

Le docteur Bill Buyers s'est vu décerner le titre honorifique de docteur en science par son alma mater, l'université d'Aberdeen. Cette nomination reconnaît la carrière exceptionnelle de Bill en physique de la matière condensée, et particulièrement ses contributions scientifiques dans le domaine du magnétisme.

Arrivé au Canada en 1965 en tant que détenteur d'une bourse de perfectionnement postdoctoral du CNRC, Bill est resté à l'avant-scène de la recherche sur les systèmes d'électrons fortement corrélés. Les premiers travaux de Bill étaient essentiels à l'établissement de la nature des ondes de spin et des excitations des champs cristallins dans des matériaux magnétiques, ainsi que de la nature des impuretés dans des isolants magnétiques. Il s'est ensuite intéressé au magnétisme quantique. Il a été le premier à observer de l'intervalle de Haldane dans le spectre de spins d'un composé à chaîne antiferromagnétique de spin 1, ce qui a confirmé une spéculation très controversée émise par le théoricien D. M. Haldane. Le tour de force des expériences de Bill a engendré un ensemble d'études expérimentales et théoriques dans le monde entier.

Aujourd'hui, agent principal de recherche du CNRC à la retraite, chercheur invité au CCFN-CNRC, membre de l'Institut canadien de recherches avancées et collaborateur à de nombreux projets internationaux, Bill poursuit un programme de recherche portant principalement sur le magnétisme quantique et les supraconducteurs à haute température.

Au cours des années, les réalisations de Bill ont été célébrées à de nombreuses occasions, les plus notables étant la médaille Rutherford de la Société royale du Canada (1985), la médaille d'or de l'Association canadienne des physiciens (2001) et la Queen's Jubilee Gold Medal (2002). La cérémonie de reconnaissance conférant à Bill le titre de Docteur en science se déroulera en novembre 2008.

Representing the Minister of Industry, Cheryl Gallant MP spoke of the importance of research into advanced materials and the impact of this research on Canada's society and economy.

La députée Cheryl Gallant, représentant le ministre de l'Industrie, a souligné l'importance de la recherche en matière de matériaux avancés et l'impact de cette recherche sur la société et l'économie du Canada.

## THE LATEST ADDITION TO THE CNBC IS CANADA'S FIRST NEUTRON REFLECTOMETER

On June 15th, 2007, the CNBC welcomed of a group of distinguished guests for a ribbon cutting ceremony that marked the official opening of the new neutron reflectometer. The guests included representatives from federal and provincial science and funding agencies and elected officials from federal, provincial and municipal government, as well as university vice presidents and scientists. They represented the broad scientific community that will benefit from this unique research tool, and the partnership led by The University of Western Ontario that enabled it to be built. Unique in Canada, this world-class instrument opens up new research possibilities, using neutrons to study nanometre-scale thin films and interfaces.

The D3 neutron reflectometer has already been used to produce insights into hydrogen storage materials, which have been published in Applied Physics Letters (See research highlight on page 17). The CNBC now has six spectrometers, all of which are operated as user instruments and are accessible to Canadian and international researchers under a peer-review proposal system:

- D3, Reflectometer
- C2, Powder Diffractometer
- C5, Polarized-Beam Triple-Axis Spectrometer
- E3, Triple-Axis Spectrometer / Diffractometer
- L3, Strain-Scanning Diffractometer
- N5, Triple-Axis Spectrometer /

## LE RÉFLECTOMÈTRE NEUTRONIQUE EST LE DERNIER AJOUT AU CCFN

Le 15 juin 2007, le CCFN-CNRC recevait dans ses laboratoires un groupe d'invités distingués pour la cérémonie d'inauguration officielle du nouveau réflectomètre neutronique. Parmi les invités se trouvaient des représentants d'organismes fédéraux et provinciaux aussi bien scientifiques que de financement, des élus des gouvernements fédéral, provincial et municipaux, ainsi que des vice-présidents d'universités et des scientifiques. Ils représentaient la communauté scientifique élargie, qui profitera de cet outil de recherche unique, ainsi que le partenariat à la tête duquel se trouvait l'université de Western Ontario qui a permis sa construction. Unique au Canada, cet instrument de classe internationale offre de nouvelles possibilités en recherche, en utilisation des neutrons pour étudier les films minces et les interfaces à l'échelle nanométrique.

Le réflectomètre neutronique D3 a déjà été utilisé pour produire des données sur des matériaux de stockage de l'hydrogène, qui ont été publiées dans Applied Physics Letters (voir les points saillants de la recherche page17). Le CCFN dispose maintenant de six réflectomètres qui sont tous sont exploités comme instruments pour les utilisateurs et sont accessibles aussi bien aux chercheurs canadiens qu'étrangers dans le cadre d'un programme d'examen des propositions par des pairs.

- Réflectomètre, D3
- Diffractomètre sur poudre, C2
- Spectromètre à trois axes à faisceau polarisé, C5
- Diffractomètre/spectromètre à trois axes, E3
- Diffractomètre à balayage des contraintes, L3
- Prototype de spectromètre à trois axes / petit angle de diffusion, N5

Dr. Helmut Fritzsche using the new D3 Reflectometer owned by The University of Western Ontario.

Docteur Helmut Fritzsche utilisant le nouveau réflectomètre D3, propriété de l'université de Western Ontario.

### First Results from the D3 Reflectometer

The first publication[3] of results from the new D3 neutron reflectometer (opened June, 2007), arose from a collaboration between CNBC and researchers from the University of Alberta / NRC National Institute for Nanotechnology. The goal of the research was to understand the absorption and distribution of hydrogen in a new hydrogen storage material, which is based on nanostructured thin films of magnesium alloys with a palladium surface layer. This research centres on materials for practical application in future hydrogen-powered vehicles (See research highlight on page 16).

### Premiers résultats du réflectomètre D3

La première publication[3] de résultats obtenus grâce au nouveau réflectomètre neutronique D3 (mis en service en juin 2007) est issue d'une collaboration entre le CCFN et des chercheurs de l'université de l'Alberta / Institut national de la nanotechnologie CNRC. Cette recherche avait pour objectif de comprendre l'absorption et la répartition de l'hydrogène dans un nouveau matériau de stockage, basé sur des films minces de nanostructure d'alliage de magnésium avec une couche superficielle en palladium. Cette recherche se concentre sur des matériaux pouvant être utilisés dans de futurs véhicules propulsés par hydrogène (voir les points saillants de la recherche page 16).

[3] H. Fritzsche, M. Saoudi, J. Haagsma, C. Ophus, E. Luber, C. T. Harrower, and D. Mitlin. 2008. Neutron reflectometry study of hydrogen desorption in destabilized MgAl alloy thin films. *Appl. Phys. Lett.* **92**, 121917.

[3] H. Fritzsche, M. Saoudi, J. Haagsma, C. Ophus, E. Luber, C. T. Harrower et D. Mitlin. 2008. Étude de réflectométrie neutronique de la désorption de l'hydrogène dans des couches minces en alliage MgAl déstabilisées. *Applied Physics Letters* **92**, 121917.


The CINS Long Range Plan may be viewed at www.cins.ca.

*Le plan à long terme de l'ICDN peut être obtenu à l'adresse www.cins.ca.*

## CINS Long-Range Plan Produced

The Canadian Institute for Neutron Scattering (CINS) has produced a plan for the next 40 years that envisions a new Canadian Neutron Centre (CNC) as a key resource for the future of materials research in Canada. CINS has represented the Canadian neutron user community since 1987 and currently has over 400 members. "In carrying out this plan for neutron scattering to 2050," states the plan, "we believe Canada will reinforce its world-class capacity for excellence in materials research, and deliver impacts across the scientific spectrum from discovery to innovation." The new CNC is conceived to supersede and expand on the capabilities of today's NRU reactor, by including a cold neutron source and capacity for more than 20 beam lines to be installed over its lifetime.

## The CNBC Participates in a Non-Proliferation Program

The CNBC is collaborating with the Institute of Chemical Physics of the Armenian National Academy of Sciences in Yerevan as part of an International Science and Technology Center (ISTC) project dedicated to making metal alloys and their hydrides for the purposes of neutron shielding. Established by international agreement in 1992 as a non-proliferation program, ISTC is an organization dedicated to applying the talents of former weapon scientists of the ex-Soviet Union to the industrial demands of international markets. Participants in this collaboration use neutron diffraction to analyse the phases of alloys and hydrides produced from self-propagating, high-temperature synthesis, also known as solid flame synthesis. In solid flame synthesis, igniting an intimate mixture of metals or hydrides starts exothermic reactions that self-propel the reaction front through the sample, to produce novel alloys or hydrides of alloys. In addition to the standard $\alpha$-phase of Ti, Zr and Hf, the binary and ternary alloys produce copious amounts of the thermodynamically unstable $\omega$-phase. The CNBC staff is studying deuterides of these alloys and has observed that the $\omega$-phase returns upon dedeuteriding these alloys, a phenomenon requiring structural analysis using neutrons in order to explain. CNBC staff is also examining the attenuation efficiency of these alloys and hydrides.

## Production d'un plan à long terme de l'ICDN

L'Institut canadien de la diffusion des neutrons (ICDN) a produit un plan couvrant les 40 prochaines années qui envisage un nouveau Centre canadien de neutrons (CCN) comme ressource clé destinée à la recherche canadienne sur les matériaux de l'avenir. L'ICDN représente la communauté des utilisateurs canadiens de neutrons depuis 1987 et le nombre de ses membres s'élève actuellement à plus de 400. « Lors de la réalisation de ce plan pour la diffusion des neutrons jusqu'en 2050, » indique le plan, « nous croyons que le Canada renforcera sa capacité mondiale d'excellence en recherche sur les matériaux et aura des impacts dans le spectre scientifique allant des découvertes aux innovations. » Le nouveau CCN est conçu pour remplacer et étendre les capacités du réacteur NRU actuel en incluant une source de neutrons froids et une capacité pour plus de 20 lignes de faisceau qui seront installées pendant sa vie utile.

## Le CCFN participe à un programme de non-prolifération

Le CCFN collabore avec l'Institute de chimie physique de l'Académie nationale des sciences arménienne à Yerevan dans le cadre d'un projet du Centre international des sciences et de la technologie (CIST) voué à la fabrication d'alliages métalliques et de leurs hybrides destinés au blindage contre les neutrons. Constitué en 1992 grâce à un accord international dans le cadre d'un programme de non-prolifération, le CIST est une organisation vouée à la mise des anciens scientifiques en matière d'armement de l'ex-Union soviétique au service de demandes industrielles des marchés internationaux. Les participants à cette collaboration mettent à profit la diffraction des neutrons pour analyser les phases des alliages et des hybrides produits dans le cadre de la synthèse par réaction auto-entretenue à haute température. Dans la synthèse par réaction auto-entretenue à haute température, l'inflammation d'un mélange intime de métaux ou d'hydrures déclenche des réactions exothermiques qui auto-entretiennent le front de réaction dans tout l'échantillon, ce qui produit des alliages nouveaux ou des hydrures d'alliages. En plus de la phase $\alpha$ standard du Ti, Zr et Hf, les alliages binaires et tertiaires produisent de grandes quantités de phase $\omega$ thermodynamiquement instable. Le personnel du CCFN étudie des detériures de ces alliages et a observé que la phase $\omega$ revenait lors de la detérisation de ces derniers, phénomène nécessitant une analyse structurelle au moyen de neutrons pour pouvoir être expliqué. Le personnel du CCFN a aussi examiné l'efficacité de l'affaiblissement de ces alliages et hydrures.

### *Unusual Orientation and Location for Cholesterol*

Over the past two years, the CNBC collaborated with Brock University (St. Catharines, ON) and Indiana University-Purdue University Indianapolis (IN, USA) to study the location of cholesterol in a number of model membrane systems, through neutron diffraction. In 2006, the participating researchers were surprised to discover that cholesterol is located between the layers of a poly-unsaturated fatty acid (PUFA)-containing phospholipid bilayer. The collaborators have now determined conclusively that the cholesterol between the layers lies flat on its side, an unusual orientation, as cholesterol is known to stand upright in other lipid bilayers (see research highlight on page 17). The findings suggest that the poor affinity for PUFA may affect the distribution of cholesterol in the membrane, and a tendency to sit at the centre of the PUFA-containing membranes would facilitate the sterol's flip-flop from one side of a membrane to the other. Thus, in living cells, the presence of PUFAs in the inner leaflet of plasma membranes may enhance the transfer of cholesterol to the outer leaflet, modifying the membrane's structure and thereby its function.

### *Orientation et emplacement inhabituels du cholestérol*

Lors des deux dernières années, le CCFN a collaboré avec la Brock University (St. Catharines, ON) et la Indiana University-Purdue University Indianapolis (IN, É.-U.) pour étudier avec la diffraction des neutrons l'emplacement du cholestérol dans un certain nombre de systèmes de membranes modèles. En 2006, les chercheurs participants ont eu la surprise de découvrir que le cholestérol est localisé entre les couches d'acides gras polyinsaturés (AGPI), contenant des bicouches phospholipidiques. Cette collaboration a mené à la conclusion que le cholestérol entre les couches repose à plat sur le côté, orientation inhabituelle, car le cholestérol est reconnu pour se tenir droit dans d'autres bicouches lipidiques (voir les points saillants de la recherche page 17). Les constatations suggèrent que la faible affinité pour les AGPI pouvait affecter la répartition du cholestérol dans la membrane et la tendance à se déposer au centre de l'AGPI; contenir les membranes faciliterait le basculement des stérols d'un côté à l'autre d'une membrane. De la sorte, dans des cellules vivantes, la présence d'AGPI dans le feuillet interne de membranes plasmiques peut améliorer le transfert du cholestérol vers le feuillet externe, ce qui modifie la structure de la membrane et donc sa fonction.

### *Additional Capacity for Studying Highly Radioactive Samples*

Because of CNBC's location at a nuclear research facility, CNBC staff frequently handle radioactive samples. With samples of limited radiological hazard, personnel are protected by safety procedures that are designed to keep people away from the sample and to minimize exposure time. These procedures include the use of remote tooling to handle the sample and remote control of the beam line. When the samples are highly radioactive, special shielded cells are also required. Recently, a shielded cell for powder diffraction was designed at the CNBC so that phase analysis of irradiated nuclear fuel could be carried out. The first measurements using this cell were performed at the CNBC in collaboration with AECL and have now attracted international collaboration. This new cell adds to the already existing capacity for the study of radioactive samples; in 2001, the CNBC developed a heavily shielded cell for carrying out stress-mapping experiments. This cell allows the sample to be repositioned internally, with the scattering angle remaining fixed at 90 degrees. The new powder diffraction cell for the analysis of fuels allows for an 80-degree range in the scattering angle. Both shielded cells are designed for easy sample loading by operators at hot cells, which are facilities designed for the handling of highly radioactive materials.

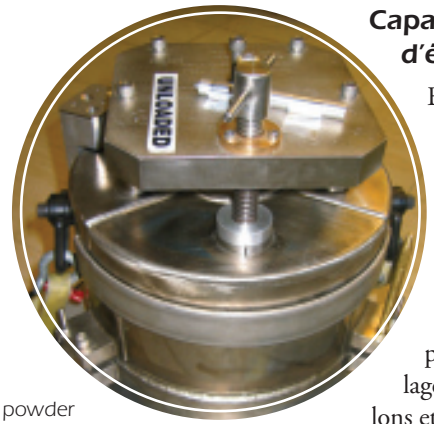


The new powder diffraction cell.

La nouvelle cellule blindée de diffraction sur poudres.

### *Capacité supplémentaire pour l'étude d'échantillons fortement radioactifs*

En raison de l'emplacement du CCFN au sein d'une installation de recherche nucléaire, le personnel de ce centre manipule souvent des échantillons radioactifs. Avec des échantillons représentant un risque radiologique limité, le personnel est protégé par des procédures de sécurité conçues pour l'éloigner des échantillons et minimiser le temps d'exposition. Ces procédures impliquent l'utilisation d'un outillage télécommandé pour manipuler les échantillons et d'une télécommande de la ligne de faisceau. Lorsque les échantillons sont fortement radioactifs, des cellules blindées spéciales sont aussi requises. Récemment, une cellule blindée pour la diffraction sur poudres a été conçue au CCFN, de sorte qu'il est maintenant possible d'effectuer l'analyse des phases de combustibles nucléaires irradiés. Les premières mesures utilisant cette cellule ont été effectuées au CCFN en collaboration avec EACL; elle a aujourd'hui attiré des collaborations internationales. Cette nouvelle cellule s'ajoute à la capacité existante d'étude d'échantillons radioactifs; en 2001, le CCFN a mis au point une cellule fortement blindée destinée à la réalisation d'expériences de cartographie des contraintes. Cette cellule permet de réorienter intérieurement l'échantillon, tout en maintenant l'angle de diffusion fixé à 90 degrés. La nouvelle cellule de diffraction sur poudres destinée à l'analyse de combustibles permet d'obtenir un angle de diffusion sur une plage de 80 degrés. Les deux cellules blindées sont conçues pour simplifier le chargement des échantillons par des opérateurs à des installations prévues pour manipuler des matériaux fortement radioactifs appelés cellules chaudes.

# Scientific Reports

# 2007

The scientific reports from our community of international users are presented in the language in which they were written.

Disclaimer: The experimental reports contained in this document were not subjected to a formal peer review.

# Rapports scientifiques

Les rapports scientifiques de notre communauté d'utilisateurs internationaux sont présentés dans la langue dans laquelle ils ont été écrits.

Avertissement : Les rapports d'expériences contenus dans ce document n'ont pas été soumis à un examen formel par des pairs.

# Research Highlights

## Quest for Holy Grail in Hydrogen Storage

Researchers at the NRC Canadian Neutron Beam Centre (CNBC), led by Dr. Helmut Fritzsche, and the University of Alberta / National Institute for Nanotechnology (NRC-NINT), led by Professor David Mitlin, made an important discovery in the 'quest for the Holy Grail' in hydrogen storage materials. The collaborative team studied an aluminum-magnesium hydride alloy that is a candidate for applications in the automotive industry. The "Holy Grail" material, as defined by the US Department of Energy, would need to hold 4 kg of stored hydrogen at 6% hydrogen weight storage at no more than 85°C and be able to power a vehicle for 500 km. Unlike X-rays, neutrons are very sensitive to hydrogen and its isotopes, and with the recent development of the new D3 Reflectometer at the lab, this collaboration is making a significant contribution to the Canadian research community working in the field of hydrogen storage materials.

Professor Mitlin produced thin film alloy specimens of magnesium and aluminium at the nanometre scale and capped them with a palladium layer. "Thin films are a testing ground… not the end product," explains Dr. Helmut Fritzsche, "We use thin films as a model system so we can understand what's going on at the molecular level." Palladium acts as a catalyst that enables hydrogen to quickly enter the alloy. With the new reflectometer technique, the team was able to distinguish problems at the interface and determine the amount and location of hydrogen in the film. From this point, the team varied the aluminum/ magnesium content to find the best composition.

The D3 Reflectometer revealed the profile of the hydrogen; for example, how much hydrogen there is in the centre of the film versus how much hydrogen there is at the surface. The D3 Reflectometer results showed that hydrogen was evenly dispersed in the alloy and by adjusting the magnesium-aluminum mix, the researchers discovered that 30% more hydrogen can be stored if the alloy composition is changed from a ratio of 60:40 to a ratio of 70:30. This latter composition also releases its hydrogen at a temperature 25°C lower than the former. Ultimately, the team brought down the temperature to 170°C, a very promising start that clearly shows the direction to follow to improve the material for practical applications. These results were published in the March 2008 issue of *Applied Physics Letters*.

Finding the right material will be a step in the right direction for hydrogen storage research across the country. Having the right tool, like the new D3 Reflectometer and the internal expertise to run it, is only half of the story. The other half will involve researchers visiting CNBC from other R&D organizations, academia or industry from across Canada, as CNBC is a steward for this kind of infrastructure.

The newly commissioned $2.5 M D3 neutron reflectometer was completed in 2007 as a result of the partnership of 13 universities, industry and NRC, and with funding from the Canada Foundation for Innovation, the Ontario Innovation Trust and the Ontario Ministry of Research and Innovation. The new reflectometer joins a suite of five other neutron instruments at the CNBC, essential parts of Canada's national toolkit.

## *The Unusual Location of Cholesterol in a Polyunsaturated Lipid Membrane*

T. A. Harroun, J. Katsaras and S. R. Wassall

Cholesterol is an essential component of mammalian cells and is either obtained from foods of animal origin (e.g., milk, cheese, meat, eggs) or synthesized in the endoplasmic reticulum, a subcellular organelle. Cholesterol is required for building and maintaining cell membranes, regulates their fluidity, and may act as an antioxidant to prevent or slow the oxidative damage to cells.

Polyunsaturated fatty acids (PUFA) constitute a biologically influential group of molecules whose physiological importance is now becoming well established. A multitude of disease states and chronic conditions are alleviated by dietary consumption of PUFA. While interest in the topic has centred on the omega-3 class of PUFA lipids, it has also spanned a variety of human health issues, including PUFA-associated effects on protein signalling in inflammation and cancer, arteriosclerosis, and suppressive effects on the immune system. The efficacy of PUFAs has been attributed to the formation of membrane domains enriched in PUFA-containing phospholipids. According to this model, the highly disordered PUFAs provide a local environment necessary for protein function.

Over the past two years, researchers from Brock University (St. Catharines, ON), Indiana University-Purdue University Indianapolis (IN, USA) and the NRC (Chalk River, ON) have studied the location of cholesterol in a number of model membrane systems. Using neutron diffraction,[1,2] they found cholesterol aligning in the generally accepted "upright" orientation (See Figure 1A) in most membranes. The exception was found to be 20:4-20:4 (PUFA) phosphatidylcholine membranes, whereby cholesterol was unequivocally found to lie flat in the middle of the bilayer (See Figure 1B).

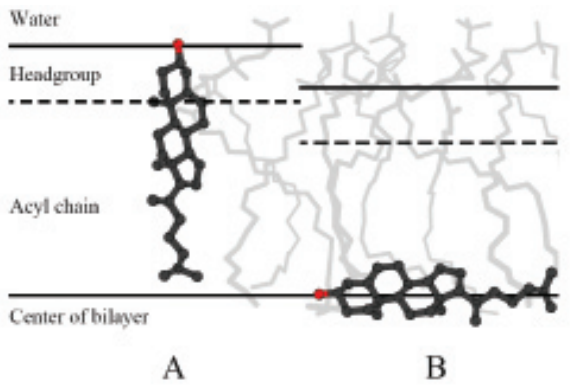


***Fig. 1*** *Schematic of the locations and orientations of cholesterol in a membrane. A gray background of model phospholipids is shown for illustration purposes. (A) Canonical location and orientation of cholesterol in a bilayer. (B) Location and orientation of cholesterol in 20:4-20:4 PC bilayers.*

The findings from the neutron diffraction work suggest that the poor affinity for PUFA may affect the transmembrane, as well as the lateral, distribution of cholesterol. A tendency to sit at the centre of the PUFA-containing membranes would facilitate the sterol's flip-flop from one side of a membrane to the other. For example, the presence of PUFAs in the inner leaflet of plasma membranes is thought to enhance the transfer of cholesterol to the outer leaflet, potentially modifying raft composition and function. Indeed, enhanced rates of flip-flop were observed for cholesterol in recently published coarse-grained simulations that identified the presence of the sterol embedded between monolayers of arachidonic acid-containing PC bilayers.[3]

#### *References*

[1] T. A. Harroun, J. Katsaras and S. R. Wassall. *Biochemistry* **45**, 1227 - 1233 (2006).
[2] T. A. Harroun, J. Katsaras and S. R. Wassall. *Biochemistry* **47**, 7090 - 7096 (2008).
[3] S. J. Marrink, A. H. de Vries, T. A. Harroun, J. Katsaras and S. R. Wassall. J. *Am. Chem. Soc.* **130**, 10 - 11 (2008).

# CNBC Publication List 2007

**The CNBC received notice of the following publications from CNBC staff and users. This list of 37 papers of research conducted at the CNBC published in 2007 may not be exhaustive.**

T. Abraham, S. R. Schooling, M.-P. Nieh, N. Kucerka, T. J. Beveridge, and J. Katsaras. **Neutron Diffraction Study of Pseudomonas Aeruginosa Lipopolysaccharide Bilayers.** *J. Phys. Chem. B* **111**: 2477-2483 (2007)

J. L. Anderson, R. C. Peterson, and I. P. Swainson. **The Atomic Structure and Hydrogen Bonding of Deuterated Melanterite, $FeSO_4 \cdot 7D_2O$.** *Can Mineral 2007* **45**: 457-469 (2007)

V. N.P. Anghel, N. Kucerka, J. Pencer and J. Katsaras. **Scattering from Laterally Heterogeneous Vesicles. II. The Form Factor.** *J. Appl. Cryst.* **40**: 513-525 (2007)

M. Blouin, M.-L. Tremblay, A. Bercier, L. Roue, D. Guay, R. Schulz, L. M.D. Cranswick, and I. P. Swainson. **Effect of Boron on the Structural and Electrochemical Properties of Nanocrystalline $Ti_2RuFeB_x$ Electrodes.** *Electrochimica Acta* **52**: 4497-4505 (2007)

A. Coucair, M. Chakrapani, B. Chakravarthy, J. Katsaras, and L.J. Johnston. **Preferential Accumulation of Aß(1–42) on Gel Phase Domains of Lipid Bilayers: An AFM and Fluorescence Study.** *Biochemica et Biophysica Acta* **1768**: 146-154 (2007)

H. L. Cuthbert, J. E. Greedan, I. Vargas-Baca, S. Derakhshan, and I. P. Swainson. **Synthesis, Structure and Unexpected Magnetic Properties of $La_3Re_2O_{10}$.** *Inorg. Chem.* **46** (21): 8739-8745 (2007)

W. Feng, M.-P. Nieh, S. Zhu, T. A. Harroun, J. Katsaras, and J. L. Brash. **Characterization of Protein Resistant, Grafted Methacrylate Polymer Layers Bearing Oligo (Ethylene Glycol) and Phosphorylcholine Side Chains by Neutron Reflectometry.** *Biointerphases* **2**(1): 34-43 (2007)

H. Fritzsche, M. Saoudi, K. Temst, and C. Van Haesendonck. **A Polarized Neutron Reflectometry Study of the Spin Glass Freezing in a 29 nm Thick AuFe Film.** *Physica B* **397**: 47-49 (2007)

M. Han, J.C. Bennett, M.A. Gharghouri, J. Chen, and C.V. Hyatt. **Understanding Modulated Twin Transition at the Atomic Level.** *Acta Materialia* **55**: 1731-1740 (2007)

S. Haravifard, K.C. Rule, H.A. Dabkowska, B.D. Gaulin, Z. Yamani, and W.J.L. Buyers. **Neutron and X-ray Scattering Studies of the Lightly Doped Spin-Peierls System $Cu_{1-x}Cd_xGeO_3$.** *Journal of Physics: Condensed Matter* **19**: 436222 (2007)

R. Hutanu, I. Swainson, M. Gharghouri, R. Rogge. **Neutron Diffraction Study of Magnetic Shape Memory Ni-Mn-Ga Alloy.** *Cansmart 2007 Proceedings of the International Workshop of Smart Materials and Structures:* 307-314 (2007)

T. Katsumata, A. Takase, M. Yoshida, Y. Inaguma, J. Greedan, J. Barbier, L.M.D. Cranswick and M. Bieringer. **Crystal and Magnetic Structures of High Pressure Perovskite-Type Oxyfluorides, $PbFeO_2F$ and $0.5PbFeO_2F$-$0.5PbTiO_3$ $[Pb(Fe_{0.5}Ti_{0.5})O_{2.5}F_{0.5}]$.** *Mater. Res. Soc. Symp. Proc.* **988**: (2007)

N. Kucerka, M.-P. Nieh, J. Pencer, T. Harroun, J. Katsaras. **The Study of Liposomes, Lamellae and Membranes Using Neutrons and X-rays.** *Current Opinion in Colloid & Interface Science* **12**: 17-22 (2007)

N. Kucerka, J. Pencer, M.-P. Nieh and J. Katsaras. **Influence of Cholesterol on the Bilayer Properties of Monosaturated Phosphatidycholine Unilamellar Vesicles.** *European Physical Journal E* **23**: 247-254 (2007)

N. Kucerka, J. Pencer, J. N. Sachs, J. F. Nagle, and J. Katsaras. **Curvature Effect on the Structure of Phospholipid Bilayers.** *Langmuir* **23**: 1292-1299 (2007)

G. Langelaan, S. Ryelandt, J.H. Root and P. Van Houtte. **Deterimination of the Morphological Texture of the Fibres in a Composite Material Made from a Textile of AISI 316L Fibres using a Mixed Deconvolution/Positivity Method.** *J. Appl. Cryst.* **40**: 96-104 (2007)

R. J. Lundgren, L. M.D. Cranswick and M. Bieringer. **Phase Stability, Structural Evolution and Magnetic Properties of $Sc_{(1-x)}Lu_xVO_3 (0.0 \leq x \leq 1.0)$.** *Chem. Mater.* **19**: 3945-3955 (2007)

L. E. Millon, Mu-Ping Nieh, J. L. Hutter, W. K. Wan. **SANS Characterization of an Anisotropic Hydrogel Poly (vinyl alcohol) with Vascular Application.** *Macromolecules* **40**: 3655-3622 (2007)

G. Pabst, S. Daner, R. Podgornik and J. Katsaras. **Entropy-Driven Softening of Fluid Bilayers by Alamethicin.** *Langmuir* **23**: 11705-11711 (2007)

J. Pencer, V. N.P. Anghel, N. Kucerka and J. Katsaras. **Scattering from Laterally Heterogeneous Vesicles. III. Reconciling Past and Present Work.** *J. Appl. Cryst.* **40**: 771-772 (2007)

M. Potter, H. Fritzsche, D.H. Ryan and L.M.D. Cranswick. **Low-Background Single-Crystal Silicon Sample Holders for Neutron Powder Diffraction.** *J. Appl. Cryst.* **40**: 489-495 (2007)

D.G. Sediako and M.A. Gharghouri. **Effect of Alloying Additions on Texture Development in Hot Processing of Creep Resistent Magnesium Alloys.** *Light Metals in Transport Application: 46th Annual Conference of Metallurgists of CIM*: 339-348 (2007)

D.G. Sediako, M.A. Gharghouri, R.B. Rogge, M.J. Watson. **Study of Texture Evolution During Channel-Die Compression of Mg-Al Alloys by In-Situ Neutron Diffraction.** *Magnesium Technology 2007*: TMS (The Minerals, Metals & Materials Society): 351-356 (2007)

D. Sediako, R. Rogge, A. McIvor, R. Donaberger, M.A. Gharghouri. **Neutron Diffraction in Applied Mechanics.** *CANCAM 2007 Proceedings*: 732-735 (2007)

N. Soheilnia, H. Xu, H. Zhang, T. M. Tritt, I. Swainson and H. Kleinke. **Thermoelectric Properties of $Re_3Ge_{0.6}As_{6.4}$ and $Re_3GeAs_6$ in Comparison to $Mo_3Sb_{5.4}Te_{1.6}$.** *Chem. Mater.* **19**: 4062-4068 (2007)

C. Stock, R.A. Cowley, W.J.L. Buyers, R. Coldea, C. Broholm, C.D. Frost, R.J. Birgeneau, R. Liang, D. Bonn and W.N. Hardy. **Evidence of Decay of Spin Waves Above the Pseudogap of Underdoped $Yba_2Cu_3O_{6.35}$.** *Physical Review B* **75**: 172510 (2007)

I. P. Swainson. **Neutron Scattering in Earth Sciences.** *Can Mineral 2007* **45**: 1060-1063 (2007)

I. P. Swainson and A. L. Yonkeu. **Tilt and Buckling Modes, and Acoustic Anistrophy in Layers with Post-Perovskite Connectivity.** *American Mineralogist* **92**: 748-752 (2007)

D.R. Taylor, J.T. Love, E.M. Sheridan, W.J.L. Buyers. **Neutron Study of Magnetic Ordering of Planar Spins in a Random Anisotropy Antiferromagnet: Evidence for Quantum Tunnelling?** *Journal of Magnetism and Magnetic Materials* **310**: 1473-1475 (2007)

P.S. Whitfield, I.J. Davidson, P.H.J. Mercier, Y. Le Page, L.D. Mitchell, P.W. Stephens, L.M.D. Cranswick, I.P. Swainson. **Simultaneous Refinements with Complex Compositional Constraints – Example of Singular Value Decomposition to Diagnose Poor Matrix Conditioning.** *Advances in X-ray Analysis* **50**: 133-138 (2007)

P.S. Whitfield, I.J. Davidson, P.W. Stephens, L.M.D. Cranswick, I.P. Swainson. **Diffraction Analysis of the Lithium Battery Cathode Material $Li_{1.2}Mn_{0.4}Ni_{0.3}Co_{0.1}O_2$.** *Z. Kristallogr. Suppl.* **26**: 483-488 (2007)

C.R. Wiebe, J.A. Janik, G.J. MacDougall, G.M. Luke, J.D. Garrett, H.D. Zhou, Y.-J. Jo, L. Balicas, Y. Qiu, J.R.D. Copley, Z. Yamani and W.J.L. Buyers. **Gapped Itinerant Spin Excitations Account for missing Entropy in the Hidden-Order State of $URu_2Si_2$.** *Nature Physics Letters* **3**: 96-100 (2007)

G. Van Boven, W. Chen, R. Rogge. **The Role of Residual Stress in Neutral pH Stress Corrosion Cracking of Pipeline Steels. Part I: Pitting and Cracking Occurrence.** *Acta Materialia* **55**: 29-42 (2007)

G. Van Boven, W. Chen, R. Rogge. **The Role of Residual Stress in Neutral pH Stress Corrosion Cracking of Pipeline Steels. Part II: Crack Dormancy** *Acta Materialia* **55**: 43-53 (2007)

C.J. Voyer, D.H. Ryan, J.M. Cadogan, L.M.D. Cranswick, N. Napoletano, P. Riani and F. Canepa. **Neutron Diffraction and $^{119}Sn$ Mossbauer Study of $Sm_3Ag_4Sn_4$.** *J. Phys. Condens. Matter* **19**: 436205 (2007)

S. Xu, M. A. Gharghouri and M. Sahoo. **Tensile-Compressive Creep Asymmetry of Recent Die Cast Magnesium Alloys.** *Advanced Engineering Materials* **9**: 807-812 (2007)

Z. Yamani, W.J.L. Buyers, F. Wang, Y.-J. Kim, R. Liang, D. Bonn, W.N. Hardy. **Antiferromagnetic Correlations Near the Lower Edge of Superconducting Dome in $YBCO_{6+x}$.** *Physica C* **460-462**: 430-431 (2007)

# Experimental Reports – Table of Contents

## Quantum Materials



## Materials Science and Engineering



## Soft Materials



## Condensed Matter Structures



## Thin Films and Surfaces

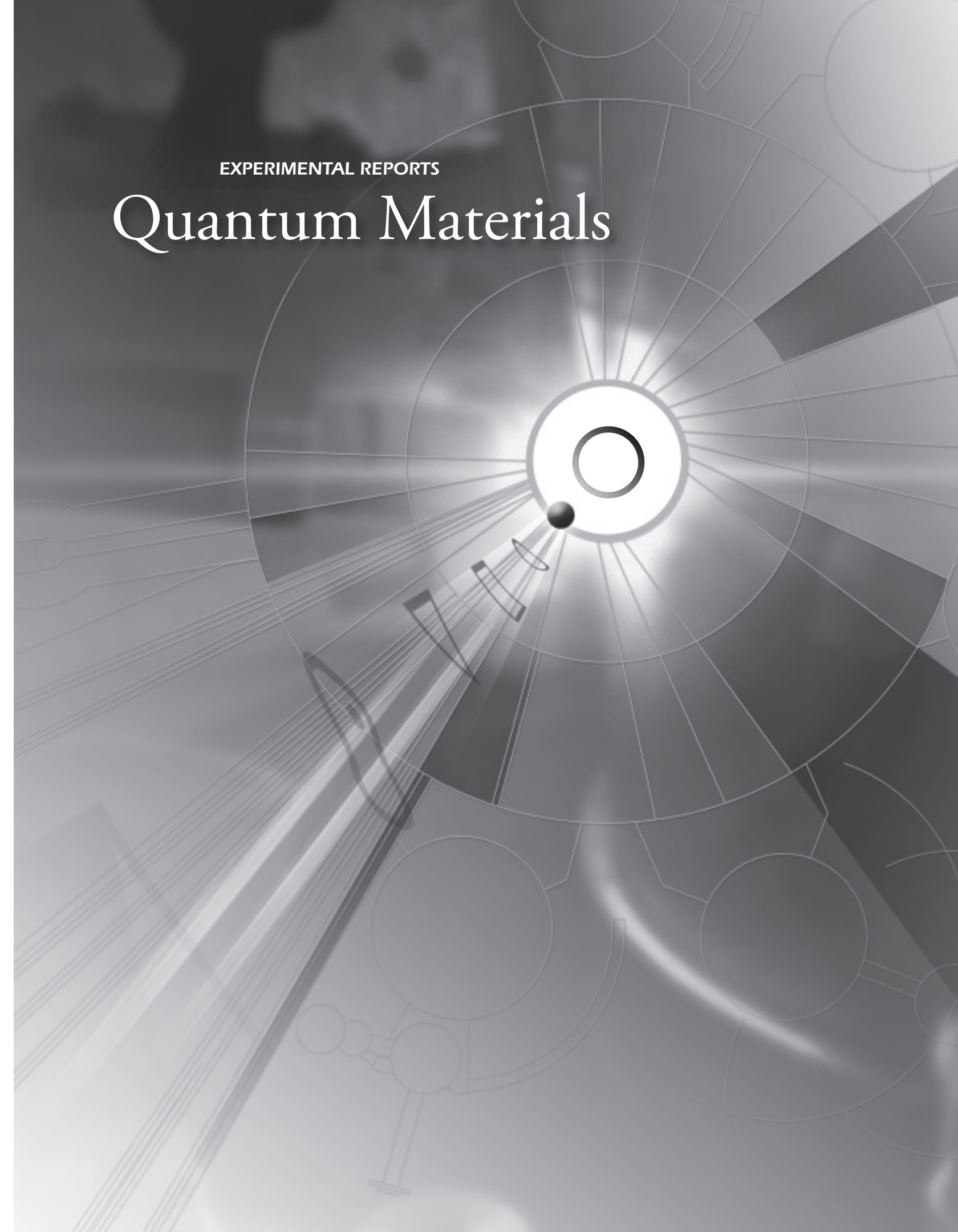

EXPERIMENTAL REPORTS

# Quantum Materials

# Spin Waves in the Ferromagnetic Ground State of the Kagome Staircase System $Co_3V_2O_8$

**M. Ramazanoglu [1], C.P. Adams [1, 2], J.P. Clancy [1], A.J. Berlinsky [1, 3], Z. Yamani [4], R. Szymczak [5], H. Szymczak [5], J. Fink-Finowicki [5], and B.D. Gaulin [1, 3]**

[1] Department of Physics and Astronomy, McMaster University, Hamilton, Ontario, Canada L8S 4M1
[2] Department of Physics, St. Francis Xavier University, Antigonish, Nova Scotia, Canada B2G 2W5
[3] Canadian Institute for Advanced Research, Toronto, Ontario, Canada M5G 1Z8
[4] Canadian Neutron Beam Centre, National Research Council, Chalk River Laboratories, Chalk River, ON, Canada K0J 1J0
[5] Institute of Physics, Polish Academy of Sciences, Warsaw, Poland 02-668

Magnetic materials in which the constituent magnetic moments reside on networks of triangles and tetrahedra have been of great interest due to their propensity for exotic ground states, a consequence of geometrical frustration [1]. While ferromagnetically-coupled moments on such lattices generally do not result in such ground states, ferromagnets, and materials that display both ferromagnetic (FM) and antiferromagnetic (AFM) interactions on such lattices remain of great interest, in part due to the relative scarcity of well-studied examples, and in part due to intriguing spin ice [2] and multiferroic phenomena [3] which characterize some of these ground states.

The kagome lattice is comprised of a two-dimensional network of corner-sharing triangles. Several realizations of magnetic moments on stacked kagome lattices with varying degrees of crystalline order have been extensively studied. The stacked kagome staircase materials $M_3V_2O_8$ ($M$ = Ni, Co) display orthorhombic crystal structures with space group *Cmce* [4]. Their kagome layers are buckled and composed of edge-sharing $M^{2+}O_6$ octahedra. These layers are separated by non-magnetic $V^{5+}O_4$ tetrahedra. The buckled kagome layers are perpendicular to the orthorhombic *b*-axis and form what is known as a stacked kagome staircase structure. Figure 1 shows the projection of the kagome staircase onto the *a-c* plane. The two inequivalent $M$ sites are known as spines ($M1$) and cross-ties ($M2$). The superexchange interaction between spine and cross-tie sites and between two adjacent spine sites are denoted by $J_{sc}$ and $J_{ss}$, respectively.

One member of this family, $Ni_3V_2O_8$ (NVO), undergoes a series of phase transitions on lowering temperature [5-9]. A very interesting characteristic of this compound is that it exhibits simultaneous ferroelectric and incommensurate AFM order, that is, multiferroic behaviour, in one of its ordered phases. In isostructural $Co_3V_2O_8$ (CVO), the $S$ = 1 magnetic moments at the $Ni^{2+}$ site are replaced with $S$ = 3/2 $Co^{2+}$ moments. CVO also displays a rich low temperature phase diagram, which has been studied using polarized and unpolarized neutron diffraction, dielectric measurements [10], magnetization [11, 12] and specific heat measurements [12]. There is a series of four AFM ordered phases below $T_N$ = 11.3 K which can be characterized by incommensurate or commensurate ordering wavevectors (0, τ, 0). In contrast to NVO, the ultimate ground state in CVO is ferromagnetic and the Curie temperature is $T_C \sim 6$ K. Earlier powder neutron diffraction measurements [10] on CVO showed ordered magnetic moments of 2.73(2) and 1.54(6) $\mu_B$ on the spine and cross-tie sites, respectively, at 3.1 K. All moments are aligned along the *a*-axis direction. In this experiment, we performed inelastic neutron scattering measurements of the spin wave excitations within the kagome staircase plane in the ferromagnetic ground state of single crystal CVO. These measurements are compared with linear spin wave theory and show a surprising sublattice dependence to the exchange interactions.

A large (5 g) and high-quality single crystal of CVO was grown using an optical floating-zone image furnace [12]. Thermal INS measurements were performed using the C5 triple-axis spectrometer. A pyrolytic graphite (PG) vertically-focusing monochromator and flat analyzer were used. Measurements were performed with a fixed final neutron energy of $E_f$ = 13.7 meV and a PG filter in the scattered beam. The collimation after the monochromator was 29'-34'-72' resulting in an energy resolution of 0.9 meV FWHM. The crystal was oriented with the (*h*0*l*) kagome staircase plane coincident with the scattering plane. Constant-$Q$ energy scans were performed along the high symmetry (*h*00) and (00*l*) directions in this plane. A follow up measurement was conducted using N5 triple-axis spectrometer with similar conditions.

A series of constant-$Q$ scans for (*h*00) and (00*l*) directions were collected at $T$ = 3 K and are presented as a color contour map in Figures 2a,c. Dispersive features corresponding to two bands of spin waves are seen in both data sets. The top of the upper spin-wave band at $\Delta E \sim 5.7$ meV corresponds to excitations reported earlier using a time-of-flight technique [7]. These constant-$Q$ scans were fit to resolution-convoluted damped harmonic oscillator (DHO) lineshapes, which gave intrinsic energy widths for the higher-energy spin-wave mode at all wavevectors ranging from $\Gamma$ = 0.6 to 1.1 meV, while the lower-energy spin waves were resolution limited at all wavevectors. This indicates a finite lifetime for the higher-energy spin waves even at temperatures $\sim T_C/2$.

We have carried out a linear spin-wave theory analysis of the magnetic excitations observed in Figures 2 (a) and (c) to understand as much of the relevant microscopic spin Hamiltonian as possible. The full Hamiltonian is potentially complicated if account is taken of the two inequivalent magnetic sites and the 3D kagome staircase structure. We employed a 2D model in which the magnetic ions in a layer are pro-

jected onto the average plane of the layer (Figure 1) and only near-neighbor exchange and single-ion anisotropy are included. Details about this theoretical calculation can be found elsewhere [13]. Best agreement between the experimental data and the spin-wave theory calculation in Figure 2 was obtained for magnetic coupling predominantly between the spine and cross-tie Co ions with $J_{sc}$ = 1.25±0.08 meV, while the spine-spine coupling $J_{ss}$ vanishes. Figure 2 shows that the spin-wave theory gives a very good description of the dispersion of the two modes (dashed lines) and accounts for the observed trend of the spin waves to trade intensity as a function of $Q$. This description is not perfect, however. The calculated dispersion of the lower spin-wave band is low compared with experiment near (200) and (002) where the intensity is very weak. The calculation is not convolved with the instrumental resolution; instead the energy width is manually set in both high and low-energy bands to correspond to the measured width. The broad (in energy) neutron groups corresponding to the upper spin-wave bands are most evident near (200) and (002). The lower energy spin-wave band becomes much more intense near the zone centers of (400) and (004). Steep excitation branches near (400) and (004) with comparatively weak intensity (Figures 2a,c) are identified as longitudinal acoustic phonons, with a speed of sound of 1050±100 m/s, in both directions. Interestingly, the upper spin wave band appears to hybridize with, or otherwise damp the longitudinal phonons near (004) (see Fig. 2c). This evidence for strong spin-lattice coupling is consistent with reports of a strong dielectric anomaly at $T_C \sim 6$ K for $\mathbf{E}||(00L)$ [10].

Our INS study of the spin-wave excitations in the ferromagnetic ground state of CVO within its kagome staircase plane reveals two separate spin-wave bands between 1.6 and 5.7 meV. The upper spin-wave band is damped with finite energy widths Γ in the range of 0.6 to 1.1 meV. These spin-wave excitations can be accurately described by a simple model Hamiltonian and linear spin-wave theory. The model gives a magnetic coupling that is predominantly between the spine and cross-tie sites of the kagome staircase.

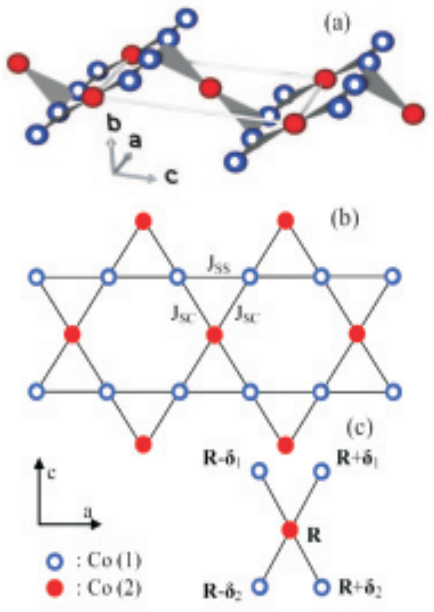


**Fig. 1** Schematic diagrams of the kagome staircase structure in 3D (a) and as reduced to 2D (b) in the *a-c* plane. The cobalt ions are represented by open and solid circles for spine (*M*1) and cross-tie sites (*M*2), respectively. Chains of spine sites running parallel to the *a*-direction are alternatively above and below the plane. (c) The basis used in the linear spin-wave theory calculation.

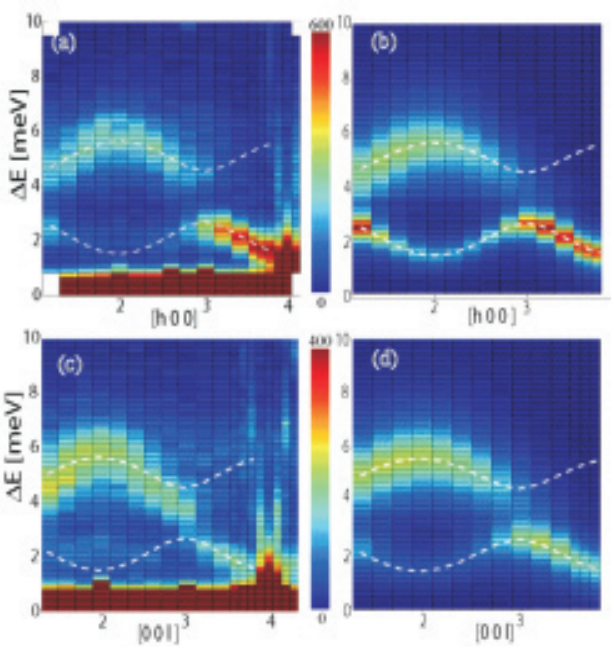


**Fig. 2** Contour maps of INS at $T$ = 3 K [(a) and (c)] and corresponding linear spin-wave theory [(b) and (d)] as described in the text. The broken lines show the dispersion relations resulting from this spin-wave theory analysis.

## References


[1] Frustrated Spin Systems, Ed. H.T. Diep. World Scientific Publishing: Singapore, 2004.

[2] S.T. Bramwell and M.J.P. Gingras, Science 294, 1495 (2001).

[3] T. Kimura et al., Nature 426, 55 (2003); Nicola A. Hill, J. Phys. Chem. B 104, 6694 (2000).

[4] E.E. Sauerbrei *et al.*, Acta Cryst.B. 29, 2304 (1973).

[5] M. Kenzelmann *et al.*, Phys. Rev. B 74, 014429 (2006).

[6] G. Lawes *et al.*, Phys. Rev. Lett. 93, 247201, (2004).

[7] N.R. Wilson *et al.*, J. Magn. and Magn. Mat. 310, 1334 (2007).

[8] N. Rogado *et al.*, Solid State Comm. 124, 229 (2002).

[9] T. Lancaster *et al.*, Phys. Rev. B 75, 064427 (2007).

[10] Y. Chen *et al.*, Phys. Rev. B 74, 014430 (2006).

[11] G. Balakrishnan *et al.*, J. Phys.: Condens. Matter 16, L347 (2004).

[12] R. Szymczak *et al.*, Phys. Rev. B 73, 094425 (2006).

[13] arxiv.org. 0804.1929.

# Magnetic Excitations in CoO

**Z. Yamani [1], W.J.L. Buyers [1], D. Prabhakaran [2], and R.A. Cowley [2]**

[1] Canadian Neutron Beam Centre, National Research Council, Chalk River Laboratories, Chalk River, ON, Canada K0J 1J0

[2] Department of Physics, University of Oxford, Oxford, United Kingdom 0X1 3PU

The magnetic properties of cobalt compounds have recently attracted attention [1,2] because the Co ion may have transitions between high and low spin states giving rise to charge ordering, magnetic ordering and superconductivity. The recent interest in exotic oxides displaying superconductivity or orbital order emphasizes the importance of understanding simple oxides such as CoO. An earlier study provided an incomplete picture [3].

Cobaltous oxide is a face-centred cubic antiferromagnet in which (1 1 1) ferromagnetic sheets of spins stack antiferromagnetically along [1 1 1] directions below $T_N$ = 291 K with a ~ 1% contraction along a cube edge. At any wave-vector transfer, $Q$, up to as many as four spin-wave modes may arise from the domain and spin structure for any one transition from the ground state to one of the eleven excited spin and orbital states. The nearest neighbour antiferromagnetic exchange is frustrated, contributing no molecular field, and it is the antiferromagnetic next nearest neighbour exchange that breaks the symmetry below $T_N$. The nature of the order and fluctuations is still controversial [4,5].

In order to determine the nature of the three-dimensional ordering in the presence of the nearest neighbour frustration, we have made detailed measurements of the magnetic excitations in a high quality CoO crystal aligned in the (HHL) plane. Our previous high-resolution study indicated [6] that there are four resolved peaks at 6 K in the excitation spectrum between 4 and 12 THz for different magnetic zone centres. In a recent study, only two broad modes in the same spectral range were detected [7]. To gain more insight into the nature of these peaks, we determined the spectrum at other magnetic zone centres as well as at a few nuclear zone centres. In addition, we investigated these spectra at several temperatures below $T_N$ from 11 K to 150 K.

The inelastic neutron studies were performed at the C5 triple axis spectrometer with a vertically focusing PG(002) monochromator and a flat PG analyzer at a fixed final energy of $E_f$ = 3.52 THz for most of the scans. A fixed final energy of 7.36 THz was used at a few wave vectors either to be able to close the scattering triangle in the desired energy transfer range or to avoid large scattering angles that were not accessible. The horizontal collimations were set to [none, 0.48°, 0.56°, 1.2°] for which an energy resolution of 0.2 THz was achieved at zero energy transfer. One PG filter was used it the scattered side to suppress the higher order contamination.

The excitations observed at magnetic zone centres at 11 K are shown in Figure 1. Scans at lower energies (<4 THz) confirmed that there are no low energy modes of appreciable strength at any measured $Q$. For energy transfers between 4 and 14 THz, four excitations are observed at all zone centres. An analysis of the data including the $Co^{2+}$ magnetic form factor indicates that the peak at 9.5 THz is mainly magnetic in origin. The intensities of the peaks at 6.5 and 7.6 THz decrease with $Q$, but by less than the form factor, suggesting the peaks at 6.5 and 7.6 THz have some magnetic weight. The peak at 4.8 THz has a substantial phonon component. This lower energy ~ 5 THz mode lies close in frequency to the TA zone boundary phonon. This phonon has the same cross-section at (1/2 1/2 3/2), (3/2 3/2 1/2) and (5/2 5/2 1/2) zones centres, hence we conclude that this lowest peak carries largely phonon amplitude.

The temperature dependence of the excitations observed at magnetic zone centres was also measured. This study again supports the conclusion that the excitation at 9.5 THz is mainly magnetic, the 7.4 THz and 6.5 THz modes have some phonon contribution and finally the mode at 4.8 THz is mainly due to phonons, possibly through an incoherent process.

Similar scans at nuclear zone centres were also performed (see Figure 3 for an example). From these scans we find the (002) intensity for some modes is stronger than their intensity at (222). This suggests these modes are likely to be magnetic. In addition since the nuclear Bragg peaks are the same for all domains, the frequencies of the modes are the same irrespective of the magnetic domains. Hence it is concluded that the peaks at 6.7 and 7.6 THz are mainly magnetic and common to all domains.

Within each domain, there are several bands of spin excitations to states controlled by the exchange, spin–orbit and tetragonally distorted crystal field. Numerical calculations of these modes with a Hund's rule model suggest that the two out-of-plane domains give similar frequencies and so the domain structure accounts for three distinct modes. This leads to a different model than that proposed in recent low-resolution experiments [7].

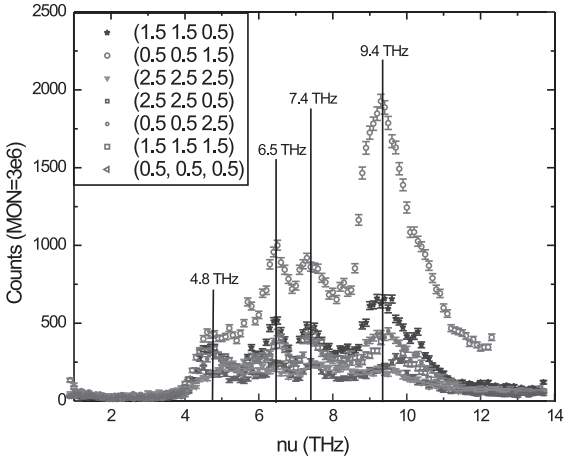


***Fig. 1*** *The observed excitations at several magnetic zone centres at 11 K. Data were collected at a fixed final energy of 3.52 THz except for (2.5 2.5 2.5) and (0.5 0.5 1.5) zone centres where a final energy of 7.36 THz was used.*

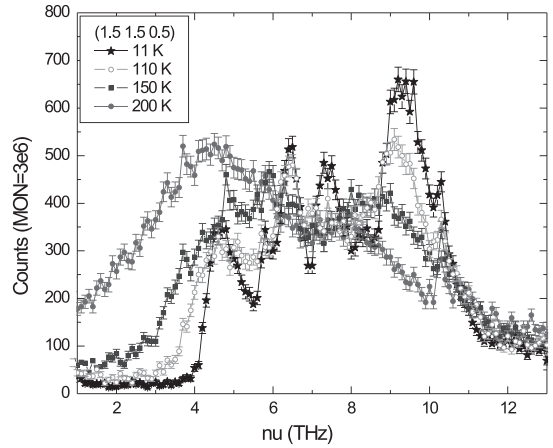


***Fig. 2*** *The temperature dependence of the excitations at (1.5 1.5 0.5) again suggesting that the excitation at 9.5 THz is mainly magnetic whereas the one at ~ 5 THz mainly arises from phonons. The excitations between 6 to 8 THz have some magnetic contributions.*

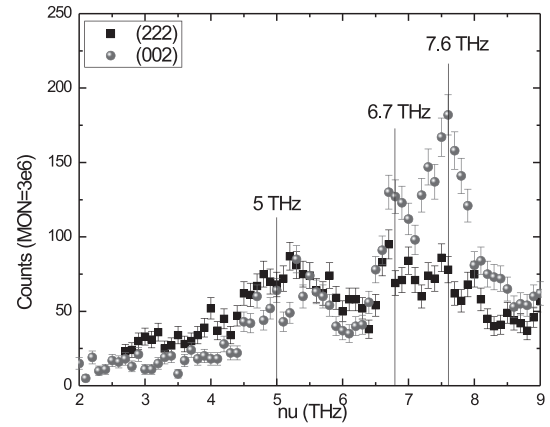


***Fig. 3*** *The observed excitations at nuclear zone centres (002) and (222). Data were collected at a fixed final energy of 3.52 THz and at 11 K.*

## References


[1] A.T. Boothroyd, et al., Phys. Rev. Lett. 92 (2004) 197201.

[2] W. Koshibae, S. Maekawa, Phys. Rev. Lett. 91 (2003) 257003.

[3] J. Sakurai, et al., Phys. Rev. 167 (1968) 510.

[4] E. Ressouche, et al., Physica B 385–386 (2006) 394.

[5] W. Jauch, et al., Phys. Rev. B 64 (2004) 052102.

[6] Z. Yamani et al., Physica B 403 (2008) 1406.

[7] K. Tomiyasu, S. Itoh, J. Phys. Soc. Japan 75 (2006) 084708.

# Polarized Neutron Scattering Study of Lightly Doped Superconducting YBCO6.33 ($T_c$ = 8.5 K)

**Z. Yamani [1], W.J.L. Buyers [1], R. Liang [2], D. Bonn [2], and W. N. Hardy [2]**

[1] Canadian Neutron Beam Centre, National Research Council, Chalk River Laboratories, Chalk River, ON, Canada K0J 1J0

[2] Physics Department, University of British Columbia, Vancouver, BC, Canada V6T 1W5

High temperature superconductors (HTSC) have a complex phase diagram. Hole doping drastically changes the magnetic properties of the antiferromagnetic (AF) insulating parent material eventually destroying long-range order. Superconductivity (SC) is observed for doping larger than a critical value ($p_c$) on the copper oxide planes. Understanding the properties of materials with doping levels close to the boundary of superconducting and long range AF ordered regions of the phase diagram may hold the key to unravelling the mechanism behind HTSC. For $La_{2-x}Sr_xCuO_4$ (LSCO) family, SC emerges from a non-metallic glassy phase whereas the precursor phase for $YBa_2Cu_3O_{6+x}$ (YBCO6+x) remains controversial. To investigate whether SC and long-range AF phases coexist in the YBCO6+x, we have studied a very underdoped crystal of YBCO6.33 with a superconducting transition temperature $T_c$ of only 8.5 K (less than 1/10 of the optimally doped $T_c$ = 94 K) and a hole density of only p ~ 0.055.

Our unpolarized neutron scattering study of the spin spectrum at low-energies in YBCO6.33 indicated [1] that there is no coexistence of superconductivity with long range ordered antiferromagnetism. Instead, we found that at low temperatures an elastic peak at the AF position $\boldsymbol{Q}$ = (0.5 0.5 L) with L = integer starts to grow gradually on cooling with no indication of a transition to a new phase. Although this peak remains resolution limited in energy, it has a finite width in $Q$-space both for spin correlations within the plane (~ 100 Å) and between planes (~ 25 Å). These short-range correlations indicate the coexistence of a glassy phase within the SC phase. In addition, we found that the spectrum of excitations out of this phase is in the form of a damped Lorentzian with a ~ 3 meV relaxation rate. This study showed that a second-order transition to long range Néel order either lies below the critical concentration for SC or that the transition is first order.

To separate magnetic from nuclear scattering as well as to investigate whether the central mode and its excitations exhibit a preferred spin orientation, we polarized the neutron beam at the C5 spectrometer. Flat Heuser-111 crystals were used both as monochromator and analyzer with a fixed final energy of $E_f$ = 3.52 THz and collimations were set to (0.8°, 0.85°, 2.4°) after the monochromator. No Soller collimation was used before monochromator resulting a 0.6° distance collimation (this is indicated as "none" in the collimations listed on the figures). A Mezei flipper coil was placed on the incident side and one graphite filter was used on the scattered side to suppress higher order neutrons. The Mezei flipper allowed spin-flip (SF) and non-spin-flip (NSF) cross sections to be measured. To control the direction of the neutron spin at the sample position two pairs of coils were used to apply a weak magnetic field (of ~ 3-5 G) either perpendicular to $\boldsymbol{Q}$ (vertical, VF) or parallel (horizontal, HF) to it (see Figure 1). Flipping ratios of ~ 15:1 and ~ 12:1 were measured for the vertical field and horizontal field configurations, respectively, using several Bragg reflections including (114) as well as using the straight through beam with the sample angle at the (114) position. For inelastic scans, the optimal flipping current at a given energy transfer was set automatically by the control program using an empirical relation between the flipping current and the initial energy ($E_i$). This relation was determined by measuring the optimal current at several initial energies using the straight through beam and was confirmed by measuring the flipping ratio at several Bragg reflections with final energies of $E_f$ = 3.52 and 7.37 THz.

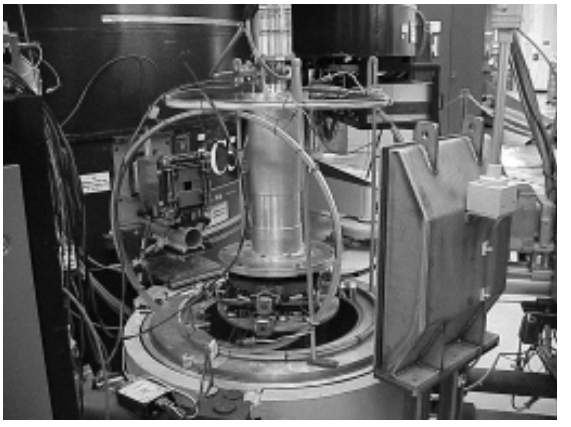

**Fig. 1** Two pairs of coils were used to control the direction of neutron spin at the sample position. The sample is mounted in the closed-cycle refrigerator (centre).

For each field configuration at the sample position, the sample was first warmed to 50 K and then field-cooled to low temperatures to prevent any possible depolarization from trapped flux in the Meissner state. For the horizontal field configuration, it was confirmed that during scans the field direction with respect to $\boldsymbol{Q}$ did not change more than a few degrees, hence the effects of depolarization on the neutron beam was minimal. For the vertical field configuration, the field orientation with respect to the sample was always perpendicular to the scattering plane, i.e. perpendicular to $\boldsymbol{Q}$.

Since neither the polarizer nor analyzer are perfect, there is always a small number of neutrons with the wrong spin

state that pass through and are counted at the detector. To correct for this and obtain the true SF scattering from the measured SF and NSF count rates, we used the following relation [2]

$$SF = C_{SF}\frac{F}{F-1} - C_{NSF}\frac{1}{F-1}$$

where F is the flipping ratio and $C_{SF}$ and $C_{NSF}$ are the measured SF and NSF count rates, respectively. Similarly the true NSF scattering was determined by the following correction

$$NSF = C_{NSF}\frac{F}{F-1} - C_{SF}\frac{1}{F-1}$$

The spin correlations, $S^{\alpha\alpha}(\boldsymbol{Q}, \omega)$, in the 2D $CuO_2$ planes along the [1 -1 0] α direction can be directly determined free of nuclear incoherent or phonon scattering (see Figure 2) by calculating the difference in the SF intensities of the HF and VF configurations (HF-VF) with the sample aligned in the (HHL) plane. In addition, a comparison of the observed SF intensity for HF vs. VF provides some information on the anisotropy of the magnetic scattering along the *ab*-plane vs. *c*-axis direction. For example, if the observed SF scattering for HF is twice as that for VF, the magnetic scattering along different directions is the same showing that the spin orientation is isotropic.

| | $H_o \| \| Q$ | | $H_o \perp Q$ | |
|---|---|---|---|---|
| | SF | NSF | SF | NSF |
| Nuclear coherent | 0 | 1 | 0 | 1 |
| Nuclear isotope incoherent | 0 | 1 | 0 | 1 |
| Nuclear spin incoherent | 2/3 | 1/3 | 2/3 | 1/3 |
| Magnetic | $S_x+S_y$ | 0 | $S_y$ | $S_x$ |

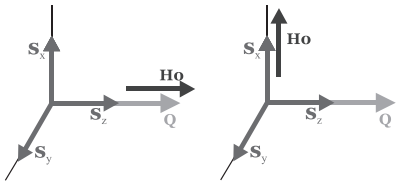


**Fig. 2** *Two configurations of the neutron spin at the sample position are shown. For each orientation, the contributions from nuclear and magnetic scattering are listed for both the spin-flip (SF) and non-spin-flip (NSF) components. The spin scattering cross-section $S^{\alpha\alpha}$ is denoted $\boldsymbol{s}_\alpha$.*

The polarized neutron scattering results confirm that both elastic and inelastic scattering observed previously with non-polarized neutrons are entirely magnetic in origin. Thus the methods we used in background subtraction for both scattering components correctly gave the magnetic component. The scattering is short ranged and is peaked at AF position (0.5 0.5 L) with L = integer. A comparison of the polarized with non-polarized data is provided in Figure 3 where the magnetic scattering obtained at low temperature along the (0.5 0.5 L) direction is shown.

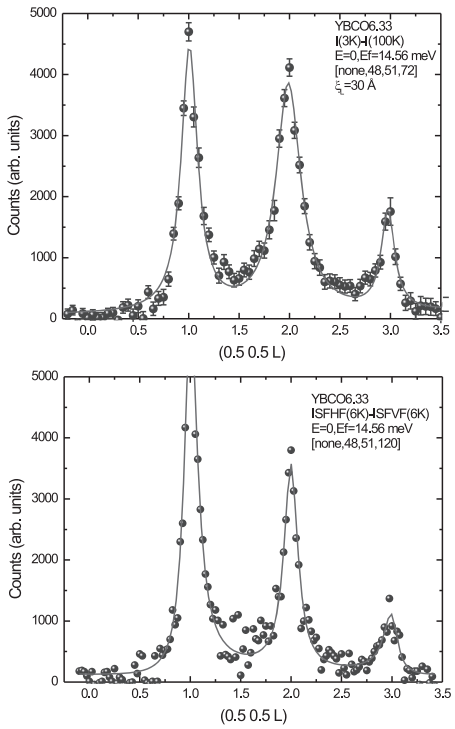


**Fig. 3** *Elastic magnetic scattering along the (0.5 0.5 L) obtained from the non-polarized study (top, low temperature minus high temperature background) compared to the polarized data (bottom, low temperature SF vertical field data is subtracted from the horizontal data).*

Typical H- and L- elastic SF scans are shown in Figure 4 for HF and VF configurations. It shows that the SF scattering with the horizontal field configuration is always twice that measured in the vertical field configuration. This is seen for scans both along the H- and L-directions and indicates that the spin coupling is unpolarized or paramagnetic in nature unlike the undoped parent compound where a strong anisotropy orients the spins preferentially in the *ab*-plane rather than along the *c*-axis.

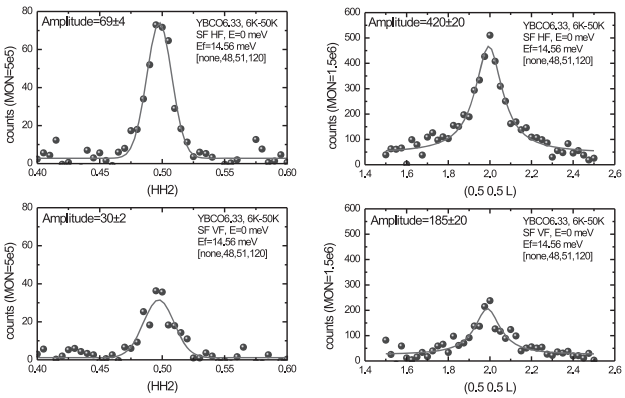


**Fig. 4** *SF scattering observed along the (HH2) for the HF (top left) and VF (bottom left) configurations. Similar scans are shown on the along the [0.5 0.5 L] direction (right panels).*

Our polarized data proves that the unpolarized response previously found to consist of two energy scales, a slow central peak response and faster spins relaxing at a rate of ~ 3 meV, does in fact arise from the magnetic spins. The inelastic spectrum obtained from the difference between

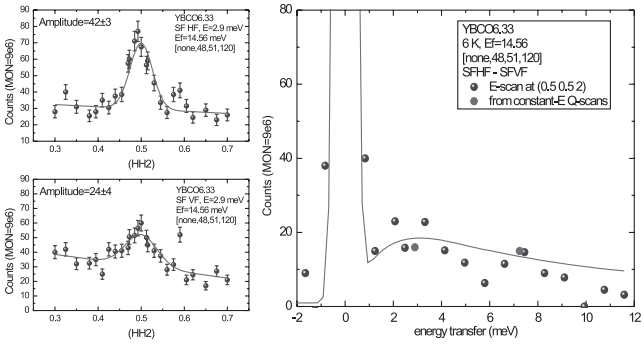


***Fig. 5*** *Polarized spin-flip inelastic neutron scattering data. Inelastic scans along [HH2] direction (left) show that the spin directions are isotropic since the HF intensity is twice that for VF. (right) The magnetic spectrum along [1,-1,0] measured by subtracting the VF from the HF data. The spectrum is fitted to a central mode and a modified Lorentzian (right line in the right panel).*

the horizontal spin-flip channel and the vertical field spin-flip channel as a function of energy transfer is shown in Figure 5. For inelastic scattering, we also find that the horizontal field SF scattering is always twice that measured in the vertical field configuration again indicating that the spin fluctuations are unpolarized or paramagnetic in nature.

The polarized study shows that the spin response is isotropic unlike the AF undoped parent compound with a strong in-plane anisotropy. It also confirms that the spin correlations coexist with superconductivity and remain short-ranged within $CuO_2$ planes and perpendicular to them, even for this very underdoped sample close to the edge of the superconducting phase. We conclude that the spins at this low doping are organized into a glassy state with unbroken orientational spin symmetry that coexists with superconductivity below $T_c$. Hence even lower doping than in YBCO6.33 is required for the long range AF phase to emerge.

## References

[1] Z. Yamani et al., *Physica C* 460–462 (2007) 430.

[2] A.R. Wildes, *Rev. Sci. Instrum.* 70 (1999) 4241.

# Magnetic Structure of Laves Phase [111]-Grown Superlattice: [50 $ErFe_2$/ 100 $YFe_2$]$_{40}$

**S. R. Jones [1], R. A. Cowley [1], and H. Fritzsche [2]**

[1] Department of Physics, University of Oxford, Oxford, United Kingdom OX1 3PU

[2] Canadian Neutron Beam Centre, National Research Council, Chalk River Laboratories, Chalk River, ON, Canada K0J 1J0

## Introduction

There is a long history of research into the rare earth - transition metal (R-T) intermetallic compounds in bulk form, based on the idea that the R and T atoms will interact to give useful properties. The R and T magnetic moments couple ferromagnetically when R is a light rare earth and antiferromagnetically when R is a heavy rare earth and magnetic interactions are possible that will raise the ordering temperature of the elemental rare earths - which have large localized moments - to above room temperature. This is the basis for the permanent magnet compounds $RT_5$ and $R_2T_{17}$, which are widely used in electric motors and other magnetomechanical devices.

Magnetic multilayer films of these compounds have become a subject of research due to their possible applications as permanent magnets [1]. The successful growth of $DyFe_2$/$YFe_2$ superlattices with [110] growth direction, which have magnetic moments aligned largely perpendicular to this direction, has demonstrated unusual exchange spring behavior as well as the existence of spin-flop phases in Y-rich materials [2], [3]. The direction of the moments depends on the composition of the superlattice. $ErFe_2$/$YFe_2$ [110] superlattices have also been grown and have the magnetic moments aligned largely along the growth direction. Magnetization measurements show that in an applied field they also show exchange spring behavior [4].

Recently it has become possible to grow $RT_2$, single layers and superlattices with [111] growth direction [5]. This is of interest as the [111] growth system also allows other R-T compounds such as $RT_3$ and $R_2T_{17}$ to be produced. Magnetization measurements on the $ErFe_2$/$YFe_2$ superlattice system using a SQUID magnetometer show that the easy axis of magnetization is along this growth direction and suggest that it is difficult to rotate the Er moments away from the easy axis by applying a perpendicular field.

## Experimental Arrangements

The superlattice discussed in this report has composition [50 $ErFe_2$/ 100 $YFe_2$]$_{40}$ and was prepared in the Balzers facility, Oxford using molecular beam epitaxy (MBE). $ErFe_2$ and $YFe_2$ have the face centred-cubic $MgCu_2$ structure and the super-lattice has the [111] direction as the growth direction. The notation used for the structure is [$t_1$Å $ErFe_2$/ $t_2$Å $YFe_2$]$_N$ where $t_1$ is the thickness of the $ErFe_2$ layer, $t_2$ is that of the $YFe_2$ layer and $N$ is the number of layers. It was grown as detailed in ref. [5]. X-ray diffraction measurements [5] have shown that this sample is composed of two epitaxial domains: one with the [111] direction parallel to the growth direction, the other with this direction anti-parallel to the growth direction.

Polarized neutron reflectivity and unpolarized neutron diffraction measurements were carried out on the C5 spectrometer. The sample was oriented with the growth direction ([111] direction) horizontal and perpendicular to the incoming neutron beam and with the [11$\bar{2}$] or [$\bar{1}$1$\bar{2}$] direction parallel to the beam. A vertical magnetic field was applied, perpendicular to both the superlattice growth direction and the beam direction. The diffraction measurements were taken at the (111), (220), and (113) Bragg reflections at fields starting at -7.5 T and increasing up to 6 T, field cooled at -7.5 T, at temperatures of 100 K and 200 K. Reflectivity measurements were taken at fields between 0 T and 6 T, also at 100 K and 200 K. Theoretical calculations of the reflectivity were produced using the `Polly: Polarised Neutron Reflectivity' program developed by S.Langridge at the Rutherford Appleton Laboratory, Oxfordshire, UK.

Erbium and Yttrium have very similar neutron scattering lengths: 7.79 fm and 7.75 fm respectively. Consequently, the subsidiary peaks due to the superlattice will not be visible unless the $ErFe_2$ and $YFe_2$ layers have different magnetizations.

## Results and Discussion

*Reflectivity*

Figure 1 shows the polarized neutron reflectivity of a [50 $ErFe_2$/ 100 $YFe_2$]$_{40}$ superlattice. This was measured at 100 K with an applied field of 3 T perpendicular to the neutron beam and to the growth direction of the sample.

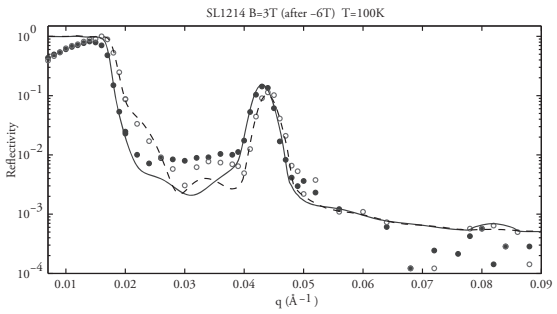


**Fig. 1** Reflectivity of a [50 $ErFe_2$/ 100 $YFe_2$]$_{40}$ superlattice at 100 K and 3 T (after -6 T). Filled circles show the up-up measurement, open circles show the down-down measurement. Theoretical calculations are shown as a solid line (up-up) and a dashed line (down-down).

The features are typical of all of our neutron reflectivity measurements on this sample. The filled circles show the up-up measurement, the open circles show the down-down measurement. The up-down and down-up measurements were also recorded and showed that there was no spin-flip scattering. The first order superlattice peak can be clearly seen at $q \approx 0.043$ Å. However, the second order peak, expected at $q \approx 0.081$ Å, is not observed in this or in any of the reflectivity measurements taken. This absence should not be due to structural imperfections in the superlattice, as x-ray reflectivity measurements on this sample show several orders of superlattice peaks.

A model is necessary for the magnetization profile of the sample that produces no spin-flip intensity and also reduces the intensity of the second reflectivity superlattice peak. One such model, shown schematically in figure 2, is that of a magnetic exchange spring forming in the soft $YFe_2$ layers while the magnetic moment of the strongly anisotropic $ErFe_2$ layer remains aligned along the growth axis of the superlattice.

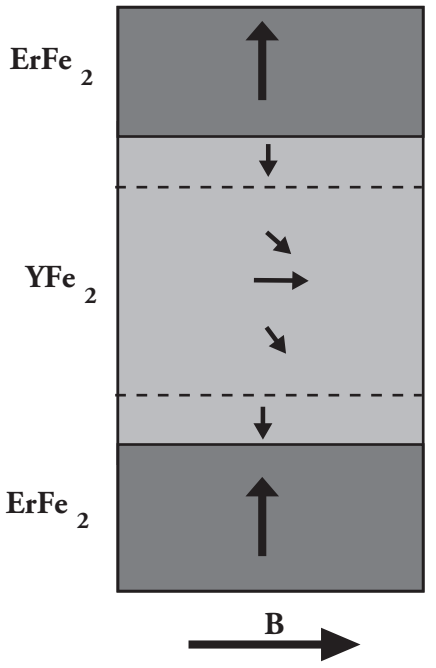


**Fig. 2** Schematic diagram of the proposed magnetization of the superlattice.

In our model, the magnetic moments of the $YFe_2$ layers are anti-aligned with those of the $ErFe_2$ layers (along the [111] growth direction) for 12 Å from the $ErFe_2/YFe_2$ interface due to the strong coupling between the Fe moments in both compounds. Further into the $YFe_2$ layers the magnetization rotates away from the [111] direction towards the direction of the applied magnetic field. In the largest applied fields the magnetization at the center of the $YFe_2$ layers becomes parallel to the applied field; for smaller applied fields the magnetization is still at an angle to the applied field.

*Diffraction*

Figure 3 shows the integrated intensities of the scattering from the (111), (220) and (113) Bragg reflections at 100 K in applied magnetic fields of between 0 T and 6 T. The intensities are normalized to their values at 0 T. As the nuclear structure factors are constant, changes in these intensities are attributed to variation in the magnitude and direction of the magnetization of the sample. The magnetic structure factor is at a maximum for $q$ perpendicular to the magnetization and at a minimum for $q$ parallel to the magnetization.

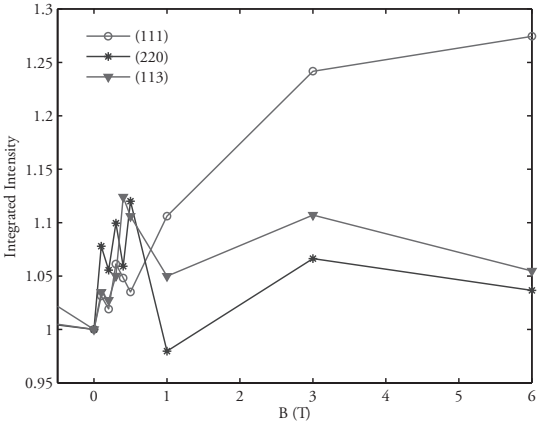


**Fig. 3** Integrated intensities of the (111), (220) and (113) Bragg reflections at 100 K.

The intensity of the (111) reflection increases as the field is increased. This suggests a rotation of the sample magnetization away from the [111] direction. A reduction in the intensities of the (113) and (220) reflections can be seen at B = 1 T. This indicates that the magnetization of the sample rotates through the [113] and [220] directions as the field increases from 0.5 T to 3 T. As the sample contains two domains, both of these directions lie between the [111] direction and the direction of the applied magnetic field.

## Conclusions

Polarized neutron reflectivity and unpolarized neutron diffraction measurements have been made on a $[50\ ErFe_2/100\ YFe_2]_{40}$ superlattice sample with a [111] growth direction. The reflectivity data suggests a model for the magnetization in which the magnetic moments in the $ErFe_2$ layers are aligned with the growth direction and those in the $YFe_2$ layers form exchange springs, rotating away from the growth direction towards the direction of the applied magnetic field (the [112] direction).

Diffraction measurements were made around the (111), (220) and (113) Bragg reflections. Analysis of the integrated intensity of these Bragg reflections shows that the magnetization of the superlattice rotates away from the [111] growth direction as the applied field increases and

goes through the [113] and [220] directions as the field reaches ~ 2 T. As these two axes lie between the [111] and [11$\overline{2}$] directions, this diffraction data supports the model, suggested by the reflectivity measurements, of exchange springs in the $YFe_2$ layers which rotate from the [111] direction towards the [11$\overline{2}$] direction.

### References


[1] J. M. D. Coey. Permanent magnetism. Solid State Commun., 102:101, 1997.

[2] M. Sawicki, G. J. Bowden, P. A. J. de Groot, B. D. Rainford, J.-M. L. Beaujour, R. C. C. Ward, and M. R. Wells. Exchange springs in antiferromagnetically coupled $DyFe_2$ – $YFe_2$ superlattices. Phys. Rev. B, 62:5817, 2000.

[3] M. J. Bentall, R. A. Cowley, W. J. L. Buyers, Z. Tun, W. Lohstroh, R. C. C. Ward, and M. R. Wells. Magnetic structures of laves phase superlattices. J. Phys.: Condens. Matter, 15:4301, 2003.

[4] K. N. Martin, K. Wang, G. J. Bowden, A. A. Zhukov, P. A. J. de Groot, J. P. Zimmermann, H. Fangohr, and R. C. C. Ward. Exchange spring driven spin flop transition in ErFe2 / YFe2 multilayers. App. Phys. Lett., 89:132511, 2006.

[5] S. R. Jones, A. Dunhill, R. A. Cowley, and R. C. C. Ward. Structure of epitaxially grown rare-earth intermetallics using x-ray diffraction: RT2, RT3, RT5, and R2T17. Phys. Rev. B, 77:214110, 2008.

# Spin Fluctuations in $La_{2-x}Sr_xCu_{1-y}Zn_yO_4$ (x = 0.25, y = 0.02)

**S. Wilson [1], B. Freelon [1], R. Birgeneau [1], Z. Yamani [2], and W.J.L. Buyers [2]**

[1] UC Berkeley and Lawrence Berkeley National Lab, Berkeley, CA, USA 94720-1500

[2] Canadian Neutron Beam Centre, National Research Council, Chalk River Laboratories, Chalk River, ON, Canada K0J 1J0

Neutron scattering studies of both elastic and dynamic spin ordering across the phase diagram of the prototypical, monolayer cuprate $La_{2-x}Sr_xCuO_4$ (LSCO) have shown a clear coupling between the existence of incommensurate, stripe-like, spin density wave (SDW) states and the presence of the high-$T_c$ superconducting phase [1]. Undoped, LSCO (along with all other cuprates) is a long-range ordered, antiferromagnetic (AF) insulator. Upon doping however, the long range AF order is rapidly suppressed in favor of an incommensurate SDW state. In superconducting concentrations, this SDW phase manifests itself through an incommensurate quartet of magnetic peaks about the $\mathbf{Q}_{inplane}$ = (0.5, 0.5±δ), (0.5±δ, 0.5) wave vectors similar to those observed in systems exhibiting a known stripe ordered phase such as $La_{1.6-x}Nd_{0.4}Sr_xCuO_4$ (with x = 0.12) [3]. Near optimal doping in LSCO (x ~ 0.15), the static SDW order breaks down and a well defined spin gap opens; however at low energies strong spin fluctuations remain distributed along the incommensurate SDW wave vectors $\mathbf{Q}_{inplane}$ = (0.5, 0.5±δ), (0.5±δ, 0.5). Upon continued Sr doping into the overdoped regime, this magnetic response becomes overdamped and spin excitations are suppressed concomitantly with superconductivity [4]. At 30% Sr doping, no discernable magnetic response remains – simultaneous to the disappearance of $T_c$. An effective route to study this microscopic coupling between SC and the incommensurate SDW states in LSCO further was realized by perturbing the superconducting state through the introduction of non-magnetic impurities (such as Zn) into the CuO planes and characterizing the resulting modification to the system's spin behavior.

The substitution of only a small amount of nonmagnetic $Zn^{2+}$ impurities onto the Cu-sites in the $La_{2-x}Sr_xCu_{1-y}Zn_yO_4$ compound (LSCZO) results in a dramatic suppression of the superconducting phase [5]. Early transport measurements theorized that this Zn-substitution in fact stabilized stripe order at the expense of superconductivity; however neutron work subsequently uncovered that the Zn effect is to localize magnetic states within the spin gap of nearly optimally doped LSCO rather than merely closing the spin gap, as would be naively expected for stabilizing a dynamic stripe phase [6]. These subgap states have since been theorized to originate from a "Swiss cheese" picture of non-superconducting islands consisting of localized Cu moments induced in a halo about the Zn impurities within the superconducting planes [7]. Further experiments, however, have suggested that instead islands of superconducting regions form in which AF correlations coexist (and support electron pair formation), and these islands are intermixed within regions of Fermi-liquid, non-superconducting electronic states (about the Zn sites) [8]. This latter interpretation was introduced in order to explain experiments on Zn substituted, highly overdoped LSZCO (x = 0.25, y = 0.01) samples. These experiments demonstrated that the effect of Zn doping into LSZCO (x = 0.25, y = 0.01) was to surprisingly enhance the severely damped incommensurate magnetic scattering observed in overdoped LSCO [4]. The characteristic energy scale in the local susceptibility of Zn-free LSCO (x = 0.25) and Zn-doped LSZCO (x = 0.25, y = 0.01) remained identical in strong contrast to the subgap behavior reported for Zn doping into the LSZCO (x = 0.15, y = 0.01) system [6].

In order to understand the spin behavior in the overdoped regime further, we conducted experiments on the LSCZO (x = 0.25, y = 0.02) system in which we mapped out the spin fluctuations about the incommensurate SDW wave vectors at energies from $\Delta E$ = 3 meV to 12 meV on the C5 spectrometer. For this experiment, we coaligned 3 large single crystals LSCZO (x = 0.25, y = 0.02) within the [H,K,0] plane and mounted them in a closed cycle cooling cryostat. A fixed final energy of $E_f$ = 14.7 meV was used and one PG filter was placed before the analyzer. Both monochromter (vertically focusing) and analyzer (flat) crystals were PG, and two different collimation settings were used: 33'-35'-40'-120' (tight) and 33'-48'-51'-120' (loose). To determine the spin excitation dispersion relation, we performed constant energy $Q$-scans around the (0.5, 0.5, 0) point in reciprocal space at different energy transfers. Figure 1 shows a typical $Q$-scan through (H, 0.5, 0) at 2 THz energy transfer and 6 K.

Our results reveal a surprising dispersion in the spin excitations about (0.5, 0.5), which is modified from the nearly dispersionless Zn-free LSCO (x = 0.25) response at these energies. Figure 2 shows this dispersion which strikingly resembles a renormalized version of the hour-glass type dispersion reported in optimally doped LSCO (x = 0.15); albeit the dispersion in this Zn-doped sample never truly reaches the commensurate position at $E_R$ ~ 7 meV. The energy, $E_R$, with the minimum $\delta Q$ from the commensurate in-plane (0.5, 0.5) position however corresponds to the renormalized energy scale of superconductivity in this system with $T_c$ ~ 11 K, which would obey the linear relationship between $E_R$ and $T_c$ observed within other classes of cuprates ($E_R \sim 6k_BT_c$). The magnetic spectral weight for excitations below 12 meV also seems to retain its peak around 8 meV, similar to the reported results of more lightly Zn-doped samples of LSCZO (x = 0.25, y = 0.01).

The precise temperature dependence of this anomalous dispersion and the possible existence of inelastic spin signal at higher energies are the next natural step in this study and will be the focus of future experiments.

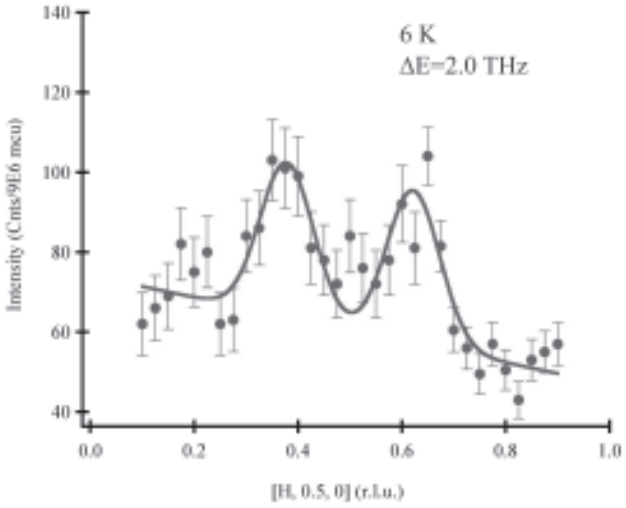


***Fig. 1*** *Q-scan through (H, 0.5, 0) at 2 THz energy transfer and at 6 K showing a typical fit utilized to determine the dispersion in LSCZO (x = 0.25, y = 0.02).*

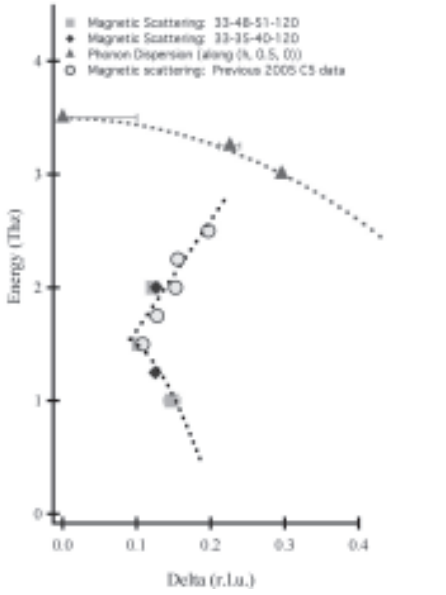


***Fig. 2*** *Dispersion of spin excitations and interfering phonon through (0.5± δ, 0.5) and equivalent positions. δ values represent the average displacement of the four incommensurate spin excitations from the (0.5, 0.5) position using the tetragonal unit cell.*

### References


[1] R. J. Birgeneau et al., JPSJ 75, 80301 (2006).

[2] J. Tranquada arXiv:condmatt:0512112v1 (2005).

[3] J. Tranquada et al., Nature 375, 561 (1995).

[4] S. Wakimoto et al., PRL 92, 217004 (2004).

[5] Fukuzumi et al., PRL 76, 684 (1996).

[6] H. A. Kimura et al., PRL 91, 067002 (2003).

[7] B. Nachumi et al., PRL 77, 5421 (1996).

[8] S. Wakimoto et al., PRB 72, 064521 (2005).

# Three Dimensional Magnetic Correlations in Multiferroic $LuFe_2O_4$

**A.D. Christianson [1], M.D. Lumsden [1], M. Angst [1], Z. Yamani [2], W. Tian [1,3], R. Jin [1], E.A. Payzant [1], S.E. Nagler [1], B.C. Sales [1], and D. Mandrus [1]**

[1] Oak Ridge National Laboratory, Oak Ridge, TN, USA 37831

[2] Canadian Neutron Beam Centre, National Research Council, Chalk River Laboratories, Chalk River, ON, Canada K0J 1J0

[3] Ames Laboratory, Iowa State University, Ames, Iowa, USA 50011

Multiferroic materials have been investigated for many years, but only recently have materials been found which exhibit effects large enough to be useful in devices. In this new class of materials, the ferroelectricity originates as part of a more complex phenomenon [1]. For example, in $LuFe_2O_4$ at high temperatures, $Fe^{2+}$ and $Fe^{3+}$ ions are found in equal numbers but are randomly distributed. At temperatures below 320 K, the $Fe^{2+}$ and $Fe^{3+}$ ions order (charge order) leading to the formation of a ferroelectric polarization [2]. At 240 K, magnetic order appears along with a simultaneous anomaly in the electric polarization indicating a coupling between the magnetic and ferroelectric degrees of freedom in $LuFe_2O_4$. An additional demonstration of coupling between magnetic and electric degrees of freedom in $LuFe_2O_4$ is provided by dielectric constant measurements under applied magnetic fields which show a giant magnetocapacitance at room temperature [3]. Hence, $LuFe_2O_4$ appears to be a promising multiferroic material.

To provide further insight into the interesting behavior of $LuFe_2O_4$ we have performed neutron diffraction measurements on high quality single crystals. These measurements were performed on the N5 and C5 (for the polarized work) triple-axis spectrometers, Chalk River, Canada. Further measurements were also performed with the HB1 triple-axis spectrometer at HFIR at Oak Ridge National Laboratory. For the non-polarized experiment at N5, pyrolytic graphite (PG-002) flat monochromator and flat analyzer were used. Measurements were performed with a fixed final neutron energy of $E_f$ = 13.7 meV and a PG filter in the incident beam to remove higher order contamination. Horizontal collimations were set to (none, 0.6°, 0.27°, 1.1°). For polarized experiments on C5, flat Heuser-111 crystals were used both as monochromator and analyzer with a fixed final energy of $E_f$ = 13.7 meV and collimations set to (none, 0.8°, 0.85°, 2.4°). A Mezei flipper coil was placed on the incident side and two graphite filters were used on the scattered side to suppress the higher order neutrons. The Mezei flipper allowed spin-flip and non-spin-flip cross sections to be measured. At the sample position a pair of coils applied a weak vertical field perpendicular to $\boldsymbol{Q}$ (of ~ 3-5 G) to control the direction of the neutron spin at the sample. A flipping ratio of ~ 15:1 was achieved for this vertical field configuration.

Our study shows that in contrast to previous work, there are two transitions, one at 240 K ($T_N$) and another at 175 K ($T_L$) [4]. The nature of ordering which occurs at each of these transitions can be examined by comparing scans along the (1/3 1/3 L) direction (Figure 1a) at various temperatures. The scan at 280 K shows weak peaks at large values of L with ½ integer indices. These peaks are not magnetic and in accord with previous work they are attributed to the onset of 3D charge order at 320 K [5]. Comparing the data at 220 K to that at 280 K (where there is no long range magnetic order) shows new intensity appearing on peaks at integer and half-integer values of L with strongest enhancement at small L values. Such enhanced scattering at small L values is expected for scattering from the ordered magnetic moments of $Fe^{2+}$ and $Fe^{3+}$.

To explicitly check which contributions of the scattering are due to magnetic and/or charge order we performed polarized neutron diffraction measurements on the C5 spectrometer. The results of these measurements are shown in Figure 1(b). The scattering in the spin flip channel is magnetic and the lack of scattering in the non-spin flip channel at small L values provides confirmation that the magnetic moments point along the *c*-axis. Thus, the neutron scattering data demonstrates 3D magnetic correlations below 240 K in $LuFe_2O_4$.

To constrain models for the spin configuration in $LuFe_2O_4$, a large number of reflections were measured at 220 K by scanning along the (1/3 1/3 L), (2/3 2/3 L), and (4/3 4/3 L) directions. To solve for the magnetic structure, representational analysis was performed to consider those magnetic structures that are symmetry allowed from the parent R-3m space group. From this analysis we concluded that the spin configuration is described by a ferrimagnetic structure with ordering wavevector (1/3 1/3 0), the presence of ½-integer reflections occurring as a result of the charge ordering which decorates the lattice with differing magnetic moment on $Fe^{2+}$ and $Fe^{3+}$ sites with a periodicity of (1/3 1/3 ½). A ferrimagnetic model consistent with the representational analysis provides good agreement with the data. The proposed magnetic structure shown in Figure 2 has 2/3 of the spins pointing in one direction and 1/3 in the opposite direction.

Below $T_L$, profound changes occur in the magnetic scattering as shown in Figure 1 (a). In particular, a component to the scattering builds up which is extremely broad along (1/3 1/3 L) but sharp along (HH0). Figure 1 (a) also shows that below $T_L$ significant changes occur in the magnetic peaks along (1/3 1/3 L). The intensity along (1/3 1/3 L) for

magnetic reflections changes rather dramatically with some peaks becoming more intense (e.g. (1/3 1/3 1)) and some peaks becoming less intense (e.g. (1/3 1/3 0)). Thus, 3D magnetic correlations persist below $T_L$ albeit with a shorter correlation length than found for $T_N$. Finally, we note that scans along (110) have revealed the existence of a new set of satellite peaks indexed as (1/3±δ 1/3±δ 3L/2) where δ ~ 0.027 (not shown) below $T_L$.

In conclusion, we show that that $LuFe_2O_4$ has two transitions below 300 K. Both of these transitions involve a 3D magnetically correlated structure with a finite correlation length along the *c*-axis. The degree to which the correlation length is an intrinsic property or is the result of disorder, most likely oxygen stoichiometry, is yet to be elucidated. Below $T_N$ a ferrimagnetic spin configuration is found with a magnetic propagation vector of (1/3 1/3 0) with magnetic intensity occurring at (1/3 1/3 L) where L is a half-integer arising due to the charge ordering at 320 K. Theoretical models taking into account the 3D nature of the magnetic interactions as well as the sequence of magnetic phase transitions described above should provide additional insight into the multiferroic behavior of $LuFe_2O_4$.

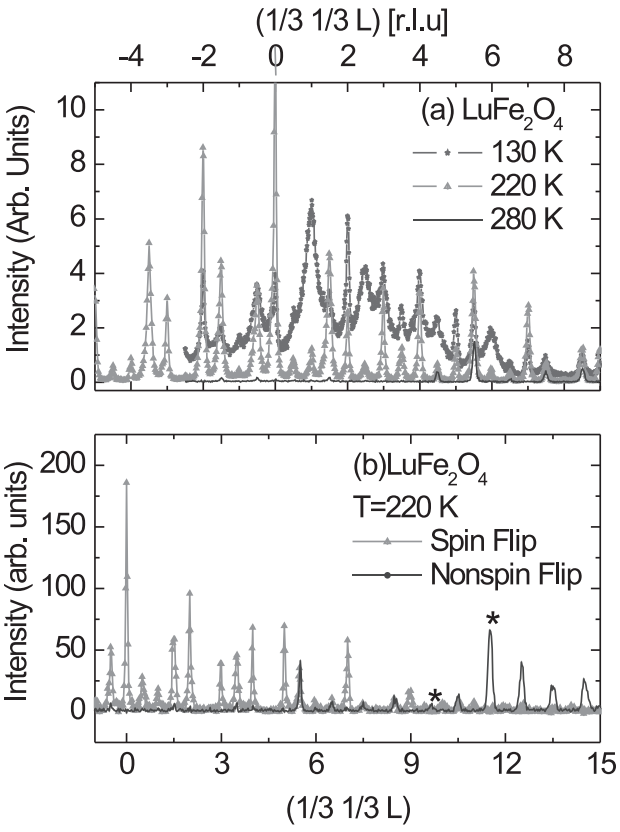


**Fig 1.** (a) Scans along (1/3 1/3 L) at several temperatures showing the changes to the scattering below $T_N$ (240 K) and $T_L$ (175 K). (b) Polarized neutron scattering data along (1/3 1/3 L). The * indicate peaks contaminated by aluminum background scattering.

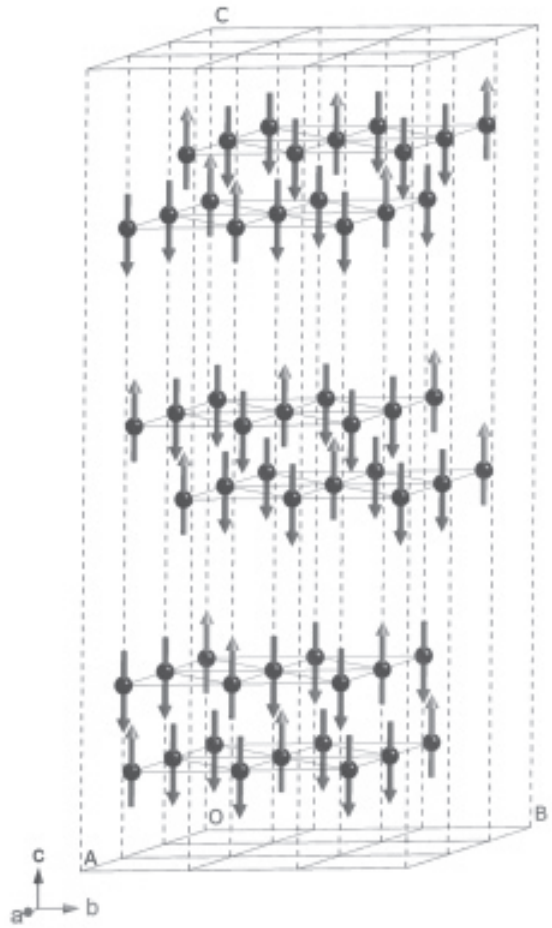


**Fig 2.** The ferrimagnetic structure determined below 240 K.

### References


[1] S.-W. Cheong and M. Mostovoy, Nature Materials 6, 13 (2007).

[2] A. D. Christianson, et al., Phys. Rev. Lett. 100, 107601 (2008).

[3] N. Ikeda, et al., Nature 436, 1136 (2005).

[4] M.A. Sibramanian, et al., Adv. Mater. 18, 1737 (2006).

[5] Y. Yamada, et al., Phys. Rev. B 62, 12167 (2000).

# Quantum Spin Excitations through the Metal-to-Insulator Crossover in $YBa_2Cu_3O_{6.45}$ ($T_c$ = 48 K)

**S. Li [1], Z. Yamani [2], H.J. Kang [3,4], K. Segawa [5], Y. Ando [6], X. Yao [7], H. A. Mook [8], P. Dai [1,8]**

[1] Department of Physics and Astronomy, The University of Tennessee, Knoxville, Tennessee, USA 37996-1200
[2] Canadian Neutron Beam Centre, National Research Council, Chalk River Laboratories, Chalk River, ON, Canada K0J 1J0
[3] NIST Center for Neutron Research, National Institute of Standards and Technology, Gaithersburg, Maryland USA 20899-8562
[4] Department of Materials Science and Engineering, University of Maryland, College Park, Maryland USA 20742-6393
[5] Central Research Institute of Electric Power Industry, Komae, Tokyo, Japan 201-8511
[6] Institute of Scientific and Industrial Research, Osaka University, Ibaraki, Osaka, Japan 567-0047
[7] Department of Physics, Shanghai Jiaotong University, Shanghai, People's Republic of China 200030
[8] Neutron Scattering Sciences Division, Oak Ridge National Laboratory, Oak Ridge, Tennessee, USA 37831-6393

## Abstract

We use inelastic neutron scattering to study the temperature dependence of the spin excitations of a detwinned superconducting $YBa_2Cu_3O_{6.45}$ ($T_c$ = 48 K). In contrast to earlier work on $YBa_2Cu_3O_{6.5}$ ($T_c$ = 58 K), where the prominent features in the magnetic spectra consist of a sharp collective magnetic excitation termed "resonance" and a large ($\hbar\omega$= 15 meV) superconducting spin gap, we find that the spin excitations in $YBa_2Cu_3O_{6.45}$ are gapless and have a much broader resonance. Our detailed mapping of magnetic scattering along the *a*/b**-axis directions at different energies reveals that spin excitations are anisotropic and consistent with the "hourglass"-like dispersion along the a*-axis direction near the resonance, but they are isotropic at lower energies. Since a fundamental change in the low-temperature normal state of $YBa_2Cu_3O_{6+y}$ when superconductivity is suppressed takes place at y ~ 0.5 with a metal-to-insulator crossover (MIC), where the ground state transforms from a metallic to an insulating-like phase, our results suggest a clear connection between the large change in spin excitations and the MIC. The resonance therefore is a fundamental feature of metallic ground state superconductors and a consequence of high-$T_c$ superconductivity. Here we describe our findings that are published in [1].

## Materials

A solute-rich liquid pulling method was used to grow a large pure YBCO crystal without any impurity phase for our neutron scattering study. The crystal was cut into four pieces with a total mass of 6 grams and the oxygen content was set to y = 0.45 at one atmosphere with 0.5% oxygen partial pressure at 550°C for 5 days. The samples were mechanically de-twinned at 220°C and then annealed in sealed tube at 90°C for more than three weeks. The samples have well-established Ortho-II CuO chain ordering with 90% de-twinning ratio and sharp $T_c$.

## Methods

The neutron scattering measurements were taken on the C5 thermal triple axis spectrometer with $E_f$ = 14.7 meV and with PG(002) as both a vertically focusing monochromator and flat analyzer. Two PG filters with a total thickness 10 cm in the scattered beam removed high-order neutron wavelengths. Fast neutrons were removed from the incident beam by liquid nitrogen cooled sapphire filter before monochromator. The horizontal collimations were controlled with Soller slits and set at 30'-48'-51'-144' for [*H,H,L*] zone or 30'-28.6'-33.4'-144' for [*H,K,*4*K*/3] and [*H,K,*4*H*/3] zones.

## Results

To search for a neutron spin resonance in $YBa_2Cu_3O_{6.45}$, we note that the intensity of the neutron spin resonance increases below $T_c$ like an order parameter and its energy tracks $T_c$ as the oxygen composition is varied via $E_R = 5.8\ k_BT_c$. Since $YBa_2Cu_3O_{6.45}$ has $T_c$ = 48 K, we expect the mode to occur at energies around 20 meV. Figure 1a shows energy scans at wave vector $\boldsymbol{Q}$ = (1/2, 1/2, 5) below and above $T_c$. Consistent with earlier results on higher-doping YBCO, the raw data are dominated by phonon scattering at 20 meV and ~ 30 meV at both temperatures. However, when one takes the temperature difference spectra below and above $T_c$, a broad peak with a full-width-half-maximum (FWHM) of ~ 15 meV emerges at $\hbar\omega \approx 19$ meV (Figure 1c). Since intensity of phonons should decrease with decreasing temperature and the Bose population factor does not much affect the magnetic scattering above 10 meV from 5 to 55 K, the net intensity gain in Figure 1a must be the result of enhanced dynamic susceptibility below $T_c$. Although such intensity gain below $T_c$ is a hallmark of the resonance, the observed broad energy peak is quite different from the instrumental resolution-limited resonance for YBCO at higher doping levels.

To see if the intensity gain below $T_c$ is consistent with the bilayer $Cu^{2+}$ acoustic magnetic excitations from YBCO, we carried out energy scans at the equivalent acoustic wavevector $\boldsymbol{Q}$ = (0.5, 0.5, 1.8) and Figure 1b summarizes the temperature dependence of the susceptibility $\chi''(Q,\omega)$. Consistent with the cold neutron data measured at SPINS, NIST, $\chi''(Q,\omega)$ is proportional to $\hbar\omega$ above $T_c$, and increases with decreasing temperature. The difference spectrum $\Delta\chi''(Q,\omega)$ in Figure 1d shows a clear peak in susceptibility. Figures 1e-g show wavevector dependence of $\chi''(Q,\omega)$ at $\hbar\omega$ = 8, 12, and 24 meV below and above $T_c$. The superconductivity-induced susceptibility gain increases from 12 to 24 meV (see Figure 1), and there is substantial magnetic scattering even at 250 K.

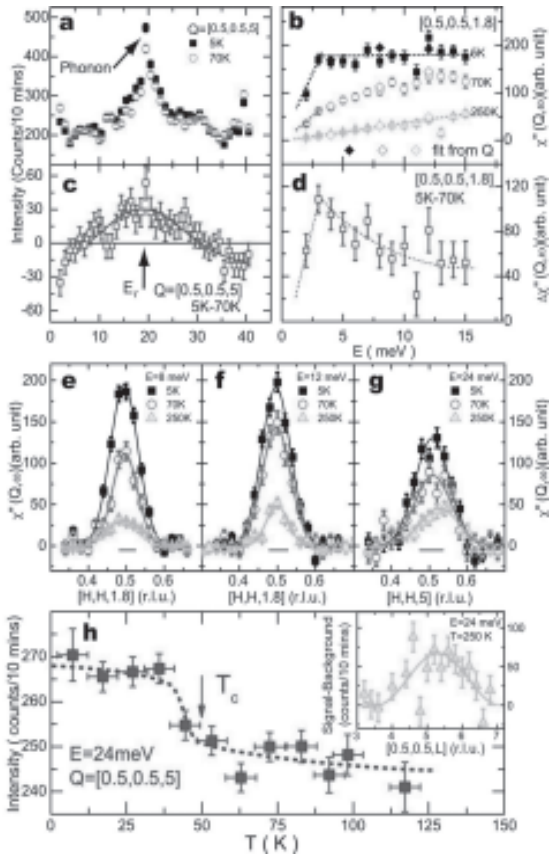


**Fig. 1** *(a), Energy-scans at* $\boldsymbol{Q}$ *= (1/2, 1/2, 5) taken below and above* $T_c$*. The difference in (c) shows a clear peak centered around 20 meV with a FWHM of 15 meV. (b), Temperature dependence of the dynamic susceptibility at the equivalent position* $\boldsymbol{Q}$ *= (1/2, 1/2, 1.8) showing clear magnetic intensity gain on cooling. (d) The temperature difference in dynamic susceptibility. (e)-(g) Wavevector dependence of dynamic susceptibility along the [H,H] direction at different energies and temperatures. (h), The temperature dependence of the scattering at 24 meV and (1/2, 1/2, 5) shows an order-parameter-like increase below* $T_c$*.*

To confirm that the observed scattering at 250 K is from acoustic magnetic excitations in YBCO, we carried out *Q*-scans along the *c*-axis direction and found that the L-modulation of the $\hbar\omega$ = 24 meV excitation at 250 K follows the expected acoustic bilayer structure factor (see inset of Figure 1h). Finally, the temperature dependence of the scattering at $\boldsymbol{Q}$ = (0.5, 0.5, 5) and $\hbar\omega$ = 24 meV shows an order parameter-like increase below $T_c$ similar to the temperature dependence of the resonance in the higher-doping YBCO. These results thus demonstrate that the broad peak centered at $\hbar\omega$ = 19 meV is indeed the magnetic resonance similar to other superconducting cuprates.

Having shown the presence of the resonance in our $YBa_2Cu_3O_{6.45}$, it is important to determine its dispersion to allow a direct comparison between the magnetic spectra of underdoped YBCO and LSCO. Previous neutron scattering work on YBCO with y = 0.5, and 0.6 have shown [2] that the dispersion of the resonance has the hour-glass shape, with incommensurate scattering below the resonance being anisotropic, having a magnetic anisotropy with a larger incommensurability along the $a^*$-axis direction than the $b^*$-axis direction. Since the low-energy spin fluctuations in our $YBa_2Cu_3O_{6.45}$ are commensurate, it will be interesting to determine the dispersion of spin excitations along *H* and *K* directions near the resonance. To accomplish this, we co-aligned the samples in either the [*H,K,*4/3*K*] or [*H,K,*4/3*H*] zone by simply rotating them 90 degrees along the $c^*$-axis in the [*H,K,*0] zone before tilting around the $a^*$($b^*$)-axis. The unique advantage of such experimental geometries is that one can carry out scans along the [*H*,1.5,2] or [-1.5,*K*,2] directions with identical instrumental resolution, thus allowing a direct comparison of the possible magnetic anisotropy in this material (Figures 2a,b).

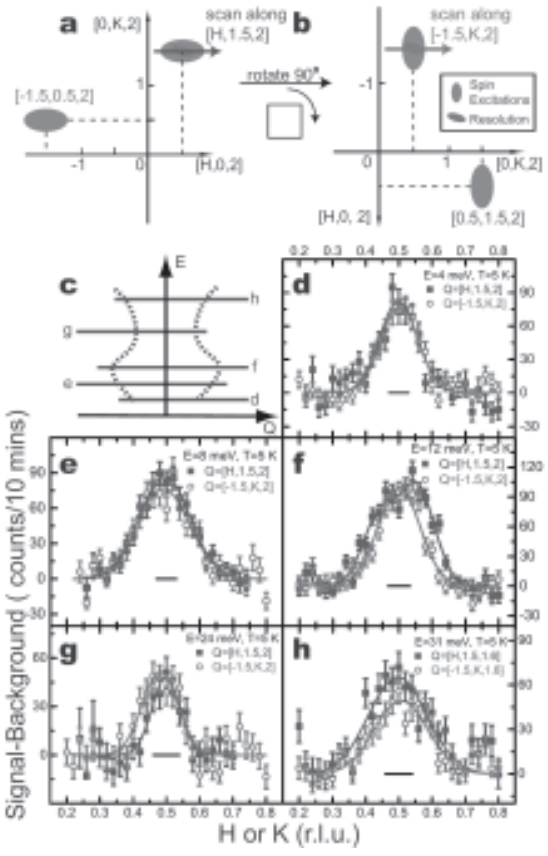


**Fig. 2** *(a)-(b) The measurements were carried out in the [H,K,*4*K*/3*] and [H,K,*4*H*/3*] zones by rotating the sample 90 degrees along c*. The advantage of such a setup is that the instrumental resolutions are identical in a* and b* scan directions. (c) Schematic Q-scans at different energies. (d)-(h) Q-scans along the [H,*1.5,2*] and [*-1.5,K,2*] directions at different energies in the low-temperature superconducting state. At 12 meV, the data show clear flattish top and we fit the data with two Gaussian peaks with the incommensurability of* $\delta$ = 0.057 ± 0.003 rlu*. The Q-profiles become narrow and isotropic again near the resonance energy. The instrumental resolutions are shown as the horizontal bars.*

Figures 2d-h summarize the constant-energy scans along *H* and *K* directions for energy transfers of $\hbar\omega$ = 4, 8, 12, 24, and 31 meV in the low temperature superconducting state. At $\hbar\omega$ = 4 meV, *Q*-scans along the *H* and *K* directions show identical behavior and suggest that spin fluctuations are isotropic at this energy (Figure 2d). On increasing the

energy to $\hbar\omega$ = 8 meV, the excitations become broader in $\boldsymbol{Q}$ but are still the same along $H$ and $K$ directions (Figure 2e). Upon increasing the energy further to $\hbar\omega$ = 12 meV, the $Q$-scan along the $H$ direction shows a clear flattish top indicative of incommensurate spin excitations while the identical scan along the $K$ direction is commensurate and has a smaller width than the $Q$-scan along the $a^*$ direction. At energies near and above the resonance (at $\hbar\omega$ = 24, and 31 meV, respectively), the scattering profiles become narrow again and the in-plane magnetic anisotropy essentially disappears (Figures 2g,h). Figure 2c summarizes the dispersions of the spin excitations along $a^*$-direction. The disappearing spin gap energy in the sample did not reveal more incommensurate scattering as expected from a naïve stripe picture but instead showed that the low-energy spin excitations are commensurate much different from the dispersion of the lower-doping LSCO [3].

### References


[1] Shiliang Li, Zahra Yamani, Hye Jung Kang, Kouji Segawa, Yoichi Ando, Xin Yao, F. Ye, H.A. Mook, Pengcheng Dai, Phys. Rev. B 77 (2008) 014523.

[2] P. Dai et al., Phys. Rev. B 63 (2001) 054525; H. F. Fong et al., Phys. Rev. B 61 (2000) 14773; C. Stock et al., Phys. Rev. B 69 (2004) 014502.

[3] J. M. Tranquada, Neutron scattering studies of antiferromagnetic correlations in cuprates, in Handbook of High-Temperature Superconductivity, edited by J. R. Schrieffer and J. S. Brooks (Springer, New York, 2007), pp. 257-298.

# Neutron Scattering Study of YBCO6.31: Nature of the Phase Just Below the Superconducting Phase

**Z. Yamani [1], W.J.L. Buyers [1], R. Liang [2], D. Bonn [2], and W. N. Hardy [2]**

[1] Canadian Neutron Beam Centre, National Research Council, Chalk River Laboratories, Chalk River, ON, Canada K0J 1J0

[2] Physics Department, University of British Columbia, Vancouver, BC, Canada V6T 1W5

The interplay between magnetism and superconductivity (SC) and how one phase is transformed to the other by doping, p, continues to be one of the most prominent questions in the physics of high-temperature superconductivity (HTSC). For the $YBa_2Cu_3O_{6+x}$ (YBCO6+x) family of superconductors, no studies have been made of whether the antiferromagnetic (AF) Néel phase is contiguous to the superconducting phase or whether a different phase such as the spin-glass phase of LaSrCuO separates them. A boson feature for $p < p_c$ (where $p_c$ is the critical doping) seen in thermal conductivity, has been taken as evidence that the AF and SC phases are contiguous (see [1] and references therein). Only a neutron measurement can directly prove the existence of a long-ranged Néel state.

Previous neutron scattering experiments (polarized and unpolarized with thermal and cold neutrons) on YBCO6.353 and YBCO6.334 crystals (with $T_c$ = 18 K and 8.4 K, respectively) have indicated [2-4] that superconductivity co-exists with quasielastic short-range AF correlations (central mode), but not with long-range antiferromagnetic order. In addition to the central mode, a damped excitation is also observed. The quasielastic spins are slowly dynamic, and are confined in finite-sized planar regions coupled weakly between planes. The spatial spin correlation length grows as doping is reduced but has not diverged even for the $T_c$ = 8.4 K sample of YBCO6.334 (i.e. no 3D magnetic Bragg peaks were observed). In addition, only a continuous increase of central mode intensity is observed [2-4] on cooling to the lowest temperature, another indication that there is no transition but rather a cross-over to the low temperature limit without crossing a phase boundary. Thus studies on superconducting samples so far have shown that the long-range AF and SC phases do not coexist. Whether long-ranged AF and SC phases are separated by a novel phase remains unanswered. To resolve this question, we used thermal neutrons to measure elastic neutron scattering properties of a new crystal of YBCO6+x doped with x = 0.31. This gives a hole doping in the copper oxide planes of only 0.045 which is just below the critical doping, $p_c$ = 0.052, for superconducting order.

The sample of YBCO6.31 consists of two co-aligned high quality single crystals grown at UBC with a total volume of ~ 2 cc that do not display a finite $T_c$. Nevertheless they remain in the orthorhombic phase, so that short oxygen chains are still available as a sink for holes. Neutron scattering measurements were performed at the C5 triple-axis spectrometer. A pyrolytic graphite (PG) vertically-focusing monochromator and a large flat analyzer were used at a fixed final neutron energy of $E_f$ = 3.52 THz. Two PG filters were used in the scattered beam to suppress higher order contamination. The horizontal collimations were set to [none, 0.48°, 0.55°, 1.2°].

The neutron scattering from YBCO6.31 shows no evidence for 3D Bragg resolution limited AF peaks. Instead we find that AF correlations behave similarly to those in more highly doped samples but now with even larger correlation lengths (see Figure 1). Along the *c*-direction, which couples the planes the correlations are clearly of finite range (~ 70 Å) and thus exclude the existence of 3D Bragg peaks. Within the *ab*-plane the correlations are too long to be determined accurately with thermal neutrons. The absence of Bragg order is also confirmed by the temperature dependence of central mode, which shows only a smooth increase with decreasing temperature with no anomaly that might signal a transition below a sharp Néel temperature. The lack of 3D Bragg AF peaks as well as lack of evidence for a transition suggests that, similarly to very underdoped but superconducting samples, the spins are organized in a spin-glass phase. This is further supported by the fact that at very low temperatures a decrease in the peak intensity of the central mode is observed upon cooling below $T \sim 20$ K.

Compared to YBCO6.33 with $T_c$ = 8.5 K, we find that the AF correlations are longer in YBCO6.31 but still remain finite. In addition in YBCO6.31, correlations start to grow at temperatures larger than for YBCO6.33. This study shows that there is an intermediate phase between the long range AF ordered and superconducting phases. The observed behaviour is consistent with a spin-glass phase. The absence of long range AF spin order does not require the presence of Goldstone spin-waves and renders the boson interpretation of thermal conductivity unlikely. Samples with even lower doping than YBCO6.31 will be required to access the long range AF ordered region of the phase diagram.

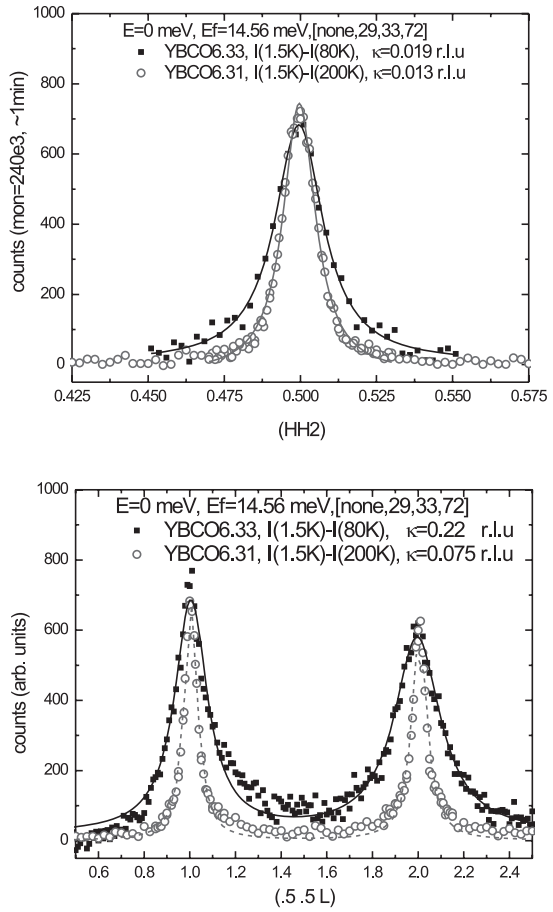


***Fig. 1*** *The background subtracted elastic data around the AF position (0.5 0.5 2) along [H H 2] and [0.5 0.5 L] directions in non-superconducting YBCO6.31 are compared to those in superconducting YBCO6.33 ($T_c$ = 8.5 K). The fits to a Lorentzian form 1/($x^2$ +$\kappa^2$/4) are shown. Although larger, correlations remain finite in YBCO6.31.*

## References


[1] N. Doiron-Leyraud and L. Taillefer, Phys. Rev. Letters 100, 029702 (2008), M. Sutherland et al, Phys. Rev. Lett. 94, 147004 (2005); Y. Ando et al., Phys. Rev. Letters 100, 029701 (2008); Phys. Rev. B 72, 100502 R (2005).

[2] Z. Yamani et al., Physica C, 460-462 (2007) 430-431.

[3] W.J.L. Buyers et al., Physica B 385–386, 11–15 (2006).

[4] C. Stock et al., Phys. Rev. B 73, 100504(R) (2006).

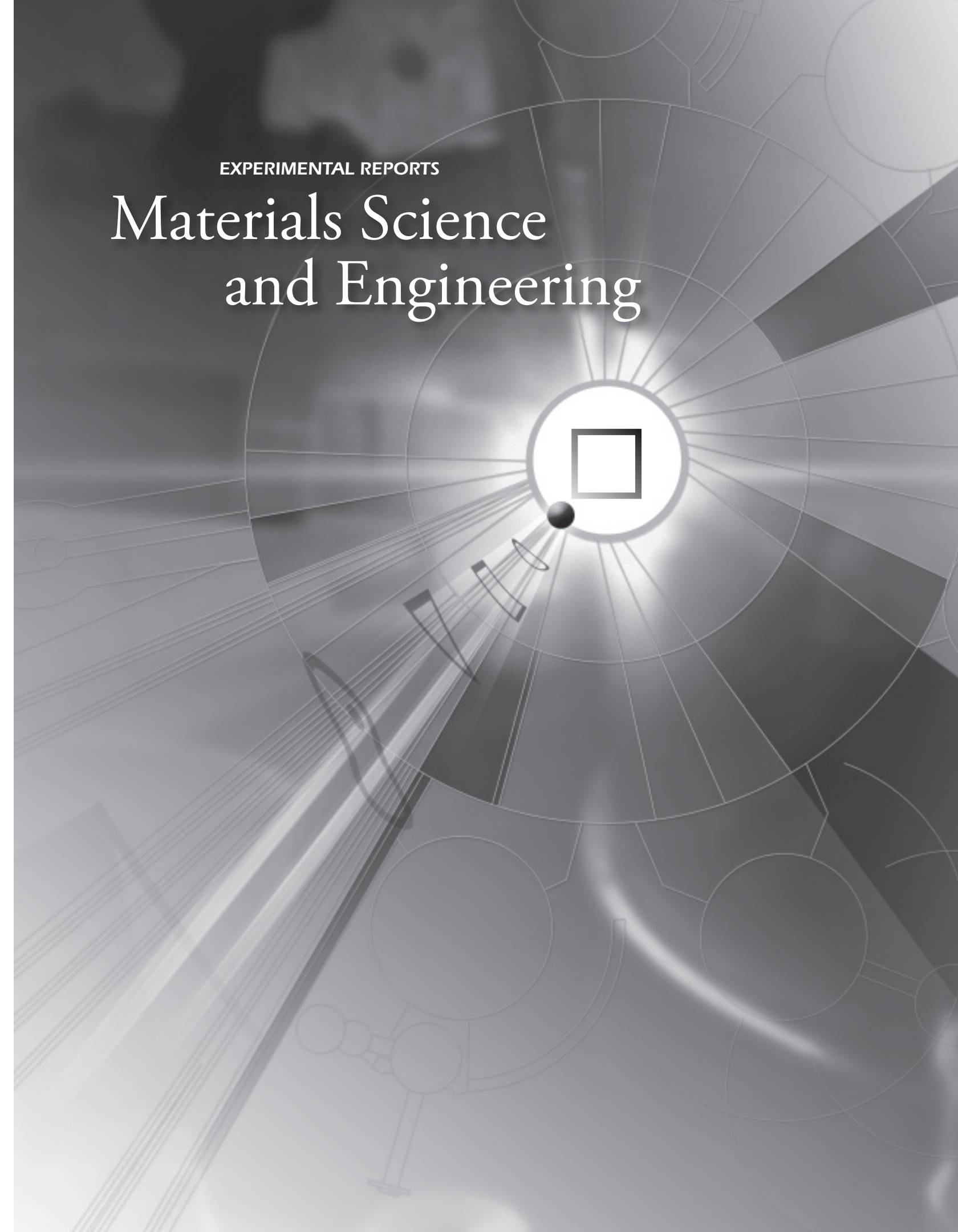

EXPERIMENTAL REPORTS

# Materials Science and Engineering

# *In-Situ Neutron Diffraction Study of Dual-Phase and Interstitial-Free Steels*

**H. Ma [1], and M.A. Gharghouri [2]**

[1] University of Toronto, Department of Materials Science and Engineering, Toronto, ON, Canada M5S 1A7

[2] Canadian Neutron Beam Centre, National Research Council, Chalk River Laboratories, Chalk River, ON, Canada K0J 1J0

Dual Phase (DP) steels consist of a ferrite matrix containing a hard martensitic second phase in the form of islands. They have become one of most popular and versatile materials in the automotive industry based on their excellent combination of high strength and good ductility. The increased strength to weight ratio afforded by these steels can potentially yield increased fuel efficiency.

DP steels have high yield stresses, require large forces during forming, and tend to be anisotropic in nature. As a result, their anisotropic nature leads to significant variations in springback and significantly complicates the design of tooling and the stamping process. It is thus essential to develop methods to accurately predict springback. Although many factors can affect springback, the Bauschinger effect should be taken into account in modeling to ensure that the internal stresses developed during sheet forming are properly captured. DP steels demonstrate a strong Bauschinger effect due to the inhomogeneous deformation of two phases.

TEM observations at pre-strains of 3% and 10% show that dislocation pile-ups occur around martensitic islands. At the large deformation, dislocation walls and cells appear, as shown in Figure 1.

It has been shown that DP steels demonstrate internal stresses due to the inhomogeneous deformation of the two phases. To identify the micro-mechanisms responsible for the strong Bauschinger effect in DP steels, and to evaluate models, a systematic investigation of the deformation response of each constituent phase in the material is needed. The distribution of stresses between the phases is hence a key element in this investigation. In-situ tensile tests with neutron diffraction provide a good way to measure internal and residual stresses to see how they respond to loads.

In figure 2, lattice strains as a function of applied stress are compared for DP and IF steels. The internal and residual stresses are stronger in the DP steels than in IF steels under the same deformation conditions, which suggest a stronger Bauschinger effect for DP steels. The results of the experiment have been used to understand, explain and model the Bauschinger Effect leading to the eventual simulation of springback behavior of DP sheet steels.

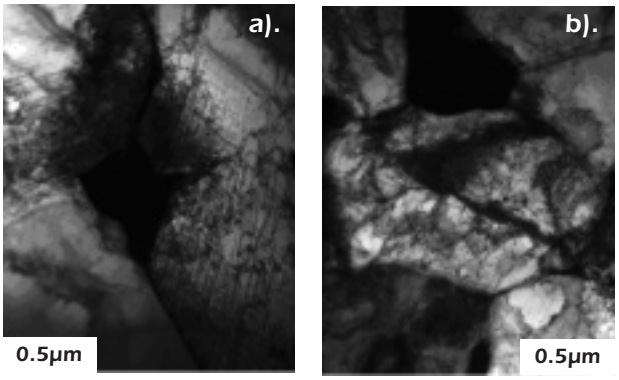


**Fig. 1** TEM at pre-strains of (a) 3% and (b) 10%.

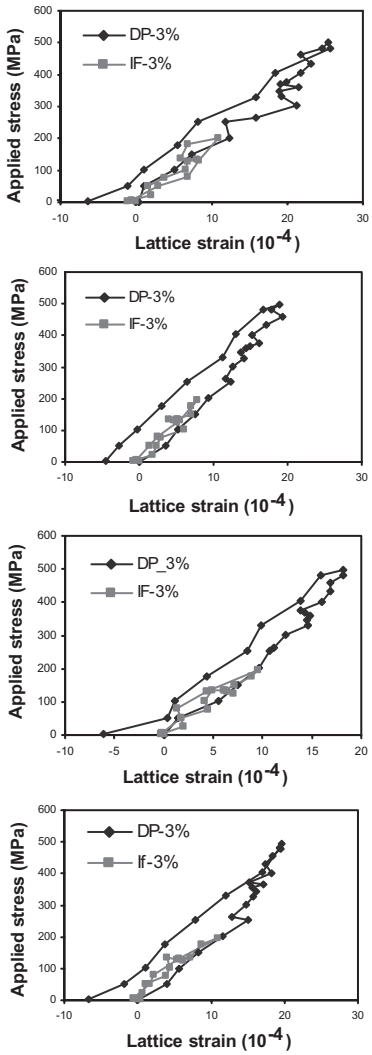


**Fig. 2** The lattice strain measurement at the load for pre-strain of 3% and unloaded.

# *In-Situ* Texture Evolution of $Ni_{49.2}Mn_{29.6}Ga_{21.1}$ with Annealing Temperature

**R. Hutanu** [1]

[1] Atomic Energy of Canada Limited, Chalk River Laboratories, Chalk River, ON, K0J 1J0

## Introduction

Ni-Mn-Ga magnetic shape memory alloys are smart materials that can exhibit large recoverable strains (several %) when subjected to a magnetic field. The strains obtained from these materials are much larger than those from magnetostrictive materials (~ 0.2%) and are comparable to those obtained from conventional shape memory alloys. The strain recovery takes place upon removal of the magnetic field, a process that is faster compares with the shape recovery process in conventional shape memory alloys. Applications of Ni-Mn-Ga based include actuators, positioning devices, sonar devices and robotics.

Conventional shape memory alloys undergo a reversible martensitic transformation when cooled below a critical temperature (the martensite start temperature, $M_s$), in which a cubic parent phase (austenite) transforms into a tetragonal, orthorhombic or monoclinic martensitic phase. The type of the martensitic structure depends on the chemical composition of the sample. Re-transformation to austenite occurs upon heating and in the case of Ni-Mn-Ga, the austenite phase has a Heusler structure (Figure 1).

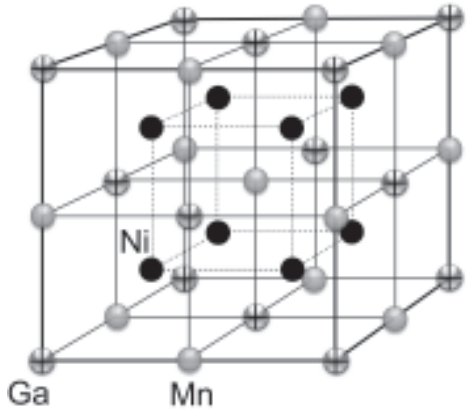


**Fig. 1** Austenite (parent phase) of Ni-Mn-Ga.

$Ni_2MnGa$ off-stoichiometric compounds show the largest magnetic shape memory effect. Although Ni-Mn-Ga single crystals have been extensively investigated, there is less work on the behaviour of polycrystalline Ni-Mn-Ga. This report is focused on the investigation of the texture evolution of polycrystalline Ni-Mn-Ga with annealing temperature.

## Sample and experimental set-up

The nominal composition of the polycrystalline sample used in the present work was $Ni_{49.2}Mn_{29.6}Ga_{21.1}$. This composition was chosen such that the material is martensitic at room temperature, which is desired for practical applications. The sample's geometry was cylindrical with its length and diameter equal to 1cm.

The neutron diffraction texture measurements were performed at E3 spectrometer at the Canadian Neutron Beam Centre (CNBC) at Chalk River Laboratories. In order to study the evolution of the texture with temperature, a specialized "bulb" furnace was installed on a Eulerian cradle at the spectrometer (Figure 2). The sample was gradually annealed using a Ta heater from the room temperature martensite to austenite and full pole figure data were collected for the major diffraction peaks of the two phases. The sample was in a vacuum of approximately $5\times10^{-2}$ Torr for the duration of experiments.

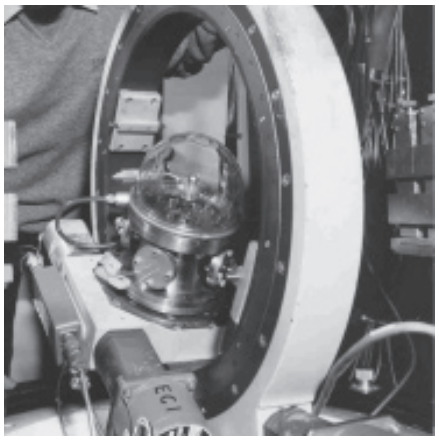

**Fig. 2.** Photograph of the "bulb" furnace placed on the Eulerian Cradle at the E3 spectrometer at CNBC.

## Neutron diffraction pole figures data

Analysis of additional neutron data obtained at the C2 powder diffractometer indicated that the martensite structure is complex and is in fact composed of at least 2 phases. At this writing, the analysis of pole figures from the room temperature martensite is not completed and thus only the austenite data will be discussed in this report.

Figure 3 shows the austenite pole figures for 65 and 85°C. Direction "R" of the pole figures was the reference direction for the measurements and was arbitrarily chosen as one of the diameters of the cylindrical sample.

Interestingly, Figure 3 shows that the austenite texture is changing with temperature, especially in the case of the <200> and <220> crystallographic directions. Further investigation involving an ODF analysis of the pole figures

is required in order to determine the details of this texture evolution.

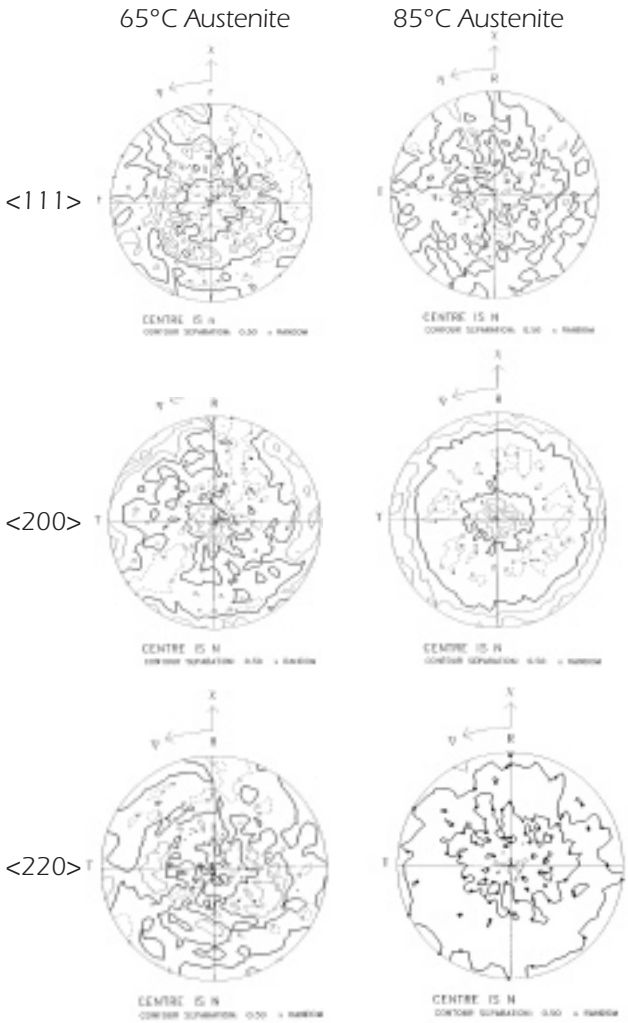


**Figure 3.** *Austenite <111>, <200> and <220> pole figures at 65 and 85°C.*


## Acknowledgements

The author wishes to thank Jimmy Bolduc for his support with the experimental set-up. The author is also thankful to Dr. Michael Gharghouri and Dr. Ron Rogge for their help and input provided for this experiment.

# Study of Texture Evolution during Channel-Die Compression of Mg-Al Alloys by In-Situ Neutron Diffraction

**D.G. Sediako, M.A. Gharghouri [1]**

[1] Canadian Neutron Beam Centre, National Research Council, Chalk River Laboratories, Chalk River, ON, Canada K0J 1J0

## Introduction

The chemistry of alloys and the casting-rolling production routes determine the cost and properties of magnesium sheets [1]. For example, the coarse-grained structure usually associated with DC casting requires complex rolling schedules to refine the grain size. Added complexity comes from micro- and macro-segregation of the alloying elements, as well as from localized, such as radial or edge, stress accumulation. These affect rolling productivity, and can also result in product defects, such as cracking, and inferior mechanical properties.

Rolling can result in a strong crystallographic texture, which is responsible for the tension-compression strength asymmetry exhibited by rolled magnesium alloys. The strength asymmetry is due mainly to the common {1012} twinning mechanism, which can accommodate tensile strain, but not compressive strain, parallel to the HCP c-axis. Thus, the stronger the basal texture, the stronger is the tension-compression asymmetry.

Alloy composition influences deformation behavior. The behavior of pure magnesium and of two binary Mg-Al alloys was investigated by neutron diffraction, as aluminum is one of the most common alloying elements in Mg alloys. The simple Mg-Al system was used in order to isolate the influence of aluminum on deformation behavior, which can be strongly influenced by other alloying additions.

## Experiment

A channel-die insert compatible with the CNBC high-temperature vacuum furnace was designed and fabricated to simulate industrial rolling operation. Two binary Mg-Al alloys (3 wt.% and 9 wt.% Al) were subjected to plane strain compression with continuous monitoring of texture and lattice strain. For each experiment, the specimen was mounted in the furnace and load frame, heated to the target temperature, and the temperature was allowed to stabilize for at least 30 minutes. A sequence of loading steps was then applied, with data collected at the end of each step, with the material in the unloaded condition. The pure Mg was deformed at 250°C, while the Mg-3%Al and Mg-9%Al alloys were deformed at 350°C.

## Metallography

As shown in Figure 1(a)-(d), the Mg-3%Al alloy has a grain size of 40-75 µm, while the Mg-9%Al alloy has finer grains in the 20-40 µm range. Another clear difference between the starting structures of the alloys is the presence of twinning in the Mg-3%Al alloy; the Mg-9%Al metal is free of twinning.

The Mg-3%Al alloy underwent a slightly higher degree of deformation (1.75:1 reduction ratio) than the Mg-9%Al alloy (reduction ratio 1.5:1). This deformation resulted in grain refinement of 65% for the Mg-3%Al alloy (from an average size of 57 µm down to 20 µm), Figure 1(b). In the case of the Mg-9%Al alloy, the grain refinement was just ~ 20%, from an average of ~ 30 µm to 25 µm, Figure 1(d).

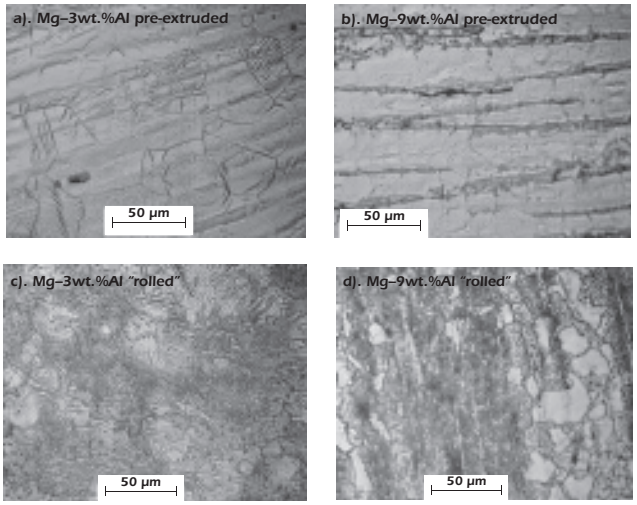


**Fig. 1** *Microstructural evolution of Mg-Al binary alloys: (a, c) starting (pre-extruded) structure, and (b, d) resulting "rolled" structure.*

The Mg-3%Al alloy twinned extensively during deformation, which should have an effect on the crystallographic texture of the material. The 9%Al alloy does not exhibit any twinning, which can be attributed to greater mechanical strength of this material.

Little or no $Mg_{17}Al_{12}$ precipitates were present prior to testing for both alloys. The resulting structures, however, show numerous β-phase precipitates, which can have an influence on texture development.

## Results: Texture Evolution

In magnesium and its alloys, extrusion results in the basal poles aligning themselves normal to the extrusion axis, as shown in the (0002) pole figure for pure Mg before deformation (Figure 2a). Two different pure Mg specimens were compressed parallel and normal to the extrusion axis. The reduction ratio used was 4.8:1. The (0002) pole figure for the specimen compressed parallel to the extrusion axis is shown in Figure 2(b). The constraint from the channel die was parallel to Y, while free expansion was allowed parallel to X. The resulting (0002) pole figures for the specimens compressed normal and parallel to the extrusion axis

were identical. Comparing the (0002) pole figures for the deformed and undeformed states, it is clear that the (0002) poles have rotated, such that they have become aligned with the compression/extrusion direction. The pole figure is symmetric with respect to the loading axis.

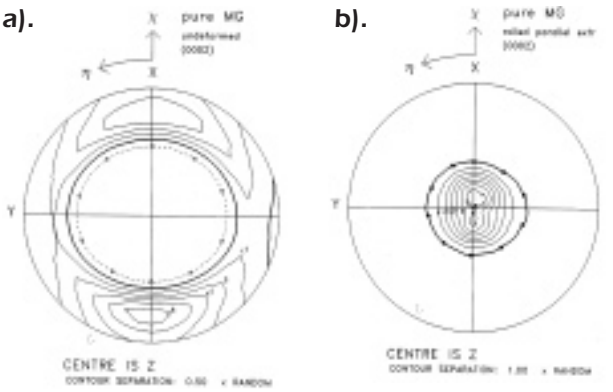


**Fig. 2** *(0002) pole figures for Mg (a) before and (b) after deformation. The heavy solid line in the pole figure corresponds to 1xRandom; the solid lines are at the noted contour intervals up to the maximum contour marked with x's. The dashed lines are for contours below random and the minimum contour is marked with circles. The extrusion axis is parallel to the Z-axis in the pole figure.*

The (0002) pole figures for Mg-3%Al before and after deformation are shown in Figure 3. The specimen was compressed parallel to the extrusion axis (Z). The constraint from the channel die was parallel to Y, while free expansion was allowed parallel to X. As in the case of the pure Mg, the (0002) poles have aligned themselves with the direction of the compression and extrusion. However, unlike in the pure Mg, the texture has become asymmetric with respect to the compression axis.

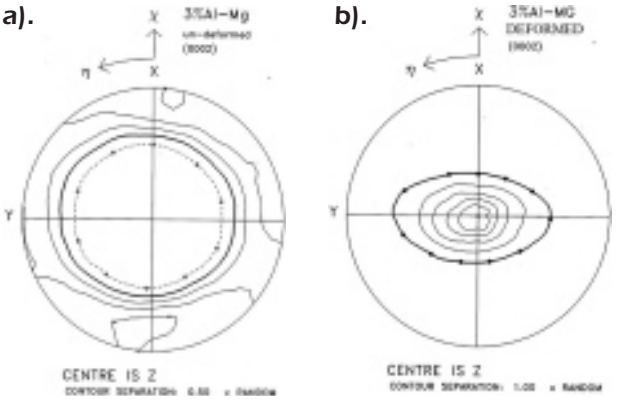


**Fig. 3** *(0002) pole figure for binary Mg-3% alloy (a) before and (b) after deformation.*

The (0002) pole figures for Mg-9%Al before and after deformation are shown in Figure 4. The specimen was compressed normal to the extrusion axis (Z). The extrusion axis was parallel to X, and the material was allowed to expand freely in that direction. The channel-die walls constrained expansion parallel to Y. As shown in the figures, very little texture evolution has occurred.

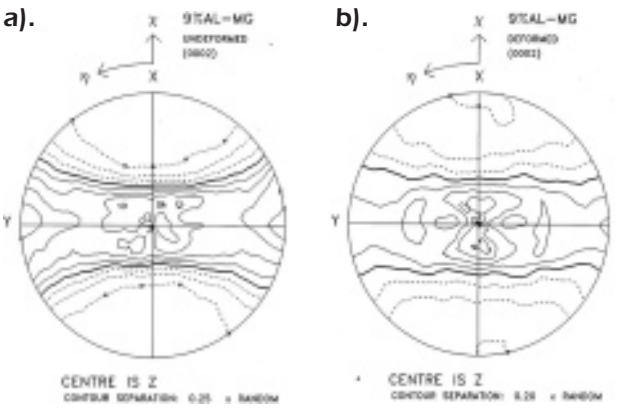


**Fig. 4** *(0002) pole figure for Mg-9wt.% Al (a) before and (b) after deformation.*

## Discussion: Deformation Mechanisms

The texture evolution exhibited by the three materials can be attributed to basal slip and {1012} twinning, both of which are consistent with the observed changes in texture. Basal slip results in the basal poles aligning themselves with the compression/extrusion direction. Reorientation due to slip occurs gradually over a large strain interval, and is generally favored at higher temperatures and low strain rates. {1012} twinning results in an 86.4° reorientation of the crystal lattice, which would result in grains having an orientation represented by points at the periphery of the pole figures moving to the centre of the pole figures. Lattice reorientation due to twinning occurs abruptly, at the speed of sound, and is favored at lower temperatures and higher strain rates.

The pole figures for the materials before deformation show a weak extrusion texture, with a maximum intensity of 2-3.5×random. The maximum intensity after deformation is about 8×random for the pure Mg, about 6×random for Mg-3%Al, and only about 1.6×random for Mg-9%Al. The differences in the deformation textures exhibited by the three materials are due to differences in the relative amounts of basal slip and {1012} twinning, which are influenced by strain, temperature and composition (as it pertains to solid solution and precipitation strengthening).

The pure magnesium was deformed at a lower temperature, and to a much higher strain, than the two binary alloys. It exhibits the strongest deformation texture, which is symmetric about the compression axis, despite the constraints imposed by the channel walls. Pure magnesium deforms easily by basal slip and {1012} twinning at elevated temperatures. [2] Typically, lenticular twins form within a grain, and grow until the original grain is entirely consumed. For the specimen compressed parallel to the extrusion axis, most of the grains are favourably oriented for {1012} twinning; the material can thus be expected to twin completely, resulting in the observed lattice reorientation. Once twinning has occurred, basal slip can take place on the reoriented basal planes. The specimen that was compressed normal to the extrusion axis (pole figure identi-

cal to Figure 4) presents an interesting case. The resulting deformation texture suggests that significant {1012} twinning has occurred likely due to the constraints imposed by the channel walls, which impose a compressive load normal to the c-axis in many grains.

The Mg-3%Al exhibits a similar deformation texture to the pure Mg, though it is weaker, due to the much lower strain imposed, and it is not symmetric about the compression axis. It is likely that {1012} twinning is the dominant mechanism contributing to texture evolution. However, it appears that the constraints imposed by the channel walls, perhaps combined with the precipitation that takes place, restrict twinning in some grain orientations, resulting in the asymmetric texture

The Mg-9%Al exhibits relatively little change in texture. This can only be explained by basal slip since no twinning was observed in the metallographic structure of the sample. The presence of copious precipitation appears to inhibit twinning.

### References


[1] F.W. Bach, M. Rodman, A. Rossberg, and M. Hepke. Magnesium Sheet Production Today And Tomorrow. Proceedings of the International Symposium on Magnesium Technology in the Global Age, Montreal, QB, 2006. 255- 268.

[2] S.E. Ion, F.J. Humphreys, S.H.White. Dynamic Recrystallization and the Development of Microstructure during the High Temperature Deformation of Magnesium. Acta Metall. 1982. 30: 1909-1919

# Quantitative Analysis of Hot-Tearing Susceptibility of New High-Temp Magnesium Alloys Using Neutron Diffraction

**L. Bichler [1], C. Ravindran [1], and D.G. Sediako [2]**

[1] Department of Mechanical and Industrial Engineering, Ryerson University, Toronto, ON, Canada M5B 2K3

[2] Canadian Neutron Beam Centre, National Research Council, Chalk River Laboratories, Chalk River, ON, Canada K0J 1J0

## Introduction

The automotive industry has renewed interest in magnesium alloys. Magnesium alloys are about 35% lighter than aluminium and about 80% lighter than steel. As a result, incorporation of magnesium alloy castings in new vehicles plays a critical role in reducing the vehicle's weight and increasing its fuel efficiency. Further, magnesium alloys show excellent specific properties, castability and recycling potential. However, when magnesium alloys are processed via high-pressure die-casting (HPDC) or permanent mold casting (PMC), they show high susceptibility to hot tearing.

Thermal and mechanical stress, strain and feeding, that is, interdendritic liquid flow of a given alloy are known to be the key parameters affecting the onset of hot tearing. Theoretical criterion functions based on these concepts were developed with the aim of predicting the onset of hot tearing. However, experimental validation of these criterion functions remains a challenge, because the currently available test methods often involve intrusive probes, which alter the casting solidification profile, or indirect estimations of the stress or strain conditions.

Solidification stresses arise in a casting due to thermal gradients causing inhomogeneous casting contraction during solidification. Further, when a casting solidifies within a rigid steel mold, as in the case of HPDC or PMC processes, the casting contraction is opposed by the rigid mold and consequently mechanical stresses develop in the semi-solid alloy. Measurement of casting residual stresses at the onset of hot tearing using neutron diffraction (ND) has not yet been reported in literature.

In this research, two magnesium alloys were studied: (1) AZ91D (9 wt%Al – 1 wt%Zn) magnesium alloy; AZ91D has excellent castability and room temperature mechanical properties, and is currently used in the automotive industry; (2) AE42 (4 wt%Al – 2 wt%RareEarths) magnesium alloy; AE42 is known for its excellent high-temperature strength in comparison to traditional magnesium alloys, such as AZ91 or AM60, and thus has a high potential for future use, for example in engine components.

Both of these alloys are susceptible to hot tearing. In order to control the severity of hot tearing in the current experiments, the mold temperature was increased from 140°C to 390°C. Figure 1a shows the casting geometry and the region where hot tears typically nucleated. Figure 1b,c illustrate the effect of mold temperature on hot tearing in the critical region. Residual strain for (100), (002), (101) and (102) crystallographic reflections was measured on two castings for each alloy: one with a hot tear, one without a hot tear. The edge of the casting, where hot tears were typically observed, corresponded to location of *x=0*.

In summary, this research involved measurement of the total, that is, thermal and mechanical, residual strains in castings with various degrees of hot tearing. Also, the solidification history and microstructure of the castings was analyzed, thus correlating these fundamental parameters to the onset of hot tearing.

## Results

Analysis of the residual strain profiles along the length of the horizontal bar (i.e., strain variation in *x*-direction) revealed that the reflections (100) and (002) did not show significant strain development for $\varepsilon_x$, $\varepsilon_y$ and $\varepsilon_z$. However, reflections (101) and (102) exhibited a definite $\varepsilon_x$ strain variation along the length of the bar: higher tensile strain in the sprue region, followed by a decreased strain in the horizontal bar.

### AZ91D

The *x*-direction contraction of the horizontal bar induced tensile strain in the horizontal bar and was responsible for initiation of hot tears in the casting. Casting contractions in the *y*- and *z*-directions were not restricted and thus resulted in compressive residual strains. Figure 2 shows the distribution of $\varepsilon_x$ strains along the length of the horizontal bar for the (101) reflection in the cracked and non-cracked castings, respectively.

In the case of a casting with a hot tear, the $\varepsilon_x$ strain in the sprue region ($x < 0$ mm) was tensile: 0.00051 mm/mm. Residual strains were relieved in the area of the crack, as indicated by a drop in the strain profile in Figure 3a. The $\varepsilon_x$ in the horizontal bar to right of the 90° junction was tensile 0.00018 mm/mm ($15 < x < 25$ mm). In the case of a casting without a hot tear, Figure 3b, the $\varepsilon_x$ strain in the downsprue was also tensile: 0.00044 mm/mm. However, contrary to the cracked casting, the region to the right of the 90° junction ($15 < x < 25$ mm) possessed compressive $\varepsilon_x$ strain of 0.00011 mm/mm. The strains in the casting became tensile only far away from the 90° junction.

The difference in the $\varepsilon_x$ strain profile was related to the feeding of the casting. At high mold temperatures, intergranular liquid feeding was possible for a longer period of

time. Thus, the volumetric contraction of the horizontal bar was compensated by incoming liquid metal feed, and the developing strains were continuously alleviated. However, for low mold temperatures, the horizontal bar solidified and contracted rapidly without compensation by liquid metal from the downsprue. Thus, inadequate compensation of casting contraction resulted in the development of significant tensile strains, which aided in separation of dendrites and crack nucleation.

### AE42

The relative uniformity of the measured strain values suggests that the horizontal bar solidified rapidly along its entire length, unlike in the case of the AZ91D alloy, where the casting solidified slowly from the restraint towards the sprue. The measurements indicate that the HCP crystals in the AE42 alloy experienced a significant strain, as shown in Figure 3.

Prior to reaching the onset conditions, a casting without a hot tear developed tensile strains between 0.006 – 0.007 mm/mm. Upon nucleation of a hot tear, the tensile strains were relieved and reduced to nearly zero. The basal planes (002) retained some of the tensile strains, even after hot tearing occurred. This observation suggests that the basal planes in the AE42 alloy were stiffer than the prismatic or pyramidal planes. A possible reason for this observation is the formation of Mg-Al$_x$RE$_y$ precipitates on the basal planes and their ability to resist dislocation motion during high temperature deformation. For the directions (101) and (102), a marginal reversal of the strain condition (from tensile to compressive) was recorded with the onset of hot tearing, as shown in Figure 3. This is in agreement with reported studies on high-temperature deformation of magnesium and its alloys, which have shown that the critical resolved shear stress (CRSS) at room temperature is considerably higher for non-basal slip than for the dominant basal slip. However, Agnew *et al.* [1] suggested that the relative strength and hardening response of a variety of slip and twinning systems control the deformation of magnesium alloys at elevated temperatures. At elevated temperatures, reorientation of the basal planes occurs, thus activating additional non-basal slip systems and accelerating bulk deformation. In particular, deformation along the (101) and (102) crystallographic directions was seen to dominate.

### Conclusions

Neutron diffraction analysis in conjunction with thermal analysis and microscopic characterization enabled a better understanding of casting behaviour at the onset of hot tearing. The measurement of casting residual strain at the onset of hot tearing was successfully carried out and yielded information previously unavailable.

At high solidification rates (~ 15 °C/s), the AZ91D castings developed hot tears, since the downsprue was not able to sufficiently feed the horizontal bar. As a result, the horizontal bar's contraction was not compensated by incoming liquid metal feed, tensile $\varepsilon_x$ strain of 0.00018 mm/mm developed in the horizontal bar, to the right of the 90° junction. For an AZ91D casting without a hot tear the solidification rate was low enough (~ 10 °C/s) to enable liquid metal feed to the contracting horizontal bar. As a result, the $\varepsilon_x$ strain at the 90° junction remained compressive (0.00011 mm/mm) and hot tearing did not occur.

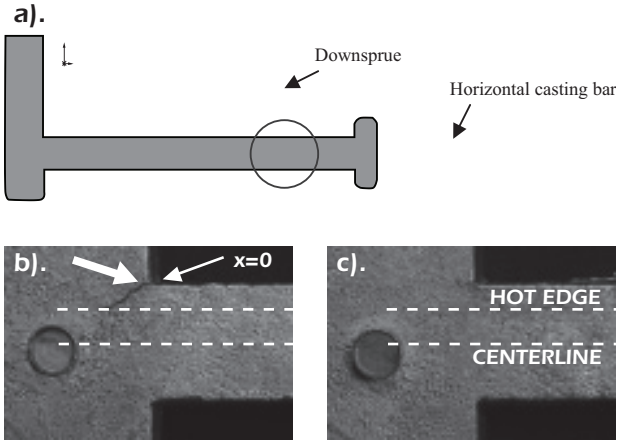


**Fig. 1** *AE42 magnesium alloy castings: (a) casting geometry and "critical region" where hot tears formed, (b) casting with a hot tear (340 °C mold temperature), and (c) casting free of hot tears (390 °C mold temperature). The white dashed lines show the location of two of the four line scans performed to map the map the residual strain.*

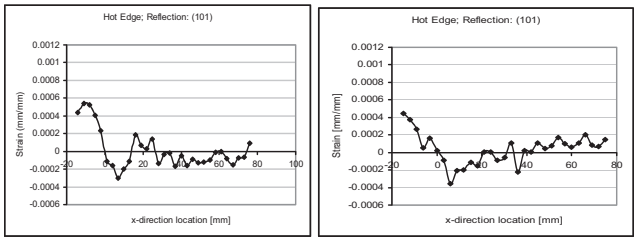


**Fig. 2** $\varepsilon_x$ *residual strain hot-edge profiles for AZ91D castings with (a) and without (b) a hot tear.*

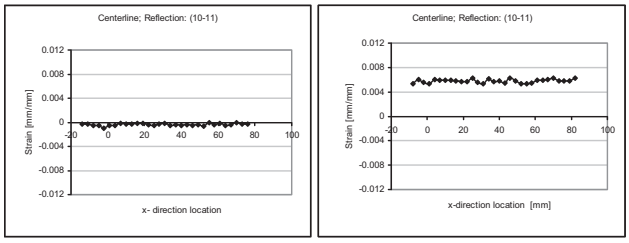


**Fig. 3** $\varepsilon_x$ *residual strain centerline profiles for AE42 castings with (a) and without (b) a hot tear.*

### References


[1] Agnew, S. R., Tome, C. N., Brown, D. W., Holden, T. M. and Vogel, S. C., Scripta Materialia. 2003. 48: 1003-1008

# Intergranular Residual Strain Behaviour of Mild Steel and Interstitial Free Steel as a Function of Low Temperature Annealing

**N. Kasai [1], R. Hutanu [2]***

[1] Graduate School of Environment and Information Sciences, Yokohama National University, 79-5 Tokiwadai, Hodogaya-ku, Yokohama, Japan 240-8501

[2] Canadian Neutron Beam Centre, National Research Council, Chalk River Laboratories, Chalk River, ON, Canada K0J 1J0

* Now with Atomic Energy of Canada Limited, Chalk River Laboratories, Chalk River, ON, Canada K0J 1J0

## Introduction

While the relationship between stress, residual stress and magnetism has been recognized for many years [1], it is not well understood due to the complexity of its many variables: differing types of stresses, and differing magnetic and mechanical properties of materials. Residual stress is often present in engineering components after a non-uniform plastic deformation. It can exist on various length scales: macroscopic residual stress appears on the sample's length scale while intergranular residual stress occurs within the grain size range. Grains in a polycrystalline sample deform differently depending on their crystallographic orientation relative to the applied stress direction. Upon unloading, some grains will have larger intergranular residual strain then others.

We used neutron diffraction to measure directly the residual strains for the <200>, <211> and <220> crystallographic directions in steels, and the Magnetic Barkhausen Noise (MBN) technique to characterize the magnetic behavior that these residual strains induced (MBN results are not reported here). Large tensile intergranular residual strains accumulated along the magnetic easy axis for steels, that is, the <100> crystallographic directions. Importantly, for body centred steels, <211> is usually chosen as the direction for macroscopic strain or residual measurement since it is known to accumulate only small intergranular strains [3]. In addition, uniaxial deformation should produce only few residual macrostresses since samples are typically designed to deform uniformly.

While a definite correlation between the <200> intergranular residual strain and the magnetic easy axis development in steel samples was shown previously [2], a systematic study of the low temperature (at and below 500°C) annealing effect on intergranular stresses and magnetic behaviour is needed to clarify the intergranular stresses relief phenomenon and its influence on magnetic properties.

## Samples

Several mild and interstitial-free (IF) steel samples were used in this study. The mild steel samples display discontinuous yield behaviour upon deformation due to the Luders bands formation. In contrast, IF steel, which contains very low levels of carbon and other interstitial elements, deformed continuously through the yield point with no Luders effect.

The mild and IF steel samples were cut from commercially available sheets of 3 mm and 1.7 mm thickness respectively. The cut samples had a 'dog-bone' shape and the gauge lengths of 155 mm x 30 mm. The width of the samples was chosen to accommodate the MBN probe. The axial direction of the samples coincided with the rolling direction (RD) of the sheet. The other two directions of the sample were the transverse direction (TD), perpendicular to the RD and in the sample's plane, and the normal direction (ND), which was normal to the sample surface.

Samples were then uniaxially deformed in tension at a strain rate of 0.1 in/min up to 20% engineering strain level using an 800 kN-capacity Riehle testing machine, followed by unloading. The loading direction corresponded to the original rolling direction (RD) of the sheet. Individual samples deformed at 20% strain were then annealed. The annealing temperatures were between 100°C to 500°C and annealing times between 0.5 and 10 hours. All heat treatments were performed in air using a radiant box furnace. Samples were then cooled slowly in air to room temperature.

## Neutron Diffraction Experiments

The samples were wire-cut to 1×1 $cm^2$ using an electric discharge machine (EDM), and then stacked together forming an approximate cube with dimensions of 1 cm. The entire cube was immersed in the neutron beam using an Eulerian cradle mounted on the E3 spectrometer. The strain for the <200>, <110> and <211> crystallographic directions was measured on 0% (un-deformed), 20% (before annealing) and on after-annealing samples. Strain data were obtained in an angular fashion every 15° (or 30°) between the ND-RD, RD-TD and TD-ND planes (Figure 1).

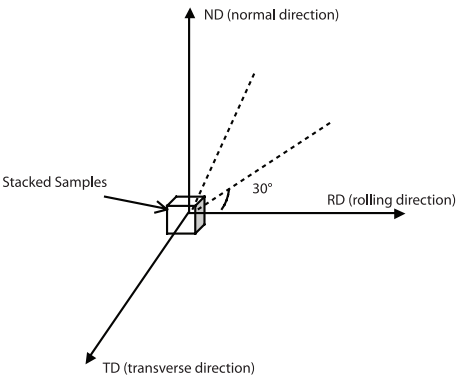


**Fig. 1** Residual strain measurements were performed along nine different directions within the RD-TD, TD-ND and ND-RD planes.

Crystallographic texture data was also obtained in the form of pole figures for the <200>, <110> and <211> directions, before and after annealing. The experimental set-up and the wavelength were identical to those for the strain measurements.

## Results

The <211> residual strain, which characterize the macroscopic residual strain, were found to be negligible for both steels and for all the measurement directions, and thus are of intergranular origin. Since the <200> residual strains are responsible for the magnetic behaviour in steels, only these strains will be discussed in this report.

As expected annealing at 500°C induces the strongest relief of intergranular residual strain for mild steel (Figure 2a). This effect can be observed especially within the TD-ND plane where the intergranular strain is the largest. Annealing data below 300C showed no significant effects on residual strain and MBN for both steels. The annealing effects at 300 and 500°C for the IF steel samples (Figure 3a) are smaller than for mild steel (Figure 2a), perhaps due to the fact that the IF steel <200> strains are in general smaller than <200> mild steel strains.

**a).**

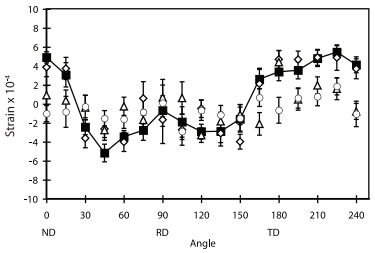


**b).**

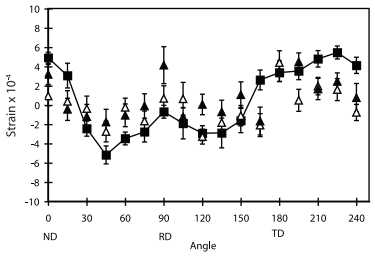


**Fig. 2** *Annealing effects on <200> intergranular residual strain for mild steel. Figure 2a shows this effect for constant annealing time of 0.5 hrs for 300 (◇), 400(△) and 500 °C (○). Figure 2b shows the effect of the annealing time, 0.5 hrs (△) and 10hrs (▲), for samples annealed at 400°C. The solid lines connecting the ■ symbols in both plots represent the prior annealing, after deformation (20% strain) data.*

In general, the effect of the annealing time (0.5 and 10hrs) is not significant in the case of both mild and IF steel samples annealed at 400°C (Figures 2b and 3b). A similar result was obtained for the 500°C annealings.

Overall, the residual strain data obtained by neutron diffraction agree with the MBN annealing results not reported here.

A comparison between the pole plots (Figures 4 and 5)

**a).**

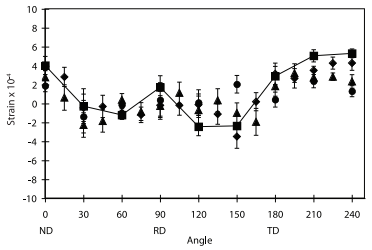


**b).**

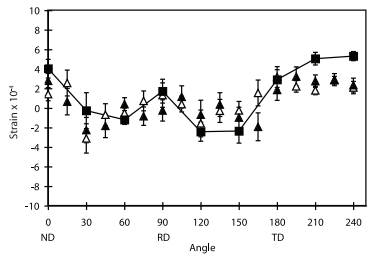


**Fig. 3** *Annealing effects on <200> intergranular residual strain for IF steel. Figure 3a shows this effect for constant annealing time of 10 hrs for 300 (◆) and 500 °C (●). Figure 3b shows the effect of the annealing time, 0.5 hrs (△) and 10hrs (▲), for samples annealed at 400°C. The solid lines connecting the ■ symbols in both plots represent the prior annealing, after deformation (20% strain) data.*

shows that the initial as well the after-deformation textures of the mild and IF steels are quite different, probably due to different manufacturing process of the two steels. However, in both cases, annealing at 500°C has only a minimal effect on texture, confirming that up to this temperature the heat treatment does not induce any recrystallization in the samples.

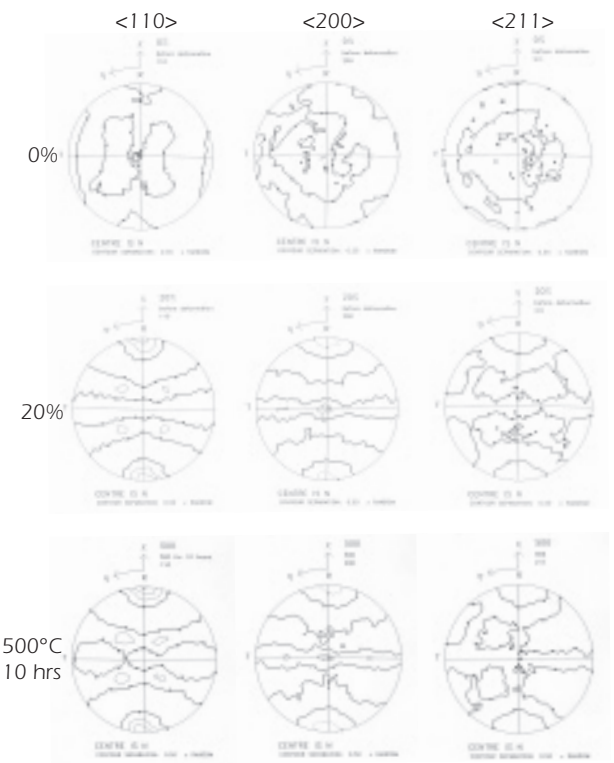


**Fig. 4** *<110>, <200> and <211> pole figures for the un-deformed (0%), deformed and prior- annealing (20%) and after-annealing (500°C, 10hrs) mild steel samples. R, T and N directions are the same as RD, TD and ND directions from Figure 1.*

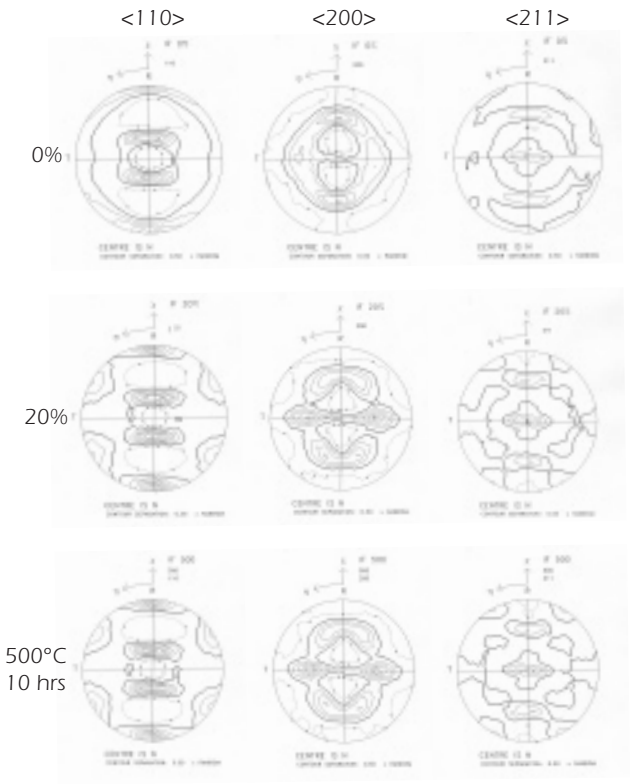


**Fig. 5** *<110>, <200> and <211> pole figures for the un-deformed (0%), deformed and prior-annealing (20%) and after-annealing (500°C, 10hrs) IF steel samples. R, T and N directions are the same as RD, TD and ND directions from Figure 1.*


## Acknowledgments

The authors wish to thank Dr. Ron Rogge and Dr. Lynann Clapham for their input with the experiments proposal and design. The authors are also thankful to John Fox for his help in setting up the experiment.


## References


[1] Bozorth R. M. Ferromagnetism. D. Van Nostrand Company, Princeton, New Jersey, 1951.

[2] Roxana Hutanu. A correlation study between Magnetic Barkhausen Noise and intergranular residual stress in steel. Ph.D. Thesis, Queen's University, Kingston, Canada, October 2005.

[3] Pang J.W.L, Holden T.M., Mason T.E. J. Strain Anal. 33:373 (1998).

# Effects of Overload and Underload on the Residual Stress, Crack Plasticity, and the Crack Growth Rate

**S.Y. Lee [1], H. Choo [1], P.K. Liaw [1], R.B. Rogge [2], and M.A. Gharghouri [2]**

[1] Department of Materials Science and Engineering, The University of Tennessee, Knoxville, TN USA 37996

[2] Canadian Neutron Beam Centre, National Research Council, Chalk River Laboratories, Chalk River, ON, Canada K0J 1J0

## Introduction

Many structural materials are subjected to variable-amplitude fatigue loading rather than constant-amplitude fatigue loading. Sudden changes in the cyclic loading patterns during fatigue deformation could give rise to complicated plastic zones in the vicinity of the crack tip and result in a considerable acceleration or retardation in the crack growth rate owing to these load interaction effects. Therefore, a fundamental understanding of the overload or underload effects and damage mechanisms will help enhance the lifetime prediction capabilities and improve the damage tolerance design for critical application exposed to random fatigue loadings. As a simple example, when a single tensile overload is applied during cycling loading, the crack growth rate slows down, which increases fatigue lifetime tremendously. Although much attention has been devoted to explain the retardation mechanism since its discovery in 1961, the phenomenon is still not fully understood. Due to the lack of experimental capabilities to measure the strain and stress fields within the bulk as a function of the distance from crack tip, the relationship between the overload or underload and the retardation or acceleration has not been quantitatively established.

## Methods

In order to study the effects of overloading, underloading, and their combination on the constant-amplitude fatigue-crack growth [i.e., $P_{max}$: 8,880 N, $P_{min}$: 89 N, a load ratio, R: 0.01, where $R = P_{min} / P_{max}$)], a single tensile overload (i.e., $P_{overload}$: 13,320 N, which is 150% of $P_{max}$), a single compressive underload (i.e., $P_{underload}$: -13,320 N) and a set of mixed loads (i.e., overload-underload and underload-overload) were imposed systematically when the crack length reached 16 mm. After applying various loading conditions, a constant-amplitude fatigue experiment was resumed.

The crack growth rate (*da/dN*) versus stress-intensity factor range ($\Delta K$) for the five different loading cases is shown in Figure 1. During a constant-amplitude fatigue-crack growth (*Case 1*), the crack growth rate increases linearly with increasing $\Delta K$. After a single tensile overload (*Case 2*), there was an instantaneous acceleration of the crack growth rate followed by a large retardation period, resulting in a temporary decrease in the crack growth rates. On the other hand, after a single compressive underload (*Case 3*), a brief acceleration of the crack growth rate was observed. However, subsequent crack growth rates were very comparable to those of *Case 1*. When a compressive underload was imposed immediately after a tensile overload, a retardation period was still found but had a significantly reduced extent (*Case 4*). Finally, when a tensile overload was imposed immediately after a compressive underload (*Case 5*), the crack-growth rates were similar to those of a single tensile overload (*Case 2*), indicating a large retardation period.

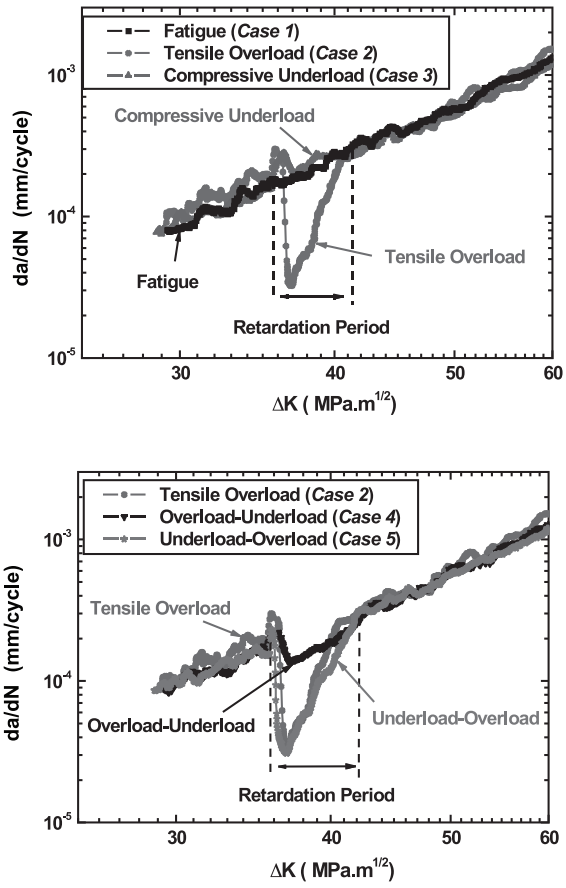


**Fig. 1** The changes in the crack growth rate (*da/dN*) as a function of stress-intensity-factor range ($\Delta K$) for the five different loading cases.

A neutron diffraction measurement was performed to probe the retardation or acceleration mechanism during fatigue crack growth following overload or underload using L3 spectrometer. High penetration capabilities and volume averaging of neutron diffraction technique allow mapping of the bulk residual strain and stress as a function of the distance from the crack tip. The five compact-tension (CT) specimens under different loading conditions [i.e., constant-amplitude fatigue (*Case 1*), tensile overloading (*Case 2*), compressive underloading (*Case 3*),

tensile overloading-compressive underloading (*Case 4*), and compressive underloading-tensile overloading (*Case 5*)] were prepared to study the influences of residual stresses on the crack growth rate (Figure 2).

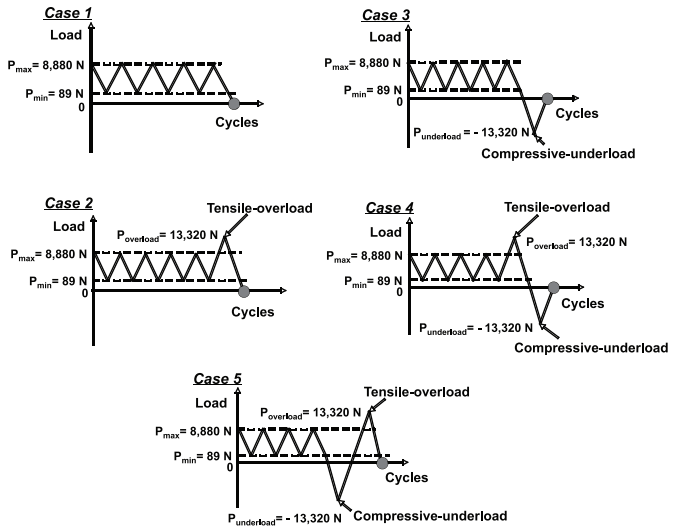


**Fig. 2** *Neutron strain mapping was performed at the marked point right after five different loadings were applied.*

The spatially-resolved neutron strain scanning was performed to measure three principal residual-strain components. A total of 26 points were measured as a function of the distance from the crack tip (Figure 3). To provide the required spatial resolution, we used scanning intervals of 1 mm from -4 to 0 mm (crack tip), 0.5 mm from 0 to 8 mm where sharp strain gradients are expected, 2 mm from 8 to 16 mm, and 3 mm from 16 to 22 mm. The wavelength in each direction was selected from the Ge115 monochromator.

For X-longitudinal and the Y-transverse strain components, the wavelength of 1.3 Å was selected, and the specimens were aligned 53° (clockwise) from the incident neutron beam and the (311) diffraction pattern was recorded in a stationary detector with diffraction angles 2θ = 74°.

Thus for the X-longitudinal strain component, the diffraction vectors were parallel to longitudinal direction, parallel to the crack growth direction (X), of the specimen. The incident beam was defined by 1 mm wide and 2 mm tall (parallel to Y) slits, and the diffracted beams were collimated by 1 mm wide slit.

For Y-transverse strain component, the diffraction vectors were parallel to transverse direction (parallel to Y) of the specimen. The incident beam was defined by 2 mm wide and 1 mm tall (parallel to X) slits, and the diffracted beams were collimated by 2 mm wide slit.

For Z-normal strain component, the wavelength of 1.74 Å was selected. The specimens were aligned 127° (clockwise) from the incident neutron beam and the (311) diffraction pattern was recorded in a stationary detector with diffraction angles 2θ = 106°. Therefore, the diffraction vectors were parallel to normal direction (parallel to Z) of the specimen. The incident beam was defined by 2 mm wide and 1 mm tall (parallel to X) slits, and the diffracted beams were collimated by 2 mm wide slit.

The interplanar spacing (*d*-spacing) was determined from the Gaussian fitting of the (311) diffraction peak and the lattice strain was obtained from

$$\varepsilon = (d-d_0)/d_0 \quad (1)$$

where $d_0$ is the stress-free reference *d*-spacing, which was measured away from the crack-tip at a corner of each CT specimen. Three residual stress components, $\sigma_i$ ($i = x, y, z$, corresponding to longitudinal, transverse and normal directions, respectively), are calculated from three strain components using the following equation:

$$\sigma_i = \frac{E}{1+\nu}\left[\varepsilon_i + \frac{\nu}{1-2\nu}\left(\varepsilon_x + \varepsilon_y + \varepsilon_z\right)\right] \quad (2)$$

where $E$ is the Young's modulus and $\nu$ is the Poisson's ratio.

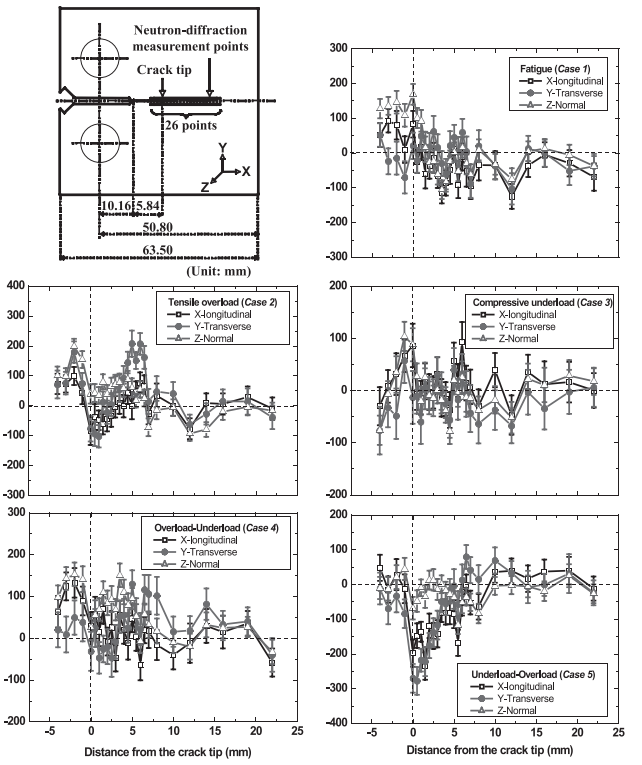


**Fig. 3** *Geometry of a compact-tension specimen of Hastelloy C-2000 alloy and residual stress distributions in the vicinity of the crack tip for the five different loading cases.*

Figure 3 shows the residual stress profiles around a crack tip after five different loadings (indicated in Figure 2). Note that Y-transverse stress is the most sensitive stress for crack closure study and is reported here. In the case of constant-amplitude fatigue (*Case 1*), the compressive residual stress of -70 MPa was examined at the 1 mm behind of the crack tip and no compressive stress was found at the region ahead of the crack tip.

After a single tensile overload was applied (*Case 2*), compressive residual stresses with the maximum of -102 MPa were measured within about 1.5 mm in front of the crack tip, which will reduce the crack-tip driving force, and, thus, will retard the crack propagation.

After a single compressive underload was introduced (*Case 3*), the tensile residual stress of 60 MPa was examined at 1 mm behind of the crack tip. The residual stress distributions at *Case 3* were very similar to those at *Case 1* but showed tensile stress at 1 mm behind the crack tip. It is expected that this tensile stress will result in the decrease of the crack opening level, and, hence, higher crack-tip driving force for crack growth. Therefore, immediately after a single compressive underload, an instantaneous acceleration of crack growth would be observed.

When a compressive underload was imposed right after a tensile overload (*Case 4*), relatively small compressive residual stresses (with the maximum of -47 MPa) were examined within 3 mm in front of the crack tip. It is believed that such reduced compressive residual stresses resulted in the reduced retardation period, as compared to the single tensile overloading case (*Case 2*).

When a tensile overload was applied immediately after a compressive underload (*Case 5*), large compressive residual stresses were found within ± 6 mm near a crack tip. At 0.5 mm in front of the crack tip, the largest compressive stress of -280 MPa was examined, which will significantly retard the crack propagation. It can be noted that different crack growth behaviors are closely correlated with the distinct residual stress distributions around a crack tip under the various loading conditions.

## Conclusion

From spatially-resolved strain scanning measurements, bulk residual stresses were successfully measured as a function of the distance from the crack tip, which allowed us to determine the kind and magnitude of residual stresses around a crack tip. The results will help us establish the relationship between crack-tip driving force and crack growth rate.

# Effect of Residual Stresses on the Distortion of Components after Machining

**J-F. Lalonde [1], M.A. Gharghouri [2], J-F. Chatelain [1]**

[1] Université du Québec, École de technologie supérieure, Montréal, Québec, Canada H3C 1K3

[2] Canadian Neutron Beam Centre, National Research Council, Chalk River Laboratories, Chalk River, ON, Canada K0J 1J0

The distribution of residual stresses induced by machining can affect the ability of a component to withstand severe loading conditions in service and may cause dimensional instability (distortion) during machining [1-4]. It is critical to be able to predict and thus control the residual stresses due to machining in order to enhance component performance. This is particularly important when critical structural components are machined, especially those used in the aerospace sector where productivity improvement and consistent part dimensionality are important [1].

Several groups have attempted to develop finite element approaches to predict residual stresses due to machining. The problem with the current models is that they do not take into account the initial residual stresses present in the raw material due to prior thermo-mechanical processing. To evaluate the initial stresses created by manufacturing and thermal processes, a non-destructive method is preferred, such that the parts can subsequently be used in machining tests [5]. Neutron diffraction is the best non-destructive method in this case because of the high penetration depth of neutrons, which allows data to be collected from all regions of a bulk specimen.

The objective of this research was to evaluate the impact of the initial residual stresses and machining stresses on the distortion of machined parts. Processes that minimize the residual stresses are now available on the market thus making it possible to carry out a comparative study on the influence of the constraints present before and after machining for different residual stress distributions. Therefore, we evaluate the residual stresses before and after the machining of a component for standard and for controlled process aluminums (see Figure 1).

Measurements were taken on six components before machining: three on the standard material and three on the controlled process material with low residual stresses. Because of the measurement time and the number of components to be measured, it was not possible to make a complete billet mapping. For each part, measurements were taken at 190 points corresponding to critical places where the component will be machined. Thus it was possible to compare the constraints before and after machining. Measurements were made using the {311} plane.

The results obtained lead to several observations. Initial measurements showed that there was symmetry in the residual stress distribution for standard material in the longitudinal direction only. For material with controlled process, there was symmetry in three directions: longitudinal, transverse and normal. Secondly, a high level of consistency was observed between specimens of the same material. However, the two types of material had different stresses distributions. The stresses obtained for aluminum with the controlled process showed weak variations and were always very close to the zero, but the curves obtained for standard aluminum showed more significant variations (Figure 2). The directions of the constraints, tension or compression, are not the same for the corresponding positions of measurements on the two materials. These variations could be at the origin of the deformations generated following the addition of the residual stresses induced by machining. Some researchers claim indeed that distortion can be generated when the stresses added by machining exceed the yield point of the material [6].

The neutron diffraction measurement method does not make it possible to measure the distribution of machining residual stresses through an entire thin wall of 0.080" [2 mm]. But it was possible to obtain the average stress in a point located at the center of the wall. The positioning of the points was critical because of the 2 mm measurement volume. Since the machined components were not straight, several wall scans were carried out in order to compensate for part distortion. We found that the distribution of stress for the machined part with standard material and with controlled process material correlates well with the geometrical deformations.

Thus, use of material whose process is controlled to minimize initial constraints solves the problem of the distortion because the residual stresses present in rough material are partly responsible for the distortion. All the parts machined in standard material underwent deformations while the parts machined in material with controlled process underwent very few deformations (see Figure 3). The neutron diffraction method shows that the distribution of the constraints, their signs, and their intensities can be at the origin of the deformations.

In the future, it will be interesting to repeat measurements on a standard billet and a controlled process billet by carrying out a complete mapping of the component. The results obtained would then be easier to analyze and they could possibly be used to solve the problem with the finite elements method. Also, a difference in the intensity of the neutrons beam was observed for the two types of aluminums during measurements. This observation suggests a difference in the granular structure coming from the

forming processes. According to the theory, the grains of standard aluminum have a lengthened form in the rolling direction while those of controlled process aluminum are smaller and more uniform [7]. The size and the orientation of the grains could possibly have an influence on the distribution and the amplitude of the residual stresses.

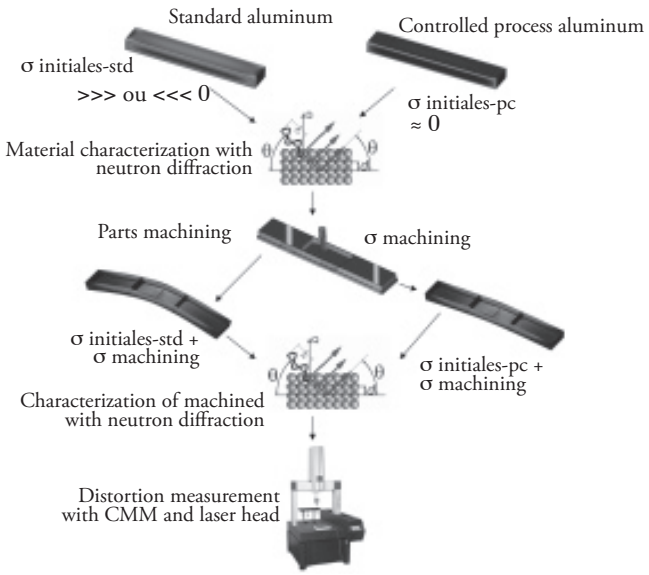


***Fig. 1*** *Methodology used to compare the distortion of parts for both types of aluminum.*

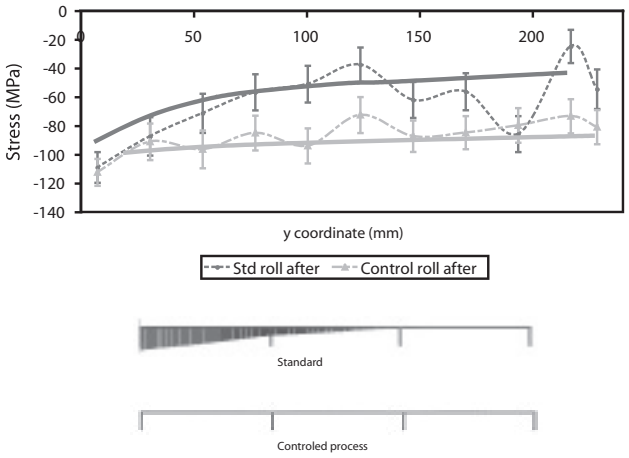


***Fig. 2*** *Residual stresses after machining in the rolling direction for the standard and the controlled process materials. The lower panel shows a 2D representation of the parts deformation measured with a 3D laser scanning technique.*

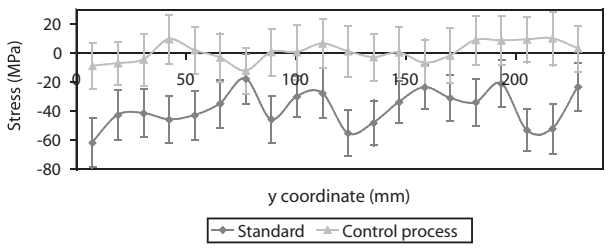


***Fig. 3*** *Raw material normal residual stresses in the Y direction for the standard and the controlled process aluminum.*

## References


[1] Young, Keith. A. May 2005. Machining-induced residual stress and distortion of thin parts. Doctor of Science, Saint-Louis, Missouri, Washington University, 150 p.

[2] Prime, M. B., Hill, M. R. 2002a. Residual Stress, Stress Relief, and Inhomogeneity in Aluminium Plate. Scripta Materialia. 46(1):77-82. http://www.lanl.gov/residual/alumsm.pdf.

[3] National Physical Laboratory. 2006. The UK's National Laboratory Internet site. In. http://www.npl.co.uk/materials/residualstress/. Accessed 13 May 2006.

[4] Physique & Industrie. 2006. Physique & Industrie Internet site. In. http://www.physiqueindustrie.com/residual_stress.php. Accessed 28 April 2006.

[5] Kandil, F.A., Lord, J.D., Fry, A.T., Grant, P.V. 2001. A Review of Residual Stress Measurement Methods - A Guide to Technique Selection. In. http://www.npl.co.uk/materials/residualstress/publications.html. Accessed 28 April 2006.

[6] Totten, George E., et D. Scott Mackenzie. 2003. Handbook of Aluminum. New York; Basel: Marcel Dekker Inc., v. 2.

[7] Sitdikov, O. Sh, A. N. Goloborod'ko, R. O. Kaibyshev, H. Miura et T. Sakai. 2005. Effect of strain rate on the formation of fine-grained microstructure in a cast aluminum alloy 7475 upon high-temperature upsetting. Physics of Metals and Metallography. 99(1):106-117.

[8] Pang, J. W. L., Holden, T. M., Mason T. E. 1998. In situ generation of intergranular strains in an AL7050 alloy. Acta mater. 46(5): 1503-1518.

# Residual Stress Characterization of a Fabrication Weld from the Victoria-Class Submarine Pressure-Hull

**R. McGregor [1], R. Rogge [2]**

[1] Defence R&D Canada Atlantic, Dockyard Laboratory Pacific, Victoria, BC, Canada, V9A 3E9

[2] Canadian Neutron Beam Centre, National Research Council, Chalk River Laboratories, Chalk River, ON, Canada K0J 1J0

## Background

The operational demands of naval platforms can benefit from explicit understanding of the structural impact of fabrication residual stresses. Such accounting supports full exploitation of the operational envelope in emergency or combat situations and design-life extension initiatives.

A length of circumferential-seam closure-weld was contained within a section of hull-plate recently removed from the HMCS Victoria submarine during refit operations. This plate was given to DRDC Atlantic, Dockyard Laboratory Pacific for metallurgical research and has provided a rare opportunity for detailed study of the thru-thickness as-received condition of this common weld-type from original vessel assembly, using techniques not otherwise possible. The results can be considered representative of all legacy circ-seam welds, and can be exploited within numerical models supporting operational limits such as diving depth for Canada's new VICTORIA Class fleet. [1]

## Objectives

The plan was to first survey the through-thickness residual strain gradient in an as-rolled plate section (not welded or otherwise cold or hot-worked) to characterize the plate fabrication residual stress effects and provide a comparative baseline for the primary study of the circ-seam weld; and second to characterize the through-thickness residual stress distribution in the vicinity of the circ-seam weld and an adjacent fit-up discontinuity (potential bounding case of pressure-hull cold-work). A grid pattern strain survey in the three principal stress directions would allow one and two-dimensional presentation of interpreted stress data.

The residual stress character within the weld was surveyed with the L3 Neutron Diffractometer. The experiment was performed over a four-week period around October 2007, with DRDC personnel supporting on-site.

## Results

The neutron diffraction survey has provided the residual stress distribution shown in Figure 1 for the circ-seam weld transverse direction. Results indicate that OD surface tensile stress peaks exist in the weld transverse direction at levels around 80% of material tensile yield. Longitudinal direction tensile surface stresses are lower in magnitude but similarly fall off to compressive levels at the weld centre line before increasing to higher tensile levels again toward the ID. Measurements are consistent with distributions from numerical analysis and 'surface-only' X-ray diffraction studies on similar weldments from other studies. [2,3,4,5]

From the trend apparent in the through-thickness stress distribution, weld finishing by flush grinding may have served to mechanically remove the highest tensile weld stresses which tend toward the OD surface (Figure 1, note that the micrograph X and Y axes do not have the same scale). Also, the evidence of the back gouge in the Figure 1 micrograph may be attenuating tensile magnitudes on the ID. Flame cutting or the cold work of the dent - both in the vicinity of the test plane - appear to have insignificant polluting effect on the weld stress data. There is little evidence of the effect on the residual stress distribution of the fit-up undulation that runs parallel and immediately adjacent to the circ-seam weld. It seems, therefore, that whatever stresses may have resulted from the fit-up deformation have either been relieved in the welding process or are at least dominated by the weld stresses.

## Summary

Data has been obtained to enhance the validity of DRDC's pressure-hull numerical models, metallurgical experimentation initiatives, and X-ray diffraction residual-stress techniques. This will support design enhancement or operational envelope analysis and evaluation for emergency and combat operations including ultimate diving depth determination, structural "weak link" isolation (incipient buckling), and design-life limit assessment and extension (fatigue margin, stress corrosion cracking resistance).

Results can also serve to renew relevance to the existing body of "surface-only" work that has been conducted on actual submarine hulls. Results are available to DRDC for use in other research areas such as submarine hull numerical modeling, X-ray diffraction validation, and fracture mechanics experimentation.

Chalk River has a history of support to DRDC submarine scientific programs for the Oberon Class fleet. [6] This current study has provided a very successful initial interface between NRC-CNBC and the new Submarine Scientific Support Service Level Arrangement that DRDC maintains with Department of National Defence for the recently acquired Victoria-Class fleet. This SLA program is presently engaged in various pressure-hull R & D activities; the NRC's unique residual stress characterisation capabilities have been anticipated as solutions to some of the challenges within these programs. DRDC expects to apply for similar residual stress characterization support in the near future.

This work is a component of the DRDC Atlantic, Submarine Scientific Support Service Level Arrangement. The project was conducted in collaboration with NRC Canadian Neutron Beam Centre with the support of Dr. Ronald Rogge.

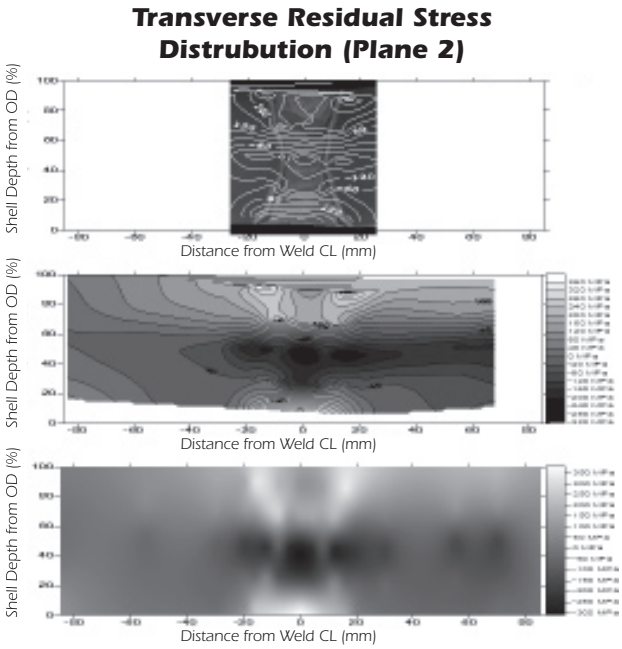


**Fig. 1** Distribution of transverse-direction residual stress over the hull circ-seam weld using different visualization approaches.

## References

[1] Smith, M., Structural Modelling and Strength Assessment of the Victoria-class Submarine Pressure Hull. Maritime Engineering Journal, Fall 2005.

[2] Porter, J. F. Residual Stress Evaluation of HMCS Onandaga Pressure Hull Weldments, Canadian Forces / CRAD Meeting, DREA – Halifax, May 1985.

[3] Porter, J.F., Brauss, M. F., Pineault, James. X-ray Diffraction Determination of Residential Strain for Marine Platforms, 2nd Canadian Forces / CRAD Meeting on Naval Applications of Materials Technology, DREA-Halifax, May 1985.

[4] Brauss, M. Wong, H., Holt, R.A., Fryzuk, P. Non-Destructive Evaluation of Oberon Submarine Pressure Hull Residual Stress. 2nd Canadian Forces /CRAD Meeting on Research In Fabrication and Inspection of Submarine Pressure Hulls, DREA-Halifax, May 1987.

[5] Farrell, S., Bayley, C. Assessment of Residual Stress Proximal to the Dent Repair Area of HMCS Victoria. DRDC-Atlantic Technical Memorandum TM2006-275, November 2006

[6] Clark, Percy., Holden, Tom., Porter, John., Yee, Richard., Diffraction Measurements on CPF Steel Fatigue Samples. Canadian Forces / CRAD-Meeting, DREA – Halifax.

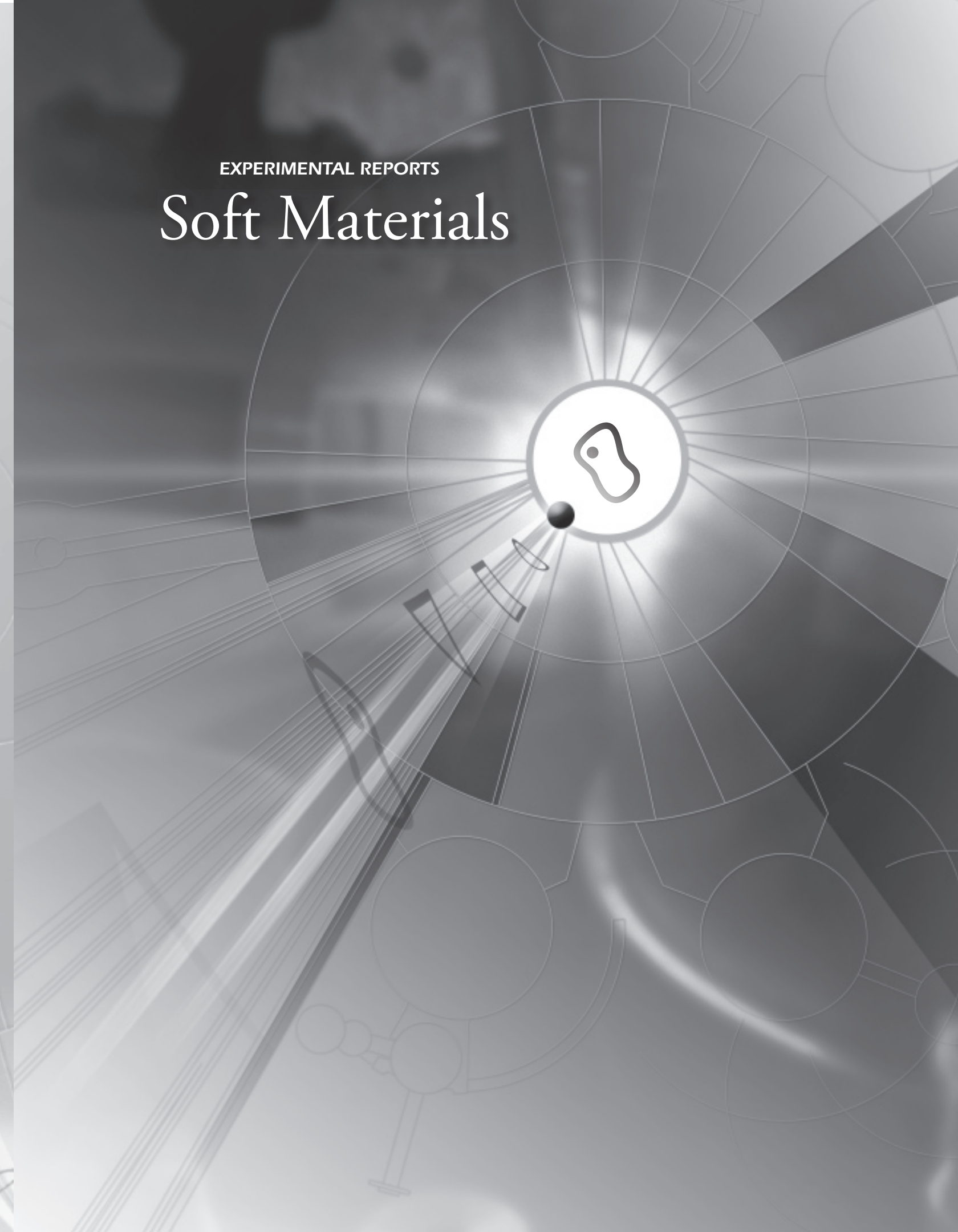

EXPERIMENTAL REPORTS

# Soft Materials

# Adapting N5, A Triple-axis Spectrometer, for Small Angle Neutron Scattering Measurements

**M-P. Nieh [1], Z. Yamani [1], N. Kučerka [1], J. Katsaras [1], D. Burgess [2], and H. Breton [2]**

[1] Canadian Neutron Beam Centre, National Research Council, Chalk River Laboratories, Chalk River, ON, Canada K0J 1J0

[2] Design and Fabrication Services, National Research Council Canada, 1200 Montreal Road, Ottawa, Ontario, Canada K1A 0R6

Small angle neutron scattering (SANS) is a powerful technique for the study of molecular structures and morphologies with length scales ranging from 10 Å to 1000 Å. Dedicated SANS instruments cover a scattering vector range ($q$-range) from 0.001 to 0.6 Å$^{-1}$, where q is defined as:

$$q = \frac{4\pi}{\lambda}\sin\left(\theta/2\right),$$

where and λ and θ are the neutron wavelength and scattering angle, respectively.

Presently, at the Canadian Neutron Beam Centre (CNBC) no cold source is available in the 120 MW National Research Universal (NRU) reactor. In order to adapt a triple-axis spectrometer for small angle measurements, the incident beam therefore needs to be highly collimated. Moreover, the use of a single crystal monochromator to select the wavelength of the incident neutrons ($\Delta\lambda/\lambda < 1\%$), significantly reduces neutron flux on the sample compared to the use of a velocity selector ($\Delta\lambda/\lambda \sim 10\%$). To increase incident neutron flux, while not increasing the beam size, we have employed multiple incident beams that converge at a spot on the detector, first proposed and tested by Nunes [1]. At CNBC, we have designed and implemented such a confocal Soller collimator (CSC, as shown in Figure 1). The CSC is 66 cm long and made up of 23 channels, whereby each channel is separated by 0.25 mm spring steel blades coated with $Gd_2O_3$. All channels converge on the same spot at the detector. Each individual channel has dimensions of 3.8 cm (high) by 0.13 cm (wide) at the monochromator end and 3.8 cm (high) by 0.10 cm at the end closest to the sample.

The experimental configuration for adapting the N5 triple-axis spectrometer to SANS measurements is shown in Figure 2. In order to cover a wide $q$-range, three values of λ (2.37, 4.00 and 5.23 Å) are used from the (002) crystal plane reflection of a PG monochromator at monochromator angles ($\theta_M$) of 20.69°, 36.50° and 51.25°, respectively. However, the incident neutron beam can be contaminated by higher order harmonics of the fundamental neutron wavelength (i.e., λ/2, λ/3, etc.), which are reduced either through the use of a beryllium (Be) ($\lambda > 3.99$ Å) or pyrolytic graphite (PG) filter ($\lambda = 2.37$ Å). A sapphire filter is optionally used for reducing the presence of "fast neutrons" in the incident beam [2]. Therefore, depending on the chosen wavelength, either a sapphire ($\lambda \leq 3.99$ Å), or Be ($\lambda > 3.99$ Å) filter (component 1 in Figure 2), cooled to liquid nitrogen temperature is placed upstream of the PG monochromator (component 2 in Figure 2). Moreover, due to the slit geometry of the incident beam, a 48 cm-long horizontal Soller collimator (HSC) with individual channels of 0.25 cm vertical opening is required on the scattered side (detector) in order to reduce the smearing due to vertical divergence. In some cases where high resolution is required, a 21.6 cm long HSC with 0.25 cm vertical opening of individual channels is also placed prior to the sample position.

Figure 3 shows a comparison of the total intensity (all channels opened) with that from different channels. It is clear that the CSC enhances the incident neutron intensity by a factor of 20 compared with that from each individual channel, without any noticeable effect on the projected beam size (on the detector) and the attainable minimal $q$, $q_{min}$ is around 0.006 Å$^{-1}$. This development allows for the ubiquitous triple-axis spectrometer to have a capability of SANS, with little cost and effort.

Using this N5-SANS (Figure 2), we examined standard polystyrene microsphere samples with a diameter of 24 nm (PS02N, Bangs Laboratories). The microspheres arrived as 10 wt.% solutions and were subsequently diluted to 1 wt.% with $D_2O$ (Atomic Energy of Canada Limited, Chalk River, Ontario, Canada). The samples were loaded in rectangular quartz cells having a 5 mm path length. The absolute intensities (i.e., $d\Sigma/d\Omega$) for the sample are obtained from the NG3-SANS located at National Institute of Standards and Technology (NIST), as shown in Figure 4a. To obtain the best-fit structural parameters, NG3-SANS data are fitted using a core-shell-sphere model convoluted with the instrumental resolution. The same model and structural parameters are used to rescale the scattering data of the sample obtained from N5-SANS, however, this time taking into consideration the N5-SANS instrumental resolution (Figure 4b). The N5-SANS data are rescaled for each $q$-range and then plotted on the same figure. Slight discontinuities at the overlapping regions of the rescaled data are observed, presumably due to different resolution functions of the individual $q$-ranges. We find good agreement between NG3-SANS and N5-SANS data (Figure 4b) proving the successful implementation of this SANS design. The total data collection time at the N5-SANS was ~ 4.5 hours (1½ hours for $\lambda = 5.23$ Å, 1 hour for $\lambda = 4$ Å and 1 hour for $\lambda = 2.37$ Å), which is longer than that at NG3-SANS (40 minutes). The statistics of the N5-SANS data are poorer than those obtained at the NG3-SANS data. The reasons for this are twofold: (1) the small detecting area of the 32-wire N5-SANS detector (12 cm x 6.5 cm) requires multiple detector locations to cover a given $q$-range (compared to the much larger 2-D detector at NG3 with a size of 65 cm x 65 cm), and (2) for weakly

scattering samples, air scattering dominates at low-$q$, thus longer collecting times are needed to reduce the error bars when subtracting the air scattering from the sample scattering.

In this report, we have shown that the triple-axis spectrometer, N5, can be successfully used for SANS measurements with a simple installation of a CSC. Data (from 0.006 $Å^{-1}$ to 0.3 $Å^{-1}$) obtained from N5-SANS agree well with those collected from the well-established 30 m NG3-SANS. Fine adjustments such as the use of evacuated HSCs and multiple off-set monochromators can presumably improve the performance further.

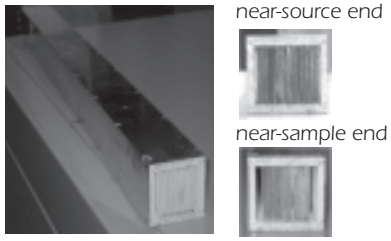


***Fig. 1*** *Photograph of the 23-channel CSC.*

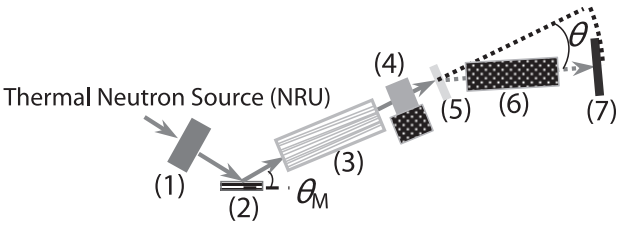


***Fig. 2*** *Schematic of the N5-SANS adapted from a triple-axis spectrometer. The components are as follows: (1) Sapphire or Be filter. (2) Monochromator. (3) 23-channel Converging Soller Collimator (CSC). (4) PG filter/21.6cm-long Horizontal Soller Collimator (HSC)/ open. (5) Sample. (6) 48cm long HSC. (7) 32-wire position sensitive detector.*

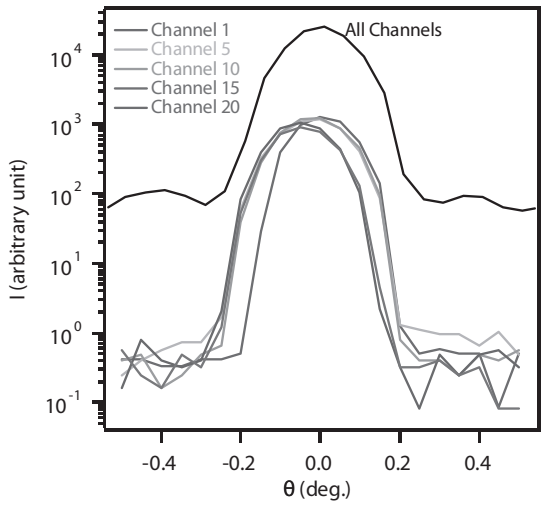


***Fig. 3*** *Comparison of incident beam intensity from individual channels (1, 5, 10, 15, 20) and all channels.*

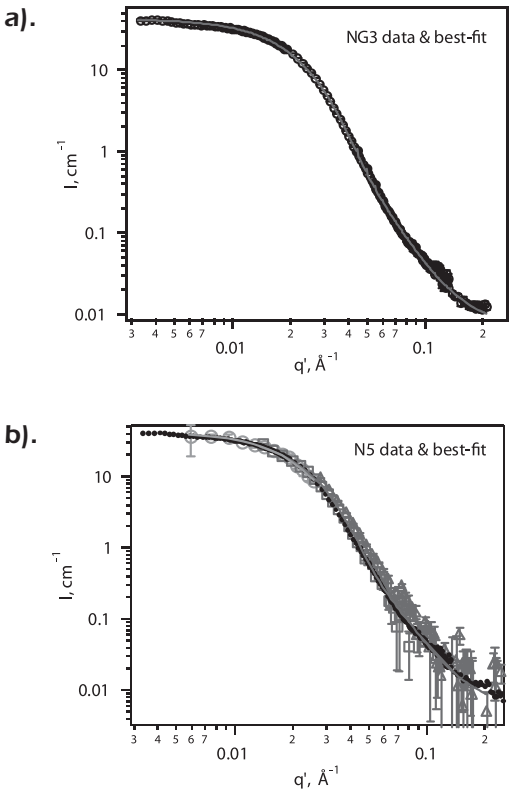


***Fig. 4*** *SANS data of 1 wt.% microspheres with a diameter of 24 nm obtained from (a) the NG3-SANS and (b) the N5-SANS. The best-fits using a core-shell-sphere model are shown as solid lines. N5-SANS data are rescaled using the same model and structural parameters as the NG3-SANS, but different instrumental resolution. Circles, squares and triangles in (b) represent the SANS configurations using λ = 5.23, 4, and 2.37 Å, respectively. NG3-SANS data (dots) are also plotted in (b) for comparison purpose.*

### References


[1] C. Nunes, Nuclear Instr. Methods 119, 291 (1974).

[2] H. F. Nieman, D. C. Tennant, and G. Dolling, Rev. Sci. Instrum. 51, 1299 (1980).

# Effect of Cations on the Structure of Bilayers Formed by Lipopolysaccharides Isolated from *Pseudomonas aeruginosa* PAO1

**N. Kučerka [1], E. Papp-Szabo [2], M.-P. Nieh [1], T. A. Harroun [3], S. R. Schooling [2], J. Pencer [4], E. A. Nicholson [1], T. J. Beveridge [2], and J. Katsaras [1]**

[1] Canadian Neutron Beam Centre, National Research Council, Chalk River Laboratories, Chalk River, ON, Canada K0J 1J0

[2] Department of Molecular and Cellular Biology, University of Guelph, Guelph, ON, Canada N1G 2W1

[3] Department of Physics, Brock University, 500 Glenridge Avenue, St. Catharines, ON, Canada L2S 3A1

[4] Atomic Energy of Canada Limited, Chalk River Laboratories, Chalk River, ON, Canada K0J 1J0 and Guelph-Waterloo Physics Institute, University of Guelph, Guelph, ON, Canada N1G 2W1

Bacterial lipopolysaccharides (LPSs, Figure 1) are the major lipid component making up the outermost leaflet of the asymmetric outer membrane (OM) of Gram-negative bacteria [1,2]. LPS contributes to the OM's structural integrity and also protects the bacteria from a variety of toxic molecules, such as certain antibiotics (e.g. penicillin), digestive enzymes (e.g. lysozyme), detergents, heavy metals, bile salts, and some dyes. On the other hand, the OM's inner leaflet is predominantly composed of common lipids such as phosphatidyl-ethanolamine (PE), phosphatidyl-choline (PC), phosphatidylglycerol (PG) and cardiolipin (diphosphatidylglycerol) [3]. The passage of nucleotides, disaccharides, amino acids, vitamins, and iron for nutritional growth are usually transported through the OM by porin proteins, but it is LPS that provides the bacteria with its remarkable selectively permeable membrane that is resistant to a variety of deleterious agents. In particular, *P. aeruginosa* is well-noted for its recalcitrance to conventional antibiotic therapy, partly as a result of its unique surface chemistry [4]. For this reason, and also due to the ubiquity of *P. aeruginosa* and its impact upon health as both an opportunistic and nosocomial pathogen, this organism represents an attractive candidate for study.

Here we report of the effects of three different cations (i.e. $Na^+$, $Ca^{2+}$, $Mg^{2+}$) on the multilamellar structure of bilayers formed using LPS isolated from *P. aeruginosa* PAO1. From the different one-dimensional neutron scattering length density (1D SLD) profiles, we find lower penetration of water molecules through $Ca^{2+}$-LPS bilayers, when compared to $Na^+$- or $Mg^{2+}$-LPS bilayers.

Features in the 1D SLD profile (Figure 2) can be associated with identifiable LPS chemical moieties. The bilayer is formed by two LPS monolayers, with their hydrophilic polysaccharide chains residing in the inter-layer water region, which in the 100% $D_2O$ case has the highest SLD. From the water region, the SLD decreases in a continuous fashion to the bilayer centre. The central bilayer region is made up of Lipid A hydrocarbon chains, which are calculated to extend about 12.5 Å on either side of the bilayer centre [5].

The hydrocarbon chains are attached to the Lipid A headgroup and the inner core, further extending the LPS molecule (from 12 to 24 Å on either side of the bilayer). The SLD profile is slightly higher in this region as it contains chemical groups with high neutron SLDs (e.g. phosphates and carboxylates). The SLD region associated with these groups is much more distinct in the case of $Ca^{2+}$-LPS bilayers, while in the case of $Na^+$-LPS bilayers this region is somewhat obscured by a presence of high SLD $D_2O$. Further increases to the SLD profile reflect the ever-increasing amounts of $D_2O$ into the outer core and O-side chain regions.

For the most part, the SLD profiles of $Ca^{2+}$- and $Na^+$-LPS exhibit the same structural features (Figure 2). Nevertheless, where they differ is in the outer/inner core region. In $Ca^{2+}$-LPS bilayers, compared to $Na^+$-LPS, the amount of water penetrating this region is substantially less. But they cannot be compared directly as a result of different scaling factors associated with the two SLD profiles. The differences in hydration between the two bilayers are better appreciated by referring to the water distribution profiles shown in Figure 3.

In the region ±14 Å from the bilayer centre, water molecules are seemingly distributed similarly in both $Ca^{2+}$- and $Na^+$-LPS bilayers, but differ outside of this region. In the case of $Na^+$-LPS bilayers the amount of water begins to increase at approximately ±14 Å (inset to Figure 3), while this increase is not seen until approximately ±22 Å (inset to Figure 3) in $Ca^{2+}$-LPS bilayers, indicating that the outer/inner core region of $Ca^{2+}$-LPS is substantially less hydrated. Interestingly, although the amount of water differs in the two systems, the shape of the water distribution functions are fundamentally similar, implying that the O-side chains are similarly hydrated.

In addition to $Ca^{2+}$- and $Na^+$-LPS bilayers, we studied the effect of $Mg^{2+}$ on LPS. Unfortunately, the $Mg^{2+}$-LPS bilayers yielded lower resolution diffraction patterns and as a consequence, less detailed 1D SLD profiles. Figure 4 compares the 1D SLD profiles for the three different systems reconstructed using only three Bragg reflections, thus ensuring a direct comparison between the various bilayers. Interestingly, there is little difference between the $Na^+$- and $Mg^{2+}$-LPS bilayers, implying that these two counterions have a similar effect on LPS, despite their different valence number.

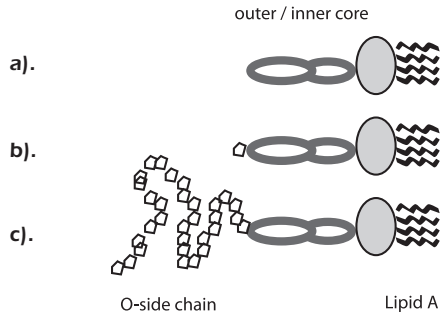


**Fig. 1** *Schematic of LPS architectures. LPSs consist of a hydrophobic region formed by lipid A, and an extensive hydrophilic region made up of the inner and outer cores, with additional O-side specific chains: (a) "Rough" LPS does not contain O-side chains. (b) "Semirough" LPS has an O-side chain with only one repeat unit. (c) "Smooth" LPS with an O-side chain made up of up to 50 trisaccharide repeat units.*

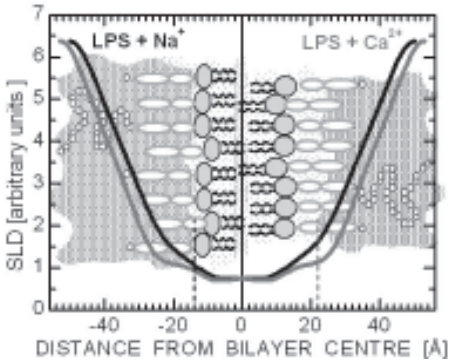


**Fig. 2** *Arbitrary scale 1D SLD profiles obtained from the Fourier reconstruction of diffraction data from oriented LPS bilayers hydrated in 100% D2O. The solid black line corresponds to $Na^+$-LPS bilayers, whereas the solid grey line corresponds to $Ca^{2+}$-LPS bilayers. The dashed lines demarcate the borders of regions that are highly accessible to water.*

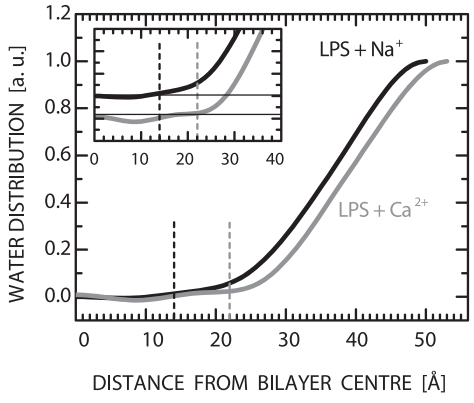


**Fig. 3** *Water distribution profiles of $Na^+$- and $Ca^{2+}$-LPS bilayers (only half of the bilayer is shown). The water distribution functions in the O-side chain region are similar for the two systems, whereas they differ in the bilayer core. The amount of water begins to increase at ± 14 Å in $Na^+$-LPS, whereas this increase is not seen until ± 22 Å in the case of $Ca^{2+}$-LPS bilayers, as emphasized in the inset (vertical offset was introduced for clarity purposes).*

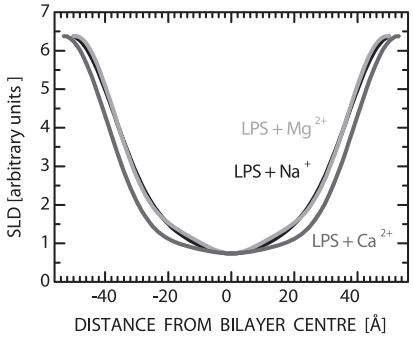


**Fig. 4** *1D SLD profiles calculated for oriented multilayers of $Na^+$-, $Mg^{2+}$-, and $Ca^{2+}$-LPS bilayers hydrated with 100% $D_2O$. All profiles were reconstructed using three Bragg reflections.*

## References


[1] Nikaido, H., Microbiol. Mol. Biol. Rev. 2003, 67:593-656.

[2] Wilkinson, S. G., Prog. Lipid Res. 1996, 35:283-343.

[3] Duong, F.; Eichler, J.; Price, A.; Leonard, M. R.; Wickner, W., Cell 1997, 91:567-573.

[4] Rocchetta, H. L.; Burrows, L. L.; Lam, J. S., Microbiol. Mol. Biol. Rev. 1999, 63:523-553.

[5] Abraham, T.; Schooling, S. R.; Nieh, M. P.; Kučerka, N.; Beveridge, T. J.; Katsaras, J., J. Phys. Chem. B 2007, 111:2477-2483.

# Effects of Additives on the Structure of Rhamnolipid (Biosurfactant): A Small-Angle Neutron Scattering (SANS) Study

**B. Dahrazma [1], C.N. Mulligan [2] and M-P. Nieh [3]**

[1] Department of Environmental Geology Faculty of Earth Science, Shahrood University of Technology, Shahrood, Iran 316-3619995161

[2] Department of Building, Civil and Environmental Engineering, Concordia University, Montreal, QC, Canada H3G 1M8

[3] Canadian Neutron Beam Centre, National Research Council, Chalk River Laboratories, Chalk River, ON, Canada K0J 1J0

Biosurfactants are surface active agents produced by microorganisms. The rhamnolipids used in this study, R1 and R2, are biosurfactants from the glycolipid group produced by the bacterium Pseudomonas aeruginosa [1, 2]. They are capable of effectively removing heavy metals (such as copper and zinc) from sediments [3, 4] and enhancing the removal of oil grease and metal ions from contaminated soil [5-7]. Addition of 1% NaOH showed significant enhancement of the removal of copper from sediments and mining residues [8]. The changes in heavy metal removal efficiency under different conditions presumably pertain to the change in the structure of rhamnolipid [6, 9, 10]. Small angle neutron scattering (SANS) has been widely used in resolving the structures of surfactants, phospholipids and microemulsions with the length scale ranged from 10 to 1000 Å. We have used the following two SANS instruments to investigate the morphology of the rhamnolipid in the absence and the presence of different additives including NaOH, KOH and NaCl to obtain more insight in to the structural transformations: NG3 at the National Institute of Standards and Technology (NIST) and E3 at the Canadian Neutron Beam Centre (CNBC).

The scattering data of the 2% rhamnolipid/D2O solutions containing 100mg/L of various ions (i.e., $Cu^{2+}$, $Ni^{2+}$, $Zn^{2+}$ and all three) obtained from E3 diffractometer (Figure 1) indicate that the scattering pattern strongly depends on the pH values of the systems instead of ions. All the curves of the samples in the basic condition collapse onto one curve with a low-q plateau followed by a high-q decay, indicative of small particles. This is different from all the scattering curves of the acidic samples, which have a common pattern that two monotonic decays with different slopes at low- and high-q regimes are observed. Due to a strong smearing effect from vertical divergence, a detailed analysis is not performed on these data. We conducted a detailed neutron scattering study using higher resolution NG3-SANS (at NIST) on representative samples, which were prepared including 100 mg/L of $Cu^{2+}$, $Ni^{2+}$ and $Zn^{2+}$ ions in 2% rhamnolipid/$D_2O$ solutions. The pH of the samples were adjusted using 10% $HNO_3$ and (1) NaOH (1M), (2) 1% NaOH, (3) 1% NaCl, and (4) 1% KOH, respectively to yield a value of 6.5 (S#1), 13.2 (S#2), 5.5 (S#3) and 13.2 (S#4), respectively.

The SANS data in Figure 2 shows that S#1 and S#4 have a similar pattern, while S#2 and S#3 are almost identical to each other. This result confirms the E3 neutron diffraction data, indicating that pH value is one of the most influential parameters on morphology. The scattering intensity of S#1 at the low q regime (from 0.003 Å-1 to 0.05 Å-1) follows a $q^{-2}$ decay, a characteristic of scattering from two-dimensional objects, presumably, unilamellar vesicles. Moreover, there are weak oscillations along the curve indicating the vesicular size distribution is somewhat narrow. Therefore, a simple model could be used, a polydisperse spherical shell [11], to fit the experimental data. The shell, presumably, is composed of the rhamnolipid bilayer and the best fitting result indicates a bilayer thickness of 15 ± 2 Å, an average diameter of 550 ± 50 Å and polydispersity of 0.28 ± 0.05.

The best fitting curve does not agree with the SANS data very well at low q, presumably due to the strong influence of interparticle interaction (known as the "structure factor") or the existence of another population of smaller aggregates (e.g. micelles). However, the feature of oscillation and the position of the broad peak are captured, indicative of reasonably reliable size and polydispersity from the best fitting result. In the case of S#4, whose pH value is lower than that of S#1, the scattering pattern also shows a $q^{-2}$ dependence at low q. However, the absolute intensity is slightly higher than that of S#1 at the same q-range and the intensity oscillation is almost absent with the broad peak seemingly shifting to a lower q value, indicative of a higher polydispersity and slightly larger particles in the system. After fitting the data using the same model, the bilayer thickness, diameter and polydispersity of the S#4 vesicles are obtained to be 14 ± 1, 580 ± 50 Å and 0.38 ± 0.10, respectively.

For both S#2 and S#3 (at strong basic condition), the intensity decays as a function of $q^{-4}$ (corresponding to Porod's law [12] of scattering from the interface) at the low-q regime ($q < 0.007$ Å$^{-1}$), indicative of the existence of large aggregates (> 200 nm). Then, the intensity remains practically constant over the q range between 0.012 and 0.06 Å$^{-1}$ followed by another $q^{-4}$ decay at $q > 0.1$ Å$^{-1}$, indicative of another population of smaller aggregates, possibly micelles (Figure 2). The scattering intensity contributed from the micelles can be approximated as the following where $(R_G^2 \cdot q^2/3) \leq 1$,

1). $$I(q) \approx I(0)e^{-R_G^2 q^2/3}$$

where I(0) and $R_G$ is the zero-angle intensity and radius of gyration of the micelles [12].

A Guinier plot, where ln[I(q)] is plotted against $q^2$, can therefore be constructed to obtain the dimension of the micelles (inset of Figure 2). This approach is based on the following two assumptions: the inter-micellar interaction is minimal, and the contribution of SANS intensity from large aggregates at the q region in interest (in this case, q > 0.03 Å-1) is negligible. The obtained slope of the line, ln[I(q)] vs. $q^2$, is $-R_G^2/3$ according to Equation 1. Applying the Guinier plot on the SANS data over a q range between 0.04 and 0.1 $Å^{-1}$ results in a value of $R_G$ = 17.2 ± 1.0 Å. The same data analysis can be applied to the scattering curve of S#3 as well. The obtained $R_G$ is 17.9 ± 1.0 Å, which is practically the same dimension as that of S#2 within the error. Therefore, it can be concluded that they presumably have the same micellar structure. The data are also fitted by a spherical model (the solid curves) [13] yielding a radius of 17.5 Å for both cases confirming the result from Guinier analysis. Since the larger aggregates (causing the uprising at low q) are outside the scale of the SANS probing range, we cannot conclude the structure based on current SANS data. However, they are possibly not of unilamellar structure, since the scattering decay follows $q^{-4}$ instead of $q^{-2}$.

In conclusion, we are able to successfully obtain the global structures of R1 and R2 aggregates in solutions using SANS. Based on the SANS data, it can also be concluded that pH is the determining factor for the transition. In fact, the pH-sensitive vesicles have the potential for the use of controlled release nanoparticles to deliver drugs. From an environmental standing point, the pH in the media to which the metal techniques applied is a major controlling parameter in the efficiency of the process. This is due to change in the morphological transition of the rhamnolipid structure.

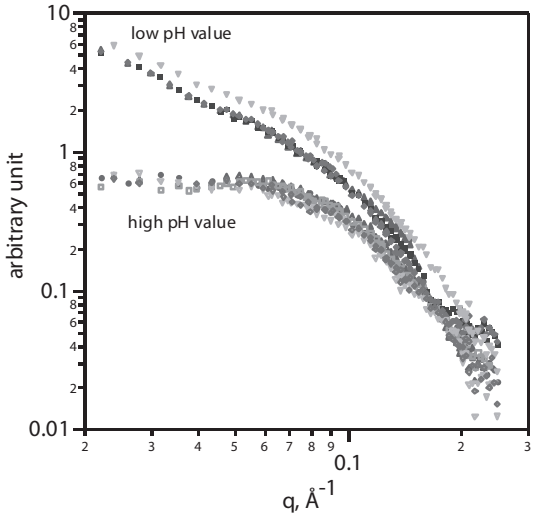


**Fig. 1** CNBC E3 neutron diffraction data for samples of various ion dopants at acidic (solid symbols) and basic (open symbols) conditions: no dopant: (diamonds), $Cu^{2+}$ (tip-up triangles), $Ni^{2+}$ (squares), $Zn^{2+}$ (tip-down triangles), all ions ($Cu^{2+}$, $Ni^{2+}$, $Zn^{2+}$, circles).

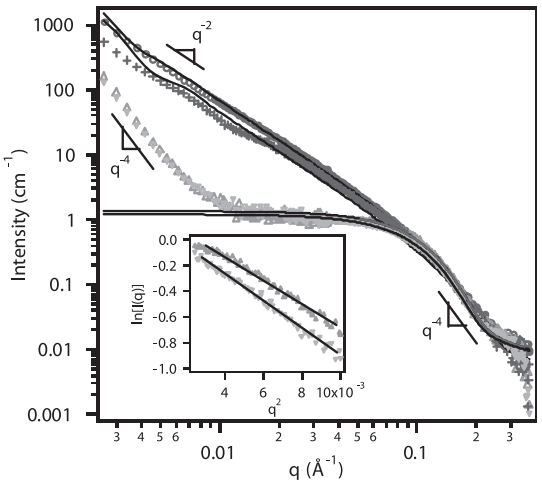


**Fig. 2** NIST SANS data of S#1 (crosses), S#2 (tip-down triangles), S#3 (tip-down triangles) and S#4 (circles). The solid curves are the best fitting results for S#1 and S#4 using the polydisperse spherical shell model and S#2 and S#3 using spherical model. Inset: Giunier plots [ln(I) vs. $q^2$] of S#2 (tip-down triangles) and S#3 (tip-up triangles). The slopes of the solid regression lines, $-R_G^2/3$, reveal the size of micelles.

## References


[1] K. Hitsatsuka, T. Nakahara, N. Sano, K. Yamada, Agric. Biol. Chem. (1971) 686.

[2] K. Tsujii, Surface Activity, Principals, Phenomena, and Applications, Academic Press, USA (1998).

[3] C. N. Mulligan, R. N. Yong, B. F. Gibbs, J. Hazard. Mat. 85 (2001) 111.

[4] C.N. Mulligan, B. Dahrazma, ASTM STP 1442 (2003) 208.

[5] S. Kyung-Hee, K. Kyoung-Woong, Environ. Geochem. Health,26 (2004) 5.

[6] C. N. Mulligan, R. N. Yong, B. F. Gibbs, Environmental Progress 18 (1999) 50.

[7] J. E. McCray, G. Bai, R. M. Maier, M. L. Brusseau, J. Contam.Hydrol. 48 (2001) 48.

[8] C.N. Mulligan, B. Dahrazma., 15th International Biohydrometallurgy Symposium (IBS), Athens, Hellas (2003).

[9] B. Dahr Azma, C.N. Mulligan, Prac. Period. Hazard. Toxic Rad. Waste Manag., 8 (2004) 166.

[10] J. T. Champion, J. C. Gilkey, H. Lamparski, J. Retterer, R. M. Miller, J. Col loid . Interface Sci., 170 (1995) 569.

[11] M.-P. Nieh, C. J. Glinka, S. Krueger, R. S. Prosser, J. Katsaras, Biophys. J., 82 (2002) 2487.

[12] G. Porod, in Small Angle X-Ray Scattering; O. Glatter, O. Kratky (Eds.), Academic Press, New York, 1982, Chapter 2.

[13] S. R. Kline, J Appl. Crystallogr. 39 (2006) 895.

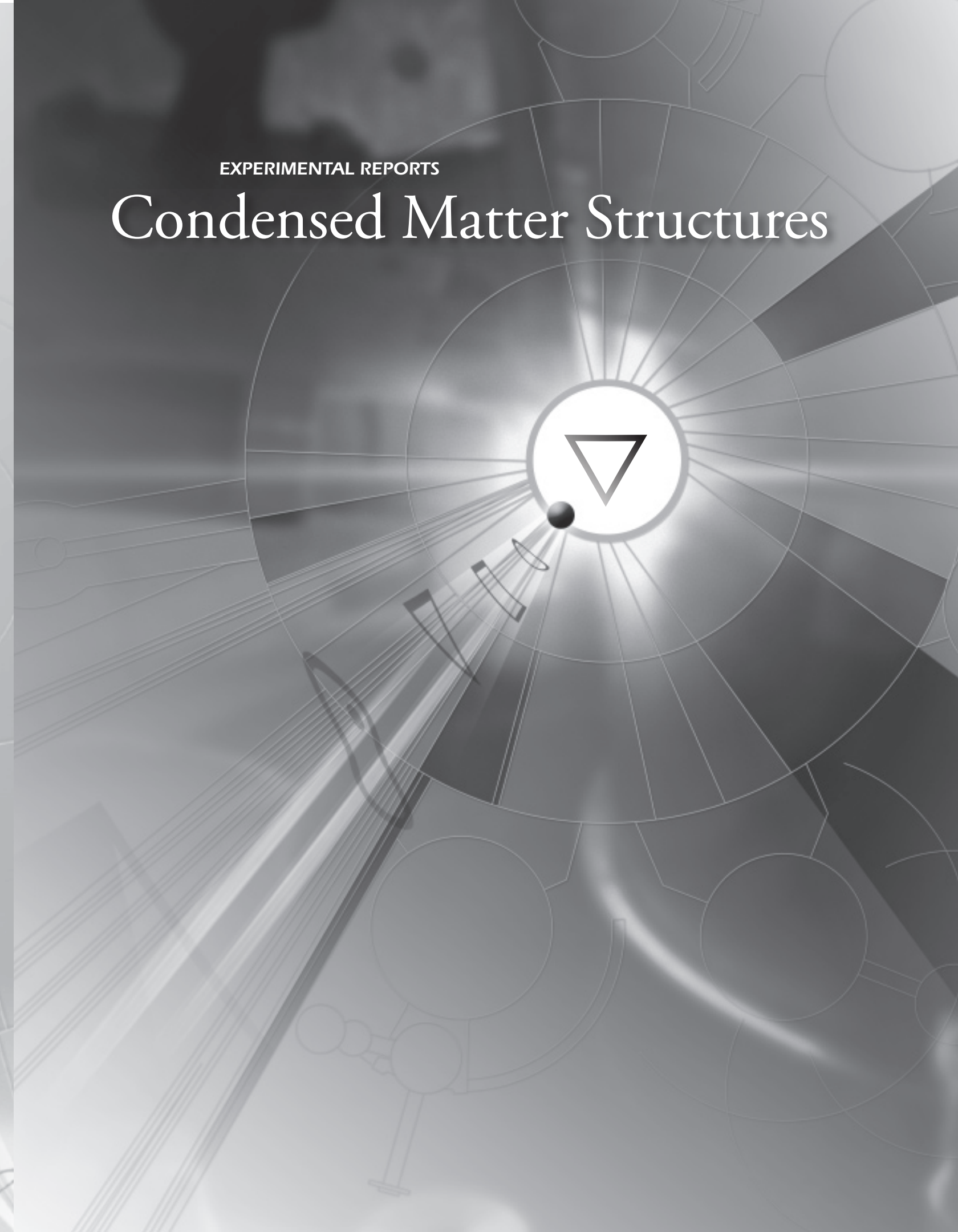

EXPERIMENTAL REPORTS

# Condensed Matter Structures

# Structure determination of the novel borate oxide, $SrBi_2OB_4O_9$

**J. Barbier [1] and L.M.D. Cranswick [2]**

[1] Department of Chemistry, McMaster University, Hamilton, ON, Canada L8S 4L9

[2] Canadian Neutron Beam Centre, National Research Council, Chalk River Laboratories, Chalk River, ON, Canada K0J 1J0

The $SrBi_2B_4O_{10}$ compound was discovered in 2006 during exploratory syntheses of novel bismuth borates for potential applications as nonlinear optical materials. The compound melts incongruently and single crystal growth has not been attempted. Instead, it was decided to attempt an ab-initio structure determination using a combination of high-resolution X-ray and neutron powder diffraction data. The X-ray data were collected on a Panalytical Expert diffractometer at McMaster Univerity and the neutron data were collected on the C2 diffractometer at Chalk River.

A 10-gram powder sample of $SrBi_2B_4O_{10}$ was synthesized by solid-state reaction using a stoichiometric mixture of high-purity $SrCO_3$, $Bi_2O_3$ and $^{11}B$-enriched (99.3%) $B(OH)_3$ powders heated to 650°C over several days with intermediate mixings. The neutron diffraction patterns were measured at room temperature in 0.05° steps at two different wavelengths of 2.37150 and 1.33063 Å. The availability of the longer wavelength was found advantageous during the structure solution step by minimizing the strong peak overlap associated with the unit-cell geometry (a = 6.86562 Å, b = 9.79777 Å, c = 6.81478 Å, $\alpha$ = 109.126 °, $\beta$ = 101.89 °, $\gamma$ = 96.14 °) (Fig. 1).

The direct-space global optimization progam FOX [1,2] was used to solve the structure of $SrBi_2B_4O_{10}$ ab initio from the combined X-ray and neutron diffraction data. As expected, the X-ray pattern was insensitive to the B and O atoms in the presence of the heavy Bi and Sr atoms, and the neutron data were essential for a successful structure solution. Initially, several structural models with different combinations of $BO_3$ and $BO_4$ groups were found to provide similar fits to the experimental data. The determination of the correct model was made possible by collecting 11B NMR spectra at McMaster University that indicated a 3:1 ratio of $BO_3$ to $BO_4$ groups in the structure. FOX then established the presence of one Sr site, two Bi sites, one isolated $B_4O_9^{6-}$ borate anion and one additional $O^{2-}$ oxide anion to yield a borate oxide composition of $SrBi_2B_4O_{10}$ with two formula units per unit-cell (P-1 space group). The crystal structure was subsequently refined with the Rietveld program PROF (Table 1) [3]. The large displacement parameters for the S, Bi and O5 atoms suggest some residual disorder or a distortion to P1 symmetry for the crystal structure. This point remains to be elucidated.

The structure of $SrBi_2B_4O_{10}$, or $SrBi_2OB_4O_9$, consist of $SrB_4O_9^{4-}$ and $Bi_2O^{4+}$ layers alternating in the [010] direction (Fig. 2). The asymmetric coordination of the Bi atoms and the short Bi-O bonds (2.10 - 2.28 Å) are typical of the $Bi^{3+}$ ion with a stereoactive lone pair, as also observed in $BaBiBO_4$ [4] and $SrBi_2B_2O_7$ [5]. The presence of borate and oxide anions distinguishes the structure of $SrBi_2OB_4O_9$ from that of $BaBi_2B_4O_{10}$ which only contains the $B_4O_{10}^{8-}$ borate anion[6].

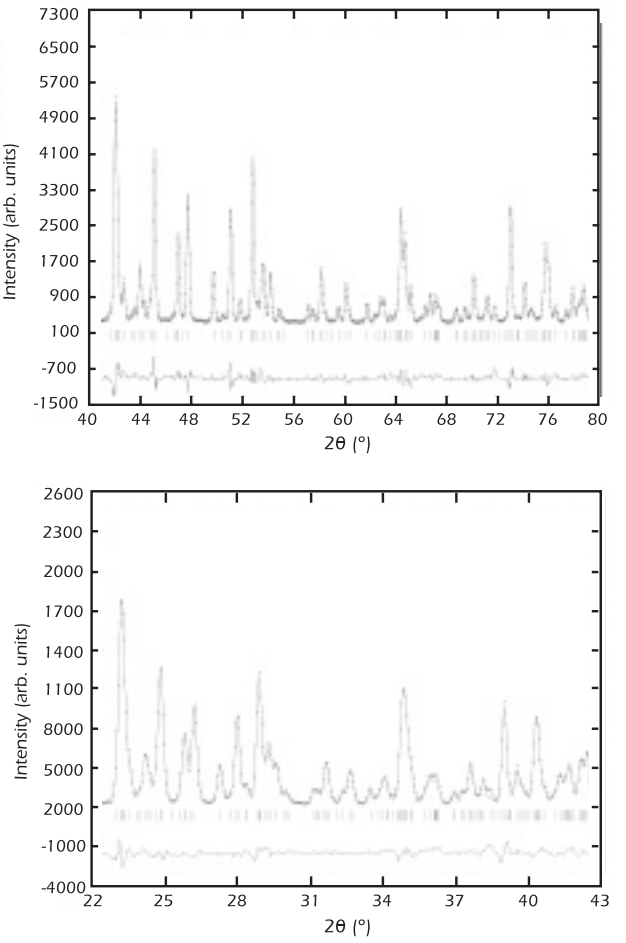


***Fig. 1*** *Selected regions of final Rietveld plots for the structure refinement of $SrBi_2OB_4O_9$ illustrating the much improved peak resolution at higher neutron waveleength, 2.3715 Å (top) vs. 1.3306 Å (bottom).*

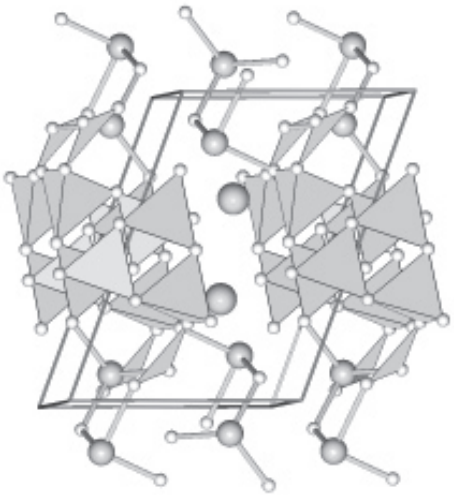

**Fig. 2** *Drawing of the $SrBi_2OB_4O_9$ structure illustrating the $SrB_4O_9^{4-}$ and $Bi_2O^{4+}$ layers alternating in the [010] direction, and the asymmetric coordination of the $Bi^{3+}$ ions. Large, medium and small spheres represent Sr, Bi and O atoms, respectively. Only the short Bi-O bonds (less than 2.3 Å) are shown.*

| | x | y | z | B (Å2) |
|---|---|---|---|---|
| Sr | 0.6503(7) | 0.3352(5) | 0.4671(7) | 1.86(11) |
| Bi1 | 0.4802(3) | 0.0974(3) | 0.8014(4) | 2.44(4) |
| Bi2 | 0.8640(3) | 0.8368(3) | 0.7658(4) | 2.44(4) |
| B1 | 0.2019(12) | 0.3258(9) | 0.6981(13) | 0.66(8) |
| B2 | 0.7525(12) | 0.4024(9) | 0.0894(12) | 0.66(8) |
| B3 | 0.1051(11) | 0.8663(9) | 0.3485(13) | 0.66(8) |
| B4 | 0.2916(13) | 0.4275(9) | 0.0980(12) | 0.66(8) |
| O11 | 0.3192(14) | 0.2502(10) | 0.5553(14) | 0.82(6) |
| O12 | 0.2841(13) | 0.3190(10) | 0.9087(13) | 0.82(6) |
| O13 | 0.2068(14) | 0.4834(9) | 0.7193(14) | 0.82(6) |
| O14 | -0.0121(12) | 0.2513(10) | 0.6127(15) | 0.82(6) |
| O21 | 0.7263(14) | 0.2612(9) | 0.0804(15) | 0.82(6) |
| O23 | 0.7352(15) | 0.4330(10) | -0.0969(14) | 0.82(6) |
| O31 | 0.3142(12) | 0.8963(10) | 0.4197(15) | 0.82(6) |
| O32 | 0.0036(13) | 0.9478(10) | 0.2528(15) | 0.82(6) |
| O42 | 0.3372(14) | 0.4053(11) | 0.2866(14) | 0.82(6) |
| O5 | 0.3892(15) | 0.0849(11) | 0.1438(15) | 1.29(20) |

**Table 1** *Atomic coordinates and displacement parameters for $SrBi_2OB_4O_9$ from the combined Rieveld refinement of one X-ray and two neutron powder diffraction data sets (combined $\chi^2 = 5.71$). Unit-cell data: a = 6.86602(1) Å, b = 9.79834(1) Å, c = 6.81524(1) Å, $\alpha$ = 109.1268(1) °, $\beta$ = 101.8973(1) °, $\gamma$ = 96.1452(1)°, Z =2 , P-1).*

### References


[1] Favre-Nicolin, V. and Cerny, R. (2002). "FOX, 'free objects for crystallography': a modular approach to ab initio structure determination from powder diffraction." J. Appl. Cryst. 35, 734-743.

[2] Favre-Nicolin V. and Cerny R. (2004). A better FOX: using flexible modelling and maximum likelihood to improve direct-space ab initio structure determination from powder diffraction. Z. Kristallogr. 219, 847–856.

[3] Rodriguez-Carvajal, J. (2004). FULLPROF version 2.55, Institut Laue-Langevin, Grenoble, France.

[4] Barbier J., Penin N., Denoyer A. and Cranswick L.M.D. (2005) "$BaBiBO_4$, a novel non-centrosymmetric borate oxide", Solid State Sci. 7, 1055-1061.

[5] Barbier J. and Cranswick L.M.D. (2006) "The non-centrosymmetric borate oxides, $MBi_2B_2O_7$ (M = Ca, Sr)" J. Solid State Chem. 179, 3958-3964.

[6] Bubovna R.S., Krivovichev S.V., Filatove S.K., Egorysheva A.V. and Kargin A.F. (2007) "Preparation, crystal structure and thermal expansion of a new bismuth barium borate, $BaBi_2B_4O_{10}$" J. Solid State Chem. 180, 596-603.

# The Influence of the Loading Conditions on the Transformation Behavior of Retained Austenite in TRIP Steel

**W. Dabboussi [1], J. Qu [1], J.A. Nemes [1], S. Yue [1]**

[1] Dept. of Metallurgical Engineering, McGill University, Montreal, QC, Canada H3A 2B2

Transformation Induced Plasticity (TRIP) is a promising strengthening mechanism in high strength low alloy multiphase steels. A potential 15-25% of vehicles' weight reduction makes these steels attractive for use in the automotive industry in particular. The source of the strengthening is the strain-induced martensitic transformation occurring during deformation where metastable retained austenite transforms into martensite. The metastable retained austenite transformation, 10 - 20% volume fraction, is well know to be influenced by several physical conditions such as strain, strain rate and stress state (triaxiality) amongst others. These conditions are similar to those encountered during dynamic events such as crash. Therefore a precise understanding of their influence on the transformation kinetics of the retained austenite warrants mechanical lab experiments on various samples under various conditions. This understanding would ultimately lead to the accurate mathematical modeling of TRIP steels and allow for a full exploitation of these steels' potentials. Therefore the accurate quantification of the retained austenite volume fraction in the tested samples is imperative to the success of this project. Various methods exist for quantifying retained austenite content in steels including optical methods, X-ray diffraction, Mössbauer Spectroscopy and neutron diffraction, but of these techniques neutron diffraction is the most precise.

TRIP steel is prepared following a two-stage heat treatment process in which the parameters at each stage are temperature and time. The variation of time and temperature at each stage results in steel with various amounts and properties of retained austenite. In the initial stage of this project, varying the time and temperature at each stage produces a matrix of materials used to determine the material with the optimal properties and amount of retained austenite that will be further investigated.

Thus far, two steels with different chemical composition have been mapped to understand the effect of the heat treatment parameters on the resultant retained austenite content. To date, there has no other such study on hot rolled TRIP steels. Moreover, the variation of retained austenite with strain was determined for two types of tests (tension and compression) at quasi-static strain rate. Varying testing conditions elucidates the influence of the stress triaxiality on the rate of transformation of the retained austenite and will help determine the stress state parameters in the retained austenite transformation kinetic model being developed. This model will eventually be incorporated in a rate dependent plasticity constitutive model for predicting the mechanical response of automotive TRIP steels under physical conditions comparable to those experienced during car crash.

The results obtained in the first phase of this study are shown in Figure 1, and have also been presented at the SAE 2007 World Congress [1] and at the ASME Applied Mechanics and Materials Conference, McMat 2007.

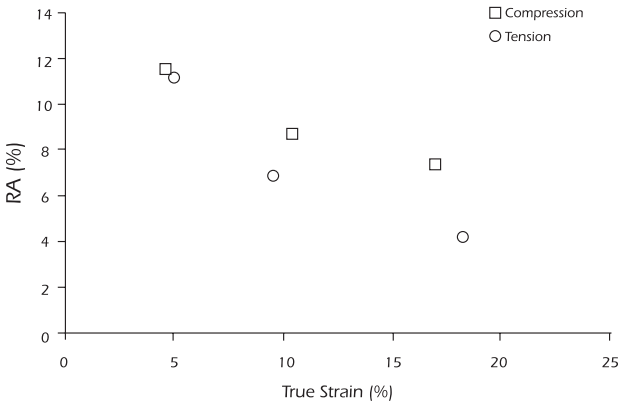


***Fig. 1*** *The variation of the retained austenite with strain under tension and compression loading conditions.*

## References

[1] Wael Dabboussi, Jinbo Qu, James Nemes, Stephen Yue. Experimental Characterization of the Strain Rate and Stress State Effects on a TRIP Assisted Multiphase Steel. SAE World Congress & Exhibition, Detroit, MI, USA, April 2007. SAE 2007 Transactions: Journal of Materials and Manufacturing.

# Neutron Powder Diffraction of Irradiated Low-Enriched U-Mo-Al Dispersion Fuel

**K. Conlon [1], D. Sears [1], R. Donaberger [2], R.B. Rogge [2]**

[1] AECL Chalk River Laboratories, Chalk River, ON, Canada K0J 1J0

[2] Canadian Neutron Beam Centre, National Research Council, Chalk River Laboratories, Chalk River, ON, Canada K0J 1J0

Atomic Energy of Canada Ltd. (AECL) is developing low-enriched (LEU < 20 % $^{235}U$) Al-UMo dispersion fuel for potential use in test reactors. Significant efforts are currently underway around the world to develop this fuel for materials test reactors. The main reasons are that the uranium loadings can be higher than in the presently qualified dispersion fuel, and that spent UMo dispersion fuel is suitable for reprocessing.

Post-Irradiation Examinations (PIE) of irradiated fuel specimens performed at AECL and elsewhere show evidence of a significant chemical reaction between the UMo particles and the Al matrix. At low burnup, the contribution of fission product formation to the swelling behaviour is negligible, and thus swelling behaviour is attributed to chemical interaction of U-Mo-Al and the subsequent formation of low-density reaction product(s), with inter-diffusion enhanced by irradiation. Neutron Diffraction Analysis of the results obtained from an UMo fuel core irradiated to 20 atom % burnup identified the predominant crystalline reaction product as isomorphous with $UAl_3$ [1]. At 60 atom % burnup, the reaction products are predominantly isomorphs with $UAl_x$ compounds (x = 2,3). A comparison of the NDA data obtained from UMo fuels at lower burnup (20 atom %) [1], suggested that (U,Mo) $Al_3$ decomposes to form (U,Mo)$Al_2$. There is also evidence of transformation of the UMo particles into α-U and δ $U_2Mo$, and the formation of small quantities of $UMo_2Al_{20}$ [1].

Recently, new neutron diffraction results show that both crystalline and non-crystalline phases form at different regions within the same fuel element, depending on the local operating conditions within the fuel core. The extent of the reaction and the structure of the reaction product is clearly influenced by the local fuel operating temperature, as evidenced by differences in the morphology of the reaction products observable optically in the region the of fuel near the end-plug region (Figure 1). Specifically, the fuel core in the annular region exhibits intact UMo particles, residual aluminium and an interaction product at the particle-matrix interface, while the fuel core towards the mid-plane exhibits a fully reacted microstructure and a total absence of residual aluminium. Neutron diffraction results obtained from the annular region do not show any significant crystalline phases, despite clear evidence of a reaction product (Figure 1). This suggests that the phase is amorphous.

A finite element model of the fuel element is being developed to assess the temperature field within the fuel element and to provide a reasonable estimate of the recrystallization temperature of the reaction product.

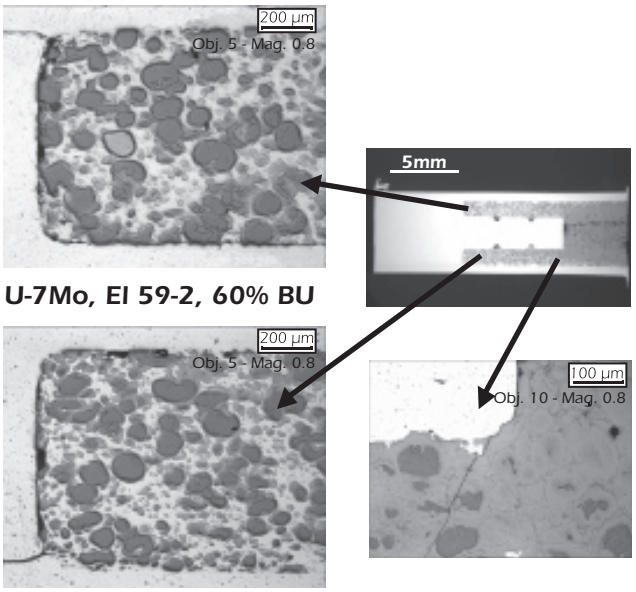


**Fig. 1** Morphology of Irradiated Al-UMo fuel core following 60 atom % burnup. Fuel core in the annular region (at left) exhibits intact UMo particles, residual aluminium and an interaction product at the particle-matrix interface. The fuel core towards the midplane (at right) exhibits a fully reacted microstructure, an absence of residual aluminium and an absence of residual UMo fuel particles.

### References

[1] K. Conlon and D. Sears (2006). Neutron Powder Diffraction of Irradiated Low Enriched Uranium-Molybdenum Dispersion Fuel. 10th Topical Meeting on Research Reactor Fuel Management (European Nuclear Society), Sofia, Bulgaria.

[2] K. Conlon and D.F. Sears, (2007). Neutron Powder Diffraction of UMo Fuel Irradiated to 60 Percent Burnup. 11th Topical Meeting on Research Reactor Fuel Management (European Nuclear Society), Lyon France.

# Crystal Structure and Long Range Magnetic Order in the Novel Rock Salt Structure Type Ruthenate: $Li_3Mg_2RuO_6$

**S. Derakhshan [1], J.E. Greedan [1], T. Katsumata [1], L.M.D. Cranswick [2]**

[1] Brokhouse Institute for Materials Research and Chemistry Department, McMaster University, Hamilton, ON, Canada, L8S 4M1

[2] Canadian Neutron Beam Centre, National Research Council, Chalk River Laboratories, Chalk River, ON, Canada K0J 1J0

Antiferromagnetic (AFM) compounds, which comprise triangular cationic sub-lattices, have the potential to exhibit geometric magnetic frustration [1]. Within the family of ordered sodium chloride type transition metal oxides, a number of compositions and structures present triangle-based topologies and therefore are they very attractive for they study of geometric magnetic frustration.

*4d* and *5d* ions have more extended *d* orbitals relative to the *3d* compounds and they also exhibit a broader range of oxidation states, especially ≥ +5. The large difference in formal charge between the magnetic cations on one hand and the nonmagnetic alkali and alkali earth cations on the other hand is the driving force towards crystallographic cation ordering in such systems. This allows precise design of the magnetic exchange pathways and interactions.

The title compound, which is iso-structural with $Li_3Mg_2NbO_6$ [2], was synthesized via solid state reaction and the phase purity was examined by the XRD method, employing a Guinier-Hägg camera with Cu $K\alpha_1$ radiation and Si as an internal standard. The magnetic susceptibility as well as the heat capacity data reveals that there is a long range AFM order below 17 K.

Variable temperature powder neutron diffraction measurements were performed on the C2 diffractometer at the Canadian Neutron Beam Centre at Chalk River, Ontario. The room temperature data were collected using two different wavelengths of 1.3307 Å and 2.3724 Å. Low temperature data collections (4, 6, 8, 10, 12, 14, 16, 17, 18 K) were carried out for investigation of the ordering temperature and the magnetic structure. For this purpose the long wavelength, 2.37197 Å in the range $4° \leq 2\theta \leq 84°$ with 0.1° intervals was utilized.

Rietveld refinements, using the GSAS program [3,4], on the room temperature neutron diffraction data sets were performed to verify the crystal structure. The structural model was initially taken from that proposed for $Li_3Mg_2NbO_6$. A pseudo-Voigt peak shape profile was chosen and the parameters were refined to obtain the best fit to the experimental data. The overall residual factors of Rp = 0.0306, wRp = 0.0384 and $\chi^2$ = 3.2 are rather low, which indicate a good quality refinement.

$Li_3Mg_2RuO_6$ crystallizes in the orthorhombic *Fddd* space group in an ordered rock salt structure type. The dimensions are: *a* = 5.8759 (2) Å, *b* = 8.4206 (1) Å and *c* = 17.6455 (5) Å. The structure is composed of edge-shared octahedra with eight formula units per unit cell (Figure 1).

There are four independent cationic positions in the unit cell. The oxidation state and size of the $Ru^{5+}$ cations are significantly different from the other cations (Li+ = 0.76 Å, $Mg^{2+}$ = 0.72 Å and $Ru^{5+}$ = 0.565 Å) [5] and therefore they tend to reside in separate crystallographic positions. However, Li and Mg occupy the other three cationic sites with different fractions, M1 being magnesium rich while M2 and M3 are lithium rich sites. When the thermal displacement factors of M2 and M3 sites were refined together, divergence occurred. To stabilize the refinement, their $U_{iso}$ values were constrained to a reasonable value, 0.015. This is due to the very small total scattering length in these sites. In fact, the scattering lengths of Li and Mg have opposite signs, $b_{Li}$ = -1.900 and $b_{Mg}$ = 5.375, and the Li:Mg occupancy ratio being close to 4:1 results in a small total negative scattering length, approximately -0.45. The crystallographic details and the atomic positions are summarized in Tables 1 and 2, respectively.

Low temperature neutron diffraction data were collected to probe the magnetic structure as shown in Figure 2. There are at least five additional peaks in the low temperature data that correspond to the magnetic structure. Subtracting the 18 K data from those of the 4 K their positions are identified as shown in Figure 2. They clearly disappear by 18 K, Figure 3, consistent with both the susceptibility and specific heat data. The two major peaks were indexed using a LeBail approach which required a magnetic cell of dimensions 2a × 2b × 3c relative to the chemical cell, giving indices (½ 1 ⅓) and (½ ½ 2). Thus, the magnetic cell is 12 × the volume of the chemical cell and involves 8 × 12 = 96 Ru spins. Attempts to solve the magnetic structure are on-going but this is clearly a difficult and highly underdetermined problem. While the details of the magnetic structure are not known in detail, the large dimensions of the magnetic unit cell are consistent with a high level of frustration in three dimensions. As well, the symmetric shape of the magnetic diffuse scattering at 18 K, seen clearly in Figure 3, is not consistent with short range 2D magnetic correlations for which the highly asymmetric "Warren" line shape is expected.

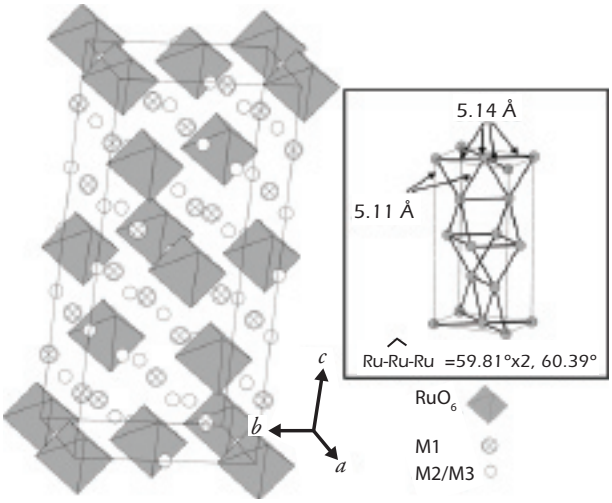


**Fig. 1** The crystal structure of $Li_3MgRuO_6$. The grey octahedra represent $[RuO_6]^{7-}$ the crossed circles are magnesium rich (M1) positions and small empty circles are Li rich (M2 and M3) positions. The Ru—Ru distances and Ru—Ru—Ru angles are presented in the inset.

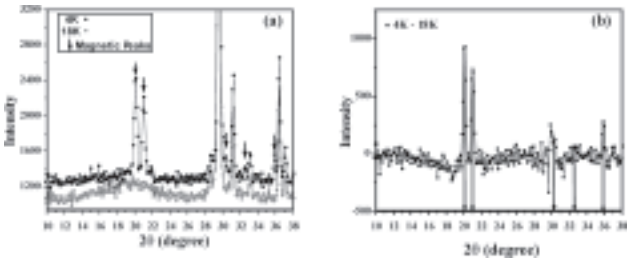


**Fig. 3 (a)** Comparison between diffraction patterns at 4 K and 18 K. (b) The magnetic peaks obtained by subtracting the 18 K data from 4 K data.

| | *a* (Å) | *b* (Å) | *c* (Å) | *Rp* | *wRp* | *z* |
|---|---|---|---|---|---|---|

**Table 1.** Some selected structural parameters of Li3Mg2RuO6.

| | *x* | *y* | z | *Occ. Li/ Mg* | $U_{iso}$ (Å$^2$) |
|---|---|---|---|---|---|
| Ru | 0.125 | 0.125 | 0.125 | | 0.007(1) |
| M1 | 0.125 | 0.125 | 0.2939(4) | 0.33(1)/ 0.67 | 0.005(2) |
| M2 | 0.125 | 0.625 | 0.299(4) | 0.78(1)/ 0.22 | 0.015 |
| M3 | 0.125 | 0.625 | 0.125 | 0.82(1)/ 0.18 | 0.015 |
| O1 | 0.125 | 0.3576(4) | 0.125 | | 0.007(1) |
| O2 | 0.1114(3) | 0.3747(3) | 0.2961(2) | | 0.0069(6) |

**Table 2.** Atomic coordinates, occupancy factors and equivalent isotropic displacement parameters for $Li_{3.06(1)}Mg_{1.94}RuO_6$.

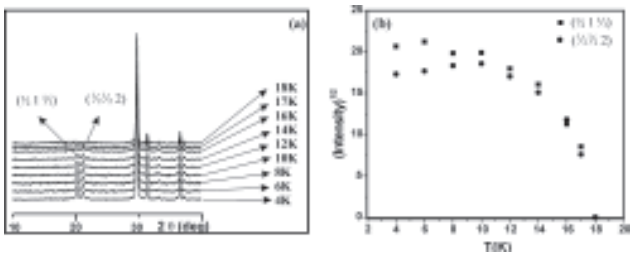


**Fig. 2 (a)** Low temperature powder neutron diffraction data. (b) Integrated area for magnetic peaks as a function of the temperature.

### References


[1] Greedan, J. E. J. Mater. Chem. 2001, 11, 37.

[2] Mather, G. C.; Smith, R. I.; Skakle, J. M.S.; Fletcher, J. G.; Castellanos, M. A.; Pilar Gutierrez, M.; West, A. R.; J. Mater. Chem., 1995, 5, 1177.

[3] Larson A. C, Von Dreele R. B, General Structure Analysis System (GSAS), Los Alamos National Laboratory Report LAUR 2000, 86.

[4] Toby B. H; J. Appl. Cryst. 2001, 34, 210.

[5] Shannon, R. D.; Acta Cryst. A, 1976, 32, 751.

# Magnetic Properties of Geometrically Frustrated Double Perovskites, $Ba_2YRuO_6$, $Ba_2YMoO_6$ and $La_2LiReO_6$

**T. Aharen [1], J. E. Greedan [1], and L.M.D. Cranswick [2]**

[1] Department of Chemistry, McMaster University, Hamilton, ON, Canada L8S 4M1.

[2] Canadian Neutron Beam Centre, National Research Council, Chalk River Laboratories, Chalk River, ON, Canada K0J 1J0

We have carried out neutron diffraction measurements on $La_2LiReO_6$, $Ba_2YMoO_6$ and $Ba_2YRuO_6$ using the C2 powder diffractometer at the Canadian Neutron Beam Centre. We expected that no magnetic peaks would appear in the first two compounds, since there were no signatures of long range ordering according to magnetic susceptibility measurements. On the other hand, $Ba_2YRuO_6$ was expected to show some feature of antiferromagnetic long range ordering since the heat capacity data shows a very sharp λ-type peak around 37 K, which is consistent with magnetic susceptibility results.

$Ba_2YRuO_6$ crystallizes in the cubic space group Fm-3m [1]. The refinement for the crystal structure with the data collected using longer neutron wavelength and FULLPROF program [2] was done and the cell constant is determined to be 8.332(1) Å at room temperature and 8.3194(7) Å at 2.7 K. R-factors in the refinements for each temperature are; $R_p$ = 4.90, $R_{wp}$= 6.45 for room temperature, and $R_p$= 4.54, $R_{wp}$= 6.88, magnetic R-factor = 20.5 for 2.7 K. These factors are reasonably low, meaning these are good refinements.

The magnetic susceptibility results collected at McMaster University using SQUID magnetometer (Quantum Design) show two shoulder-like peaks at 47 K and 37 K for this compound, which may be the transition temperatures, and the Curie-Weiss constant is calculated to be θ = -522 K. However the heat capacity measurement shows a λ-type peak around 37 K only. This could be explained as antiferromagnetic short range ordering occurring first around 47 K, following by the formation of complete antiferromagnetic long range ordering at 37 K.

The evolution of magnetic peaks in the diffraction patterns of $Ba_2YRuO_6$ is shown in Figure 1. As one can see, two magnetic peaks appear around 2θ = 16° and 23° below about 35 K. The magnetic structure was also refined and the two magnetic peaks at 2θ = 16° and 23° could be indexed as k = (0, 0, 1), and (1, 1, 0), respectively. According to this result, the actual transition temperature of $Ba_2YRuO_6$ is determined to be 37 K. The magnetic structure of this compound was confirmed to be face-centered cubic and Type I structure, which was reported by Battle *et al.* [1].

As well as $Ba_2YRuO_6$, $Ba_2YMoO_6$ also crystallizes into the same cubic symmetry (space group Fm-3m) [3]. Since the magnetic susceptibility result shows the lack of long range ordering in the temperature region from 300 K to 2 K and Curie-Weiss constant was determined to be θ = -394 K, there should not be any new magnetic peaks appearing. This result was confirmed based on the comparison of diffraction patterns collected using longer neutron wavelength (2.37Å) at 2.7 K and room temperatures. The absence of antiferromagnetic long range ordering also agreed with the result of heat capacity collected at McMaster University. The crystal structures at 298 K and 2.7 K were refined and determined to have a cubic structure with cell constants, 8.3904(5) Å and 8.3784(5) Å, respectively. R factors are: $R_p$= 4.87, $R_{wp}$= 6.36 and $\chi^2$ = 2.87. Since the $Mo^{5+}$ ion has $d^1$ electronic structure, it could result in Jahn-Teller distortion and transform to a lower symmetry. However, the refinement with cubic symmetry shows good agreement and it is reasonable to say that $Ba_2YMoO_6$ remains cubic structure at 2.7 K.

We also have performed neutron diffraction measurements on the compound, $La_2LiReO_6$. The structure is monoclinic with space group $P2_1/n$. The magnetic susceptibility result shows a ZFC/FC divergence around 50 K, a broad maximum in the ZFC curve at 33 K and the Weiss temperature is θ=-163 K. Therefore, antiferromagnetic interaction exists. However, the heat capacity data did not show any peaks or shoulders. Thus, there are not any features indicating the presence of antiferromagnetic long or short range ordering. The comparison of two diffraction patterns collected at room and base temperatures supports the absence of antiferromagnetic long range ordering. Crystal structure refinement with the data collected at 298 K determined the structure parameters to be a = 5.5819(6) Å, b = 5.6743(6) Å, c = 7.8840(8) Å, β = 90.243° and total cell volume is 249.7117 $Å^3$. R factors are: $R_p$ = 3.39, $R_{wp}$ = 4.47 and $\chi^2$ = 3.01. The structure refinement was also done with the data collected at 2.8 K and determined the cell parameters to be a = 5.5801(6) Å, b = 5.6859(6) Å, c = 7.8421(9) Å, β = 90.479° and total cell volume is 248.8079$Å^3$. R factors are: $R_p$ = 4.17, $R_{wp}$ = 5.72 and $\chi^2$ = 6.10.

In summary, the neutron diffraction experiment confirmed the presence of antiferromagnetic long range ordering and revealed the transition temperature in $Ba_2YRuO_6$ and the absence of long range ordering with $Ba_2YMoO_6$ and $La_2LiReO_6$ is confirmed, as expected.

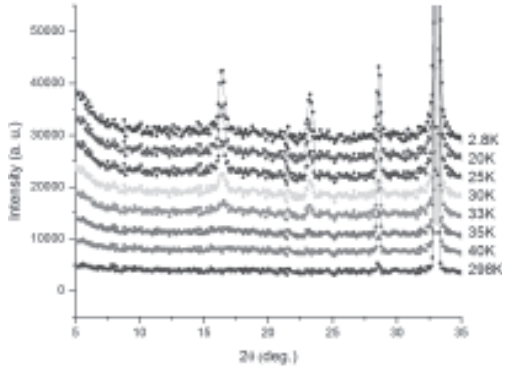


**Fig. 1** Evolution of magnetic peaks of $Ba_2YRuO_6$

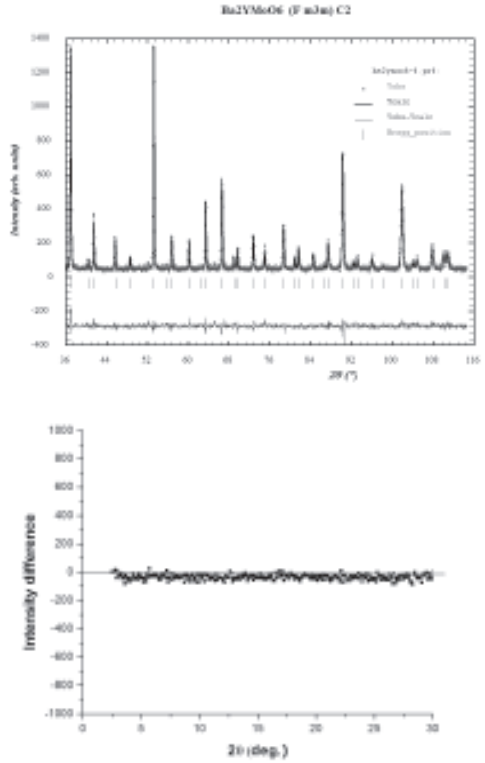


**Fig. 2** Crystal structure refinement of $Ba_2YMoO_6$ at 2.7 K (upper) and the intensity difference of the diffraction patterns at 2.7 K and 298 K (lower). There is no difference between two patterns.

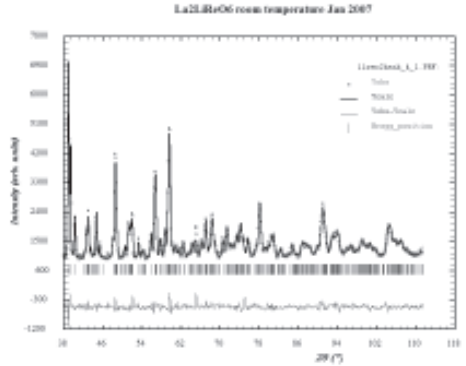

**Fig. 3** Crystal structure refinement for $La_2LiReO_6$ (298 K)

## References


[1] P.D. Battle et al, J. Solid State Chem.,78, 108 (1989)

[2] J. Rodriguez-Carvajal, Physica B, 192, 55 (1993)

[3] E. D. Cussen et al, Chem. Mater., 18, 2855 (2006)

# Investigation of the Magnetic Structure of FeCrAs

**W. Wu [1], A. McCollam [1], S. Julian [1], and I. Swainson [2]**

[1] Physics Department, University of Toronto, Toronto, ON, Canada M5S 1A7

[2] Canadian Neutron Beam Centre, National Research Council, Chalk River Laboratories, Chalk River, ON, Canada K0J 1J0

Ternary-metal arsenides with formula *MM'*As (*M, M'* = Cr, Mn, Fe, Co, Ni) usually show ferromagnetic or antiferromagnetic magnetic ordering below their corresponding critical temperatures. However, it was reported that FeCrAs is still paramagnetic at 4.2 K [1]. This compound has a $Fe_2P$-type crystal structure: hexagonal $P\bar{6}2m$ [2]. The space group ($P\bar{6}2m$) of this crystal and lattice parameters (a = 6.096 Å, c = 3.651 Å) of the unit cell were determined by R. Fruchart and L. Hollans et al. [2, 3]. Within this structure, there are two different types of atomic sites for metal atoms, *Mtet* and *Mpry*, with *Mtet* sites forming a corner-sharing triangular lattice. Mossbauer spectroscopy measurements showed that there is no magnetic ordering on the Fe atoms down to 4.2 K [1]. We postulated possible frustration as a cause of this lack of ordering.

Therefore neutron powder diffraction was undertaken to investigate possible frustration. We found that the two transition metals were strongly ordered over the two sites. Furthermore we found that in place of a lack of magnetic order, we found strong magnetic peaks which were indexed to a propagation vector of **k** = (1/3, 1/3, 0) corresponding to the K-point on the Brillouin Zone.

The peak at about 70° appears to be from an impurity phase. The best fit from a single basis function (BF) of the Cr atoms is $\psi_6$ of $\Gamma_6$. However, it doesn't appear to be a perfect description. Linear combinations of the BFs of $\Gamma_6$ are also allowed. The site symmetry of Fe is the same as that of Cr, so the BFs are common across the two sites. Therefore, we are investigating whether a very small contribution to the magnetic scattering from Fe may be at play, although this would contradict the Mossbauer study [1].

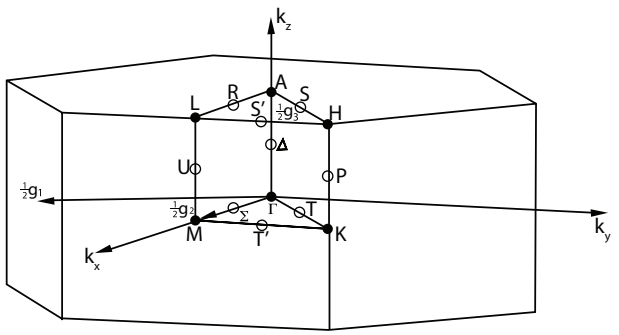


**Fig. 1** Brillouin Zone of the hexagonal primitive lattice.

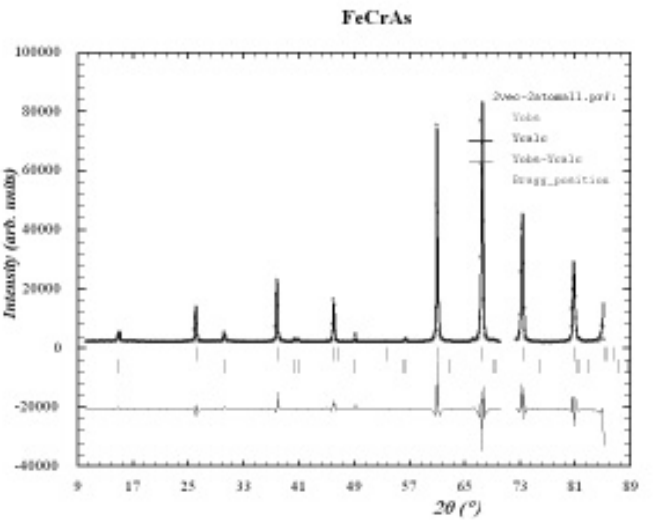


**Fig. 2** Fit to the observed neutron data, assuming only Cr moments. Lower tic marks are magnetic diffraction assuming $\Gamma_6\Psi_6$ (Table 3). Upper tic marks are the nuclear lattice, which has highly ordered Fe, Cr across the two sites.

| IR | BV | Atom | BV components | | | | | |
|---|---|---|---|---|---|---|---|---|
| | | | $m\|\|_a$ | $m\|\|_b$ | $m\|\|_c$ | $im\|\|_a$ | $im\|\|_b$ | $im\|\|_c$ |
| $\Gamma_2$ | $\psi_1$ | 1 | 4 | 0 | 0 | 0 | 0 | 0 |
| | | 2 | 0 | 4 | 0 | 0 | 0 | 0 |
| | | 3 | 2 | 2 | 0 | 3.464 | 3.464 | 0 |
| $\Gamma_3$ | $\psi_2$ | 1 | 0 | 0 | 4 | 0 | 0 | 0 |
| | | 2 | 0 | 0 | 4 | 0 | 0 | 0 |
| | | 3 | 0 | 0 | -2 | 0 | 0 | -3.464 |
| $\Gamma_4$ | $\psi_3$ | 1 | 2 | 4 | 0 | 0 | 0 | 0 |
| | | 2 | -4 | -2 | 0 | 0 | 0 | 0 |
| | | 3 | -1 | 1 | 0 | -1.732 | 1.732 | 0 |
| $\Gamma_5$ | $\psi_4$ | 1 | 0 | 0 | 4 | 0 | 0 | 0 |
| | | 2 | 0 | 0 | -2 | 0 | 0 | 0 |
| | | 3 | 0 | 0 | 1 | 0 | 0 | 1.732 |
| | $\psi_5$ | 1 | 0 | 0 | 0 | 0 | 0 | 0 |
| | | 2 | 0 | 0 | -3.464 | 0 | 0 | 0 |
| | | 3 | 0 | 0 | -1.732 | 0 | 0 | -3 |
| $\Gamma_6$ | $\psi_6$ | 1 | 4 | 0 | 0 | 0 | 0 | 0 |
| | | 2 | 0 | -2 | 0 | 0 | 0 | 0 |
| | | 3 | -1 | -1 | 0 | -1.732 | -1.732 | 0 |
| | $\psi_7$ | 1 | 0 | 2 | 0 | 0 | 0 | 0 |
| | | 2 | 1 | 1 | 0 | 1.732 | -1.732 | 0 |
| | | 3 | 2 | 0 | 0 | 0 | 0 | 0 |
| | $\psi_8$ | 1 | 0 | 0 | 0 | 0 | 0 | 0 |
| | | 2 | 0 | -3.464 | 0 | 0 | 0 | 0 |
| | | 3 | 1.732 | 1.732 | 0 | 3 | 3 | 0 |
| | $\psi_9$ | 1 | 1 | 1 | 0 | -1.732 | -1.732 | 0 |
| | | 2 | -1 | 0 | 0 | -1.732 | 0 | 0 |
| | | 3 | 0 | -1 | 0 | 0 | -1.732 | 0 |

Table 1: Basis vectors for the space group P -6 2 m with $\mathbf{k}_{13}$ = (.33333, .33333, 0). The decomposition of the magnetic representation *Fe* site (.60579, 0, .5) is $\Gamma_{Mag} = 0\Gamma_1 + 1\Gamma_2 + 1\Gamma_3 + 1\Gamma_4 + 1\Gamma_5 + 2\Gamma_6$. The atoms of the nonprimitive basis are defined according to 1: (.60579, 0, .5), 2: (0, .60570, .5), 3: (.39421, .39421, .5).

***Fig. 3*** *Table of allowed basis vectors for the Cr sublattice.*

## References


[1] D.G. Rancourt, Thesis: Hyperfine Field Fluctuations in the Mossbauer Spectrum of Magnetic Materials: Application to Small Particles and to the Bulk Antiferromagnet $Fe_{(2-x)}Cr_{(x)}As$ (1984).

[2] R. Fruchart, Ann. Chim. 7, 563 (1982).

[3] L. Hollan, P. Lecocq, C. R. Acad. Sc. Paris, t. (260) (21), 6616 (1965).

# Crystal and Magnetic Structure of Potentially Multi-Ferroic $PbFeO_3$

**J.E. Greedan [1], T. Katsumata [2], T. Tsuchiya [2], Y. Inaguma [2] and S. Derakhshan [1]**

[1] Brockhouse Institute for Materials Research and Department of Chemistry, McMaster University, Hamilton, ON, Canada L8S 4M1

[2] Chemistry Department, Gakushuin University, 1-5-1 Mejiro, Toshima-ku, Tokyo, Japan 172-8588

Multi-ferroics are materials that exhibit spontaneous electric and magnetic polarizations simultaneously. In the search for new multi-ferroic compounds, a popular strategy is to modify known ferroelectric materials by substitutions that introduce magnetic ions. For example,

$PbTiO_3$ is a well-known ferroelectric but is diamagnetic. Substitution of Ti with Fe will introduce magnetic properties. $PbFeO_3$ can be prepared only at high pressure (6 – 7 GPa) and temperature (1275 – 1575 K) in an anvil apparatus [1]. XPS data indicate that $Pb^{2+}$, $Pb^{4+}$ and $Fe^{3+}$ are present in this material. X-ray powder data are consistent with an orthorhombic pseudo cubic sub-cell with ac ~ 3.90 Å, but a complex supercell of $6a_c$ x $2a_c$ x $2a_c$ was found from electron diffraction. It was the goal of this study to determine the critical temperature for magnetic order and, if possible, the crystal and magnetic structures. The sample size was only ~ 700 mg. Data were taken from 2.8 K to 610 K. For measurements above room temperature, the sample was contained in a quartz tube backfilled with ~ 1 atm of oxygen as the sample is known to decompose above 720K in air. To search for magnetic reflections, the difference plot 296 K – 610 K was constructed as shown in Figure 1. Three magnetic reflections are marked with an asterix (*) at 2θ = 30.484(3)°, 59.89(1)° and 60.921(8)°. These can be indexed on the primitive orthorhombic cell as (1/2 1/2 1/2), (3/2 1/2 1/2) and (1/2 1/2 3/2) which indicates a G-type antiferromagnetic structure as was found for the related material, $PbFeO_2F$ [2]. The temperature dependence of the strongest magnetic peak (2θ = 30.48°) is shown in the inset which indicates $T_c$ = 605(3) K for this material. Attempts to refine the crystal and magnetic structures are underway.

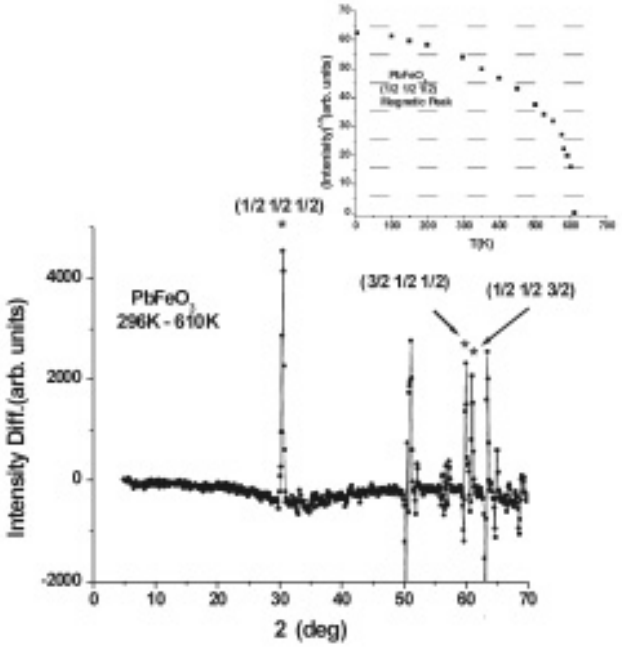


**Fig. 1** The difference plot 296 K – 610 K for $PbFeO_3$. Magnetic reflections are marked with an asterix (*). The temperature dependence of the strongest magnetic peak at 30.48 deg ,(1/2 1/2 1/2), is shown in the inset which indicates $T_c$ = 605(3) K.

## References

[1] Takeshi Tsuchiya, Hiroyuki Saito, Masashi Yoshida, Tetsuhiro Katsumata, Tomonori Ohba, Yoshiyuki Inaguma, Takao Tsurui, and Masahiro Shikano, Mater. Res. Soc. Symp. Proc. Vol. 988 (2007) 0988-QQ09-16.

[2] Tetsuhiro Katsumata, Akihiro Takase, Masashi Yoshida, Yoshiyuki Inaguma, John E. Greedan, Jacques Barbier, Lachlan M. D. Cranswick, and Mario Bieringer, Mater. Res. Soc. Symp. Proc. Vol. 988 (2007) 0988-QQ06-03.

# Crystal and Magnetic Structures of the Pillared Perovskites, $La_5Re_2TiMO_{16}$ (M = Mn, Fe, Co, Ni, Mg)

**H.L. Cuthbert [1], J.E. Greedan [1], and I. Swainson [2]**

[1] Department of Chemistry and Brockhouse Institute for Materials Research, McMaster University, Hamilton, ON, Canada, L8S 4M1

[2] Canadian Neutron Beam Centre, National Research Council, Chalk River Laboratories, Chalk River, ON, Canada K0J 1J0

Recently, an attempt was made to synthesize and study a new family of pillared perovskites. The general formula would be $La_5Re_2TiMO_{16}$, where $M$ is a $2^+$ transition metal ion (such as Mn, Fe, Co, Ni or Mg). The target structure consists of perovskite-like layers of corner-sharing $Ti^{4+}M^{2+}O_6$ octahedra, "pillared" by dimers of edge-shared $Re^{5.5+}O_6$ octahedra. Thus the dimer "pillars" would contain one unpaired electron, making them paramagnetic. The dimers connect to the $M^{2+}$ sites in the perovskite layers only. By varying the $M^{2+}$ ion from Mn ($S$ = 5/2) to Mg ($S$ = 0), the effect of the spin quantum number on the resulting magnetism of these low-dimensional compounds could be studied.

SQUID magnetometry measurements have revealed some similarities between the compounds. They all have broad features, indicative of short-range order. There is a feature that could signify long-range order at approximately 160 K, 35 K and 14 K in the Mn, Co and Ni members respectively, which is similar to the $La_5Re_3MO_{16}$ (Mn, Co, Ni) analogues previously studied [1,2,3]. The Mg member did not show any features indicative of magnetic ordering down to 2 K.

Powder neutron diffraction measurements on the C2 diffractometer at the Canadian Neutron Beam Centre in Chalk River were collected to determine the crystal structure of these compounds. Unfortunately, the samples were not very crystalline, and did not diffract well. However, these measurements did show that the samples contained significant amounts of other secondary phases that could not be identified and were difficult to detect using X-ray diffraction. Collecting low temperature data (at 3.8 K) on the samples, however, revealed some surprising results. Only the Mn member showed any evidence of new reflections. There is no evidence of any enhanced or new reflections in any other sample.

The two Mn patterns, collected at room temperature and 3.8 K, along with a difference plot are pictured in Figure 1. Some artifacts appear in the difference plot due to peak broadening at low temperature. The new peaks can be indexed to a magnetic unit cell with ordering vector, **k** = (0,0,1/2). This is similar to the structure found for $La_5Re_3MnO_{16}$, which consists of ferromagnetic intra-layer coupling between the $Re^{5+}$ ($S$ = 1) and $Mn^{2+}$ ($S$ = 5/2) moments, and antiferromagnetic coupling of the layers through the diamagnetic pillar [1]. It was expected that through substitution of $Re^{5+}$ within the layer by $Ti^{4+}$, an extra unpaired electron would reside on the $Re_2O_{10}$ pillar and cause significant changes in the resulting magnetism (i.e. if antiferromagnetic coupling along the $c$-axis is preferred, then to satisfy both layers and the dimer, the layers would be coupled ferromagnetically with respect to each other). If the substitution were successful, this does not appear to be the case. The three new magnetic reflections are consistent with a magnetic unit cell involving ferromagnetic $Mn^{2+}$ moments within the layers, aligned parallel to the $c$-axis, and antiferromagnetic interlayer coupling. The magnitude and orientation of the dimer moment are unknown and may be too weak to observe. Ferromagnetic intra-layer coupling between the $Mn^{2+}$ ions ($S$ = 5/2) is unexpected, since the Goodenough-Kanamori rules for magnetic superexchange [4,5] predict antiferromagnetic interactions. A second interpretation is that Ti substitution did not occur and that the magnetic properties studied are actually those of $La_5Re_3MnO_{16}$. As a result, further analysis to determine whether Ti substitution did indeed occur is currently underway. In addition, the synthesis of samples with improved crystallinity and phase purity is also being attempted.

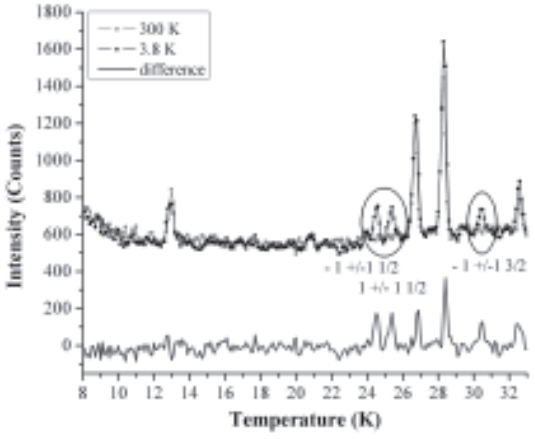


**Fig. 1** Powder neutron diffraction patterns of $La_5Re_2TiMnO_{16}$ taken at room temperature (gray) and 3.8 K (black). The difference map appears below, and the magnetic reflections have been circled and indexed.

## References

[1] Green, A.E.C.; Wiebe, C.R.; Greedan, J.E. Solid State Sciences. 2002, 4, 305-310.

[2] Chi, L.; Green, A.E.C.; Hammond, R.; Wiebe, C.R.; Greedan, J.E. J. Solid State Chem. 2003, 170, 165-175.

[3] Cuthbert, H.L.; Greedan, J.E.; Cranswick, L. J. Solid State Chem. 2006, 179, 1938-1947.

[4] Goodenough, J.B.; Magnetism and the Chemical Bond. Wiley: New York, 1963.

[5] Kanamori, J. J. Chem. Phys. Solids 1959, 10, 87-98.

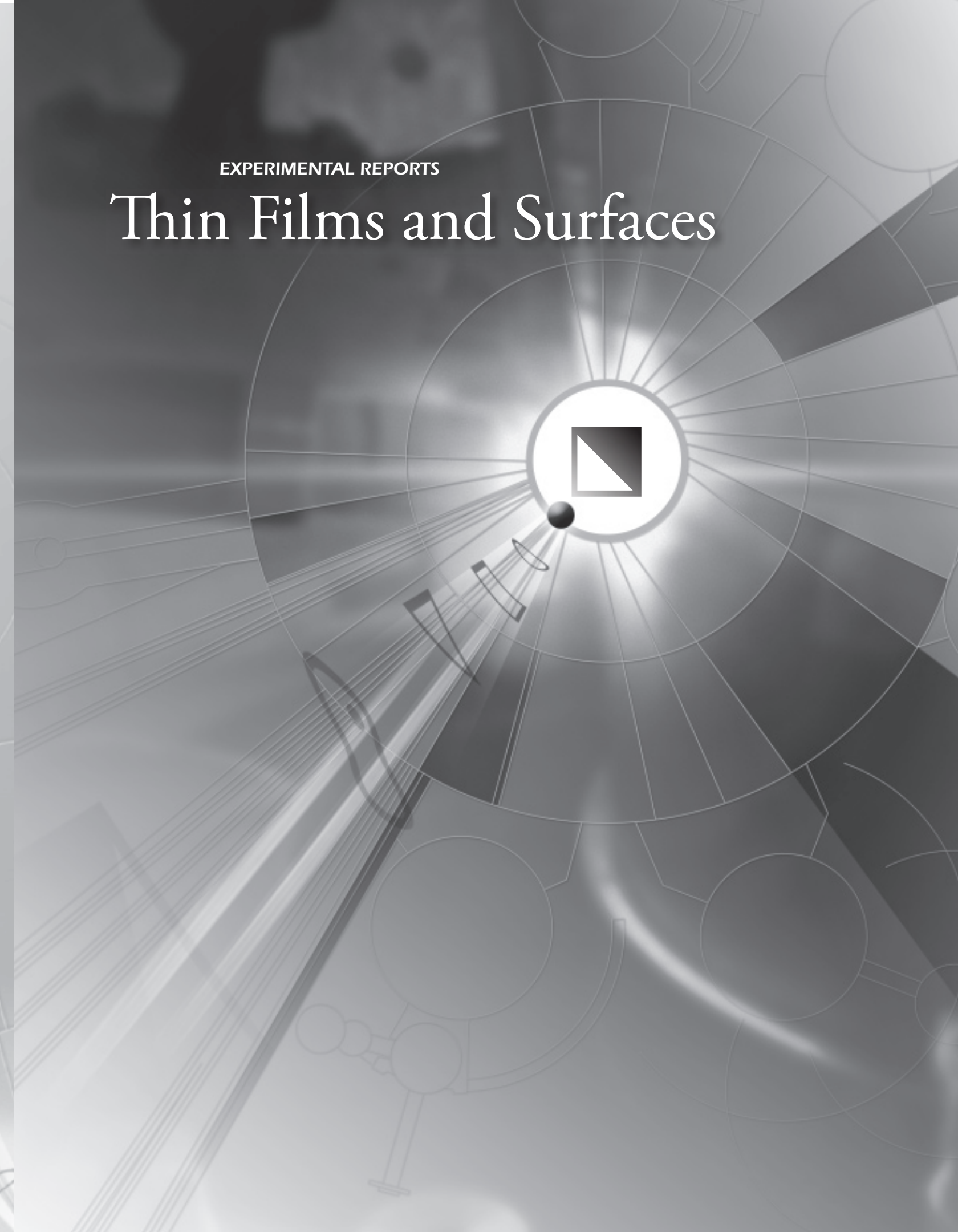

EXPERIMENTAL REPORTS

# Thin Films and Surfaces

# Morphology of Comb-Shaped Proton Exchange Membrane (PEM) Copolymers Based on a Neutron Scattering Study

**M-P. Nieh [1], M.D. Guiver [2], D.S. Kim [2], J. Ding [2], and T. Norsten [2]**

[1] Canadian Neutron Beam Centre, National Research Council, Chalk River Laboratories, Chalk River, ON, Canada K0J 1J0

[2] Institute for Chemical Process and Environmental Technology, National Research Council Canada, Ottawa, ON, Canada K1A 0R6

Proton exchange membrane (PEM) is a semi-permeable membrane that is designed to conduct protons but is impermeable to gases such as hydrogen and oxygen. For the application to fuel cells, PEM serves an important function to separate reactants and transport protons. Ideal PEM materials should possess properties such as high proton conductivity, high chemical stability over the required temperature range, good mechanical properties and dimensional stability in the hydrated state. Block copolymers forming hydrophobic and interconnected hydrophilic (ionic) domains have many of the aforementioned properties. The hydrophobic matrix provides the mechanical strength and constrains the swelling of the materials, while the hydrophilic (ionic) domains determine the proton conductivity. In order to better design polymer architectures and improve performance of PEM materials, it is essential to resolve their morphologies. In the past, small angle neutron scattering (SANS), X-ray scattering (SAXS) and wide angle X-ray scattering (WAXS) have been powerful tools for structural characterization of PEMs.

Recently, a comb-shaped copolymer has been developed based on a highly fluorinated and rigid polyaromatic backbone containing monodisperse α-methyl polystyrene sulfonic acid side-chains (Figure 1) [1]. The comb-shaped copolymer PEMs exhibit very low hydration-based dimensional changes at elevated operating temperatures with similar proton conductivity and water uptake values compared to the bench-marked PEM, Nafion. We have studied the structures of two comb-shaped copolymers: PEM-19 (19 wt.% side chain content) and PEM-32 (32 wt.% side chain content), which represent the extremes of a low and high ion exchange capacities, having proton conductivities lower (19 wt.%) and higher (32 wt.%) than Nafion, respectively. In this study, we used the following two SANS instruments: NG3 at the National Institute of Standards and Technology (NIST) and E3 at the Canadian Neutron Beam Centre (CNBC).

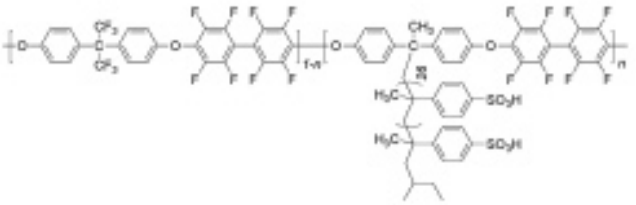

**Fig. 1** Molecular structure of comb-shaped copolymer.

The SANS results of $D_2O$-soaked PEM-19 and PEM-32 as shown in Figure 2, illustrate a similar scattering pattern, presumably resulting from the same morphology. The general feature of both curves is a gradual decay of the intensity over the whole q range with a strong and broad peak at $q$ = 0.03 ~ 0.04 Å$^{-1}$ and a shoulder at $q$ = 0.06 ~ 0.08 Å$^{-1}$, which could be the second order Bragg peak, followed by another broad peak at higher $q$ between 0.2 and 0.25 Å$^{-1}$. Comparing these two curves, the low-$q$ peak shifts outwards, corresponding to a smaller length, and the high-$q$ peak shifts inwards with an increased intensity, corresponding to a larger length, when the sample contains more sulfonic acid groups (i.e., PEM-32). Low-$q$ peaks were also observed in other PEM materials and Nafion in the past and interpreted as a "crystalline peak" [2-6]. As for the high-$q$ peak, it is well known through many SANS and SAXS studies on Nafion that there is an "ionomer peak" located around 0.1 ~ 0.25 Å$^{-1}$, which shifts toward lower $q$ and had an increased intensity at higher hydration levels [1,7-9]. The same trend of shift and intensity and the similar vicinity of the high-$q$ peak observed in our SANS measurement further confirms that it is the "ionomer peak."

Here, we propose an approach to fit the SANS data by focusing on low-$q$ and high-$q$ regimes individually. The scattering intensity in the low $q$ regime is mainly attributed to the crystalline phase composed of large hydrophobic and hydrophilic domains, whereas the high-$q$ scattering mainly comes from the local distribution of the ionomers and water ($D_2O$) in the hydrophilic domain. Therefore, the scattering function, $I(q)$ can be split into two terms as follows:

1). $$I(q) = I_{crystalline}(q) + I_{ionomer}(q)$$

We assume that the density distribution in the hydrophilic domain could more resemble the case of microemulsions considering the mixing of polyions and water. Therefore, $I_{ionomer}(q)$ can be formulated with the Teubner-Strey model (T-S model) [10], which is derived based on Landau's free energy theory and Debye-Anderson-Brumberger's derivation of scattering by inhomogeneous domains [11], with a correlation function, γ(r) (in Equation 2) yielding a scattering function as Equation 3:

2). $$\gamma(r) = \frac{d}{2\pi r} e^{-r/\xi} \sin\left(\frac{2\pi r}{d}\right)$$ , and

3). $$I_{T-S}(q) = \frac{1}{a_2 + c_1 q^2 + c_2 q^4} \quad ,$$

where $a_2$, $c_1$, and $c_2$ are the coefficients of various terms of order parameters in Landau's free energy. In the case of microemulsion, $c_1$ indicates the tendency of forming interfaces between domains and is usually negative, when $a_2$ is positive, to favour the formation of microemulsion. A positive $c_2$ stabilizes the system to meet the criteria of $4a_2c_2 - c_1 > 0$ for a stable morphology.

The T-S scattering function, $I_{T-S}(q)$ describes a morphology of two alternating domains losing long-range order and has a characteristic feature of a low-$q$ plateau with a peak followed by a $q^{-4}$ decay (as shown in Figure 2). Since the intensity of the low-$q$ plateau is simply a flat background for the low-$q$ data, it does not affect the structural parameters of the crystalline phase obtained from the SANS data in this regime. The two length scales, $d$ and $\xi$, in Equation 2 represent the domain periodicity of the system, which is related to spacing of the domains, and the correlation length of the system, which is related to the decay length of the domains, respectively, and can be related with the coefficients at the denominator of $I_{T-S}(q)$ as expressed below [10]:

4). $$\xi = \left[\frac{1}{2}\left(\frac{a_2}{c_2}\right)^{1/2} + \frac{1}{4}\frac{c_1}{c_2}\right]^{-1/2} \quad \text{,and}$$

$$d = 2\pi\left[\frac{1}{2}\left(\frac{a_2}{c_2}\right)^{1/2} - \frac{1}{4}\frac{c_1}{c_2}\right]^{-1/2} \quad ,$$

The application of T-S model does not require the assumption of aggregates with a regular location or shape and size, such as spheres, ellipsoids, disks, cylinders, yet the ratio, $S/V$, of the ionomer-water interfacial area $(S)$ to hydrophilic volume $(V)$, can be still obtained through Porod's law:

5). $$\frac{S}{V} = \frac{4\phi_w^{phil}(1-\phi_w^{phil})}{\xi} \quad ,$$

where $\phi_w^{phil}$ is the volume fraction of water in the hydrophilic domain [10].

Regarding $I_{crystalline}(q)$, to describe the crystalline phase at low-$q$ regime, two different models are employed to fit the SANS data: stacking layered disks (similar to lamellar model with a smaller planar region) and worm-like elongated aggregates with a hard disk structure factor as shown in Figure 3 (see page 86). The best-fit result of stacking layered disks model (the dark grey curve in Figure 2) to the PEM-19 SANS data indicates several mismatching regions compared with the experimental data. First, the fit overestimates the minimum prior to the first order peak and the maximum of the second order peak. Second, the model predicts a sharper decrease after the second order peak. In light of the aforementioned observations, stacking disks may not be the best model to describe the PEM morphology. The other model is the worm-like elongated aggregates model proposed for worm-like micelles is chosen to be the form factor, $F_{WL}(q)$ [12] combining with a hard disk structure factor, $S_{HD}(q)$ to account for the radial interaction among the worm-like cylinders [13]. This is based on the assumption that the radial interparticle interaction among the long aggregates is expected to be much more significant than the axial interaction in the current $q$-range. Therefore, $I_{crystalline}(q)$ can be expressed as

6). $$I_{crystalline}(q) = \Delta\rho^2\phi_{phob}(1-\phi_{phob})\cdot\bar{\upsilon}\cdot S_{HD}(q)F_{WL}(q)$$

where $\Delta\rho$, $\phi_{phob}$, $\bar{\upsilon}$ are the difference of scattering length densities (SLDs) between hydrophilic and hydrophobic domains, the volume fraction of hydrophobic domain and the volume of individual cylindrical aggregates, respectively.

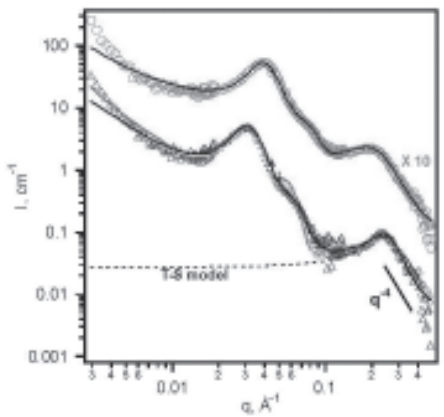


**Fig. 2** SANS data for PEM-19 (triangles) and PEM-32 (circles) with best fits of various low-$q$ models: stacking disks (dark grey), flexible cylinders with a circular cross-section (light grey), flexible ellipsoidal cylinders (black). For better clarity, the data of PEM-32 is shifted by a factor of 10 and only fitted with the flexible ellipsoidal cylinder model. In the high $q$ regime, the best-fitting T-S model to PEM-19 SANS data is shown as the dashed line.

The best-fit (the light grey curve in Figure 2) shows a better agreement with the SANS data at maxima and minima than the stacking disks model, except for the minimum after the second order peak. The mismatch is mainly attributed to the unrealistic constraint on the fixed, circular radius of the hydrophilic domain and can be improved by introducing an ellipsoidal cross-section with an aspect ratio at cross-section (the black curve in Figure 2).

The "rocking" curves of both copolymer films were taken at the low-q crystalline peaks as a function of sample angle,

ψ , where ψ = 0 is defined as neutron beam being parallel with the film surface. Both curves are practically flat with no more than a 20% higher intensity at $-2° < \psi < 2°$ than the rest (Figure 4), indicating only slightly preferred orientation, if any, along the surface of the samples for this crystalline phase.

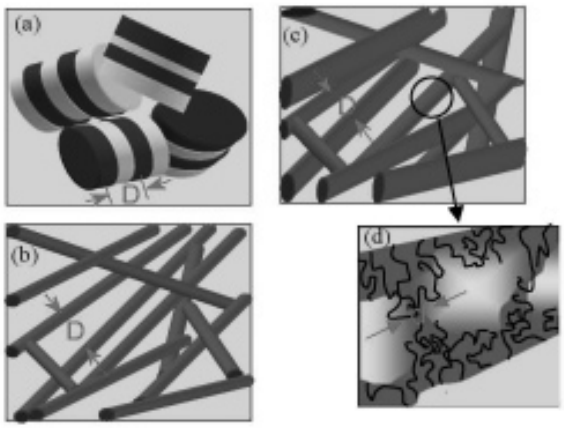


***Fig. 3*** *Various schemes to explain the morphology of the PEMs. (a) stacking disks model, (b) interconnected flexible circular cylinder model, and (c) interconnected flexible eelipsoidal cylinder (FEC) model. In all cases, the grey represents hydrophobic domains (presumably polymer backbones) and the black represents hydrophilic domains (presumably polymer side-chains and water). The average inter-domain spacing at the crystalline phase, D, yields the crystalline peak. (d) The zoom-in of the hydrophilic domains proposed with the FEC model where hydrophilic side-chains (polystyrene sulfonic acid groups) are depicted as black curves sequestering the hydrophobic-water interface and extending into the water channels. The shading represents the SLD, which is proposed to change gradually from side-chain-rich regions (dark) to water (i.e., $D_2O$)-rich ionomers (light) with a decay length of ξ (see text) and the average distance among ionomers is d, as described in T-S model.*

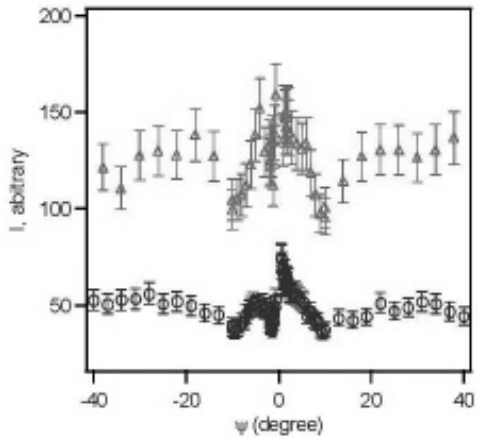


***Fig. 4*** *Rocking curves of PEM-19 (circles) and PEM-32 (triangles) as a function of sample angle (ψ) at the first order Bragg's peak (crystalline peak).*

In conclusion, the proposed compact FEC with T-S model is able to fit the SANS data nicely in the *q* range from 0.005 to 0.4 $Å^{-1}$ and describes the structure rationally over a large range of length scales. To the best of our knowledge, such agreement between SANS data and model over two decades of *q* values had never been reported previously. Moreover, since only minimal preferential orientation is found along the surface of the film, the worm-like water channels orient more or less isotropically, indicating that the solution casting does not create a situation that defeats the desired property for PEM used in FC, where high proton conductivity is through the film.

### References


[1] Norsten, T. B.; Guiver, M. D.; Murphy, J.; Astill, T.; Navessin, T.; Holdcroft, S.; Frankamp, B.L.; Rotello, V. M.; Ding, J. Adv. Funct. Mat. 2006, 16:1814-1822.

[2] Kim, M.-H.; Glinka, J. C.; Grot, S. A.; Grot, W. G. Macromolecules 2006, 39:4775-4787.

[3] Mauritz, K. A.; Moore, R. B. Chem. Rev. 2004, 104:4535-4585.

[4] Gebel, G.; Diat, O. Fuel Cells 2005, 5:261-276.

[5] Rubatat, L.; Shi, Z.; Diat, O.; Holdcroft, S.; Frisken, B. J. Macromolecules 2006, 39:720-730.

[6] Kim, J.; Kim, B.; Jung, B. J. Membr. Sci. 2002, 207:129-137.

[7] Gierke, T. D.; Munn, G. E.; Wilson, F. C. J. Polym. Sci.: Polym. Phys. Ed. 1981, 19:1687-1704.

[8] Fujimura, M.; Hashimoto, T.; Kawai H. Macromolecules 1981, 14:1309-1315.

[9] Dreyfus B.; Gebel, G.; Aldebert, P.; Pineri, M.; Escoubes, M.; Thomas, M. J. Phys. (France) 1990, 51:1341-1354.

[10] Teubner, M.; Strey, R. J. Chem. Phys. 1987, 87:3195-3200.

[11] Debye, P.; Anderson, H. R.; Brumberger, H. J. Appl. Phys. 1957, 28:679-683.

[12] Chen, W.-R.; Butler, P. D.; Magid L. J. Langmuir 2006, 22:6539-6548.

[13] Rosenfeld, Y. Phys. Rev. A 1990, 42:5978-5989.

# Characterization of Biocompatible Thin Films Using Neutron Reflectometry

**W. Feng [1], M-P. Nieh [2], S. Zhu [1], J.L. Brash [1], T.A. Harroun [3], and J. Katsaras [2]**

[1] Department of Chemical Engineering and School of Biomedical Engineering, McMaster University, Hamilton, ON, Canada L8P 4L7

[2] Canadian Neutron Beam Centre, National Research Council, Chalk River Laboratories, Chalk River, ON, Canada K0J 1J0

[3] Department of Physics, Brock University, St. Catharines, ON, Canada L2S 3A1

## Introduction

The development of surfaces that prevent nonspecific protein adsorption is important for many biomedical and biotechnology applications including biomaterials, biochips, and biosensors. For this purpose, the modification of biointerfaces with poly(ethylene oxide) (PEO) or with polymers based on phosphorylcholine (PC) has been found to be effective. The mechanisms of PEO- and PC-mediated protein resistance are presently not clear, but it is recognized that polymer chain length, graft density, and the structural arrangement of water molecules associated with the PEO- and PC containing layers are important factors in determining the interactions of the surface with proteins. Neutron reflectometry (NR) is nondestructive and powerful for the study of polymer-solvent interactions under a variety of conditions. Using NR, the objective of the present work was to determine the thickness and volume fraction profiles of poly(oligo(ethylene glycol) methyl ether methacrylate) (poly(OEGMA)) and poly(2-methacryloyloxyethyl phosphorylcholine) (poly(MPC)) thin films grafted on silicon wafers in both the dry and wet states. Additional motivation was the capability of NR to provide information on the average number of water molecules per EO or PC residue for possible correlation to protein adsorption behavior.

## Experimental

NR measurements were performed using the C5 spectrometer. The neutron wavelength was 2.37 Å. The collimation slits were varied during the scan to ensure that the entire sample was "bathed" in neutrons as its footprint varied. Specular reflection was measured and plotted against neutron momentum transfer *Qz*. The range of *Qz* was from 0.006 to 0.2 $Å^{-1}$. Measurements were performed over three *Qz* regions, namely, 0.2–0.1, 0.1–0.04, and 0.04–0.006 $Å^{-1}$. The data were normalized using the incident beam intensity to account for variations due to slit widths and were corrected for background by setting the angle to 0.5° off specular reflection. Reflectometry experiments were carried out using samples in both the dry and wet states.

Prior to measurement in the dry state, samples were cleaned with methanol (HPLC grade) and dried over nitrogen to remove any water bound to the polymer grafts. Samples were then immediately placed in the sample cell taking care to keep the layers dry. For NR measurements in the wet state, both pure $D_2O$ and a $H_2O/D_2O$ mixture containing 8.1% $D_2O$ by volume to give a solvent of null scattering length density "null-SLD water" were employed. Following the measurement in $D_2O$, the sample cell was flushed *in situ* with methanol and dried in a nitrogen stream for 1 h. Null-SLD water was then injected into the cell. For dry samples, the path of the incident neutron beam was from air to the sample to $SiO_2$ to silicon, while in the wet condition, the incident neutron path was from the backside of the sample, i.e., silicon to $SiO_2$ to the sample to $D_2O$ (or null-SLD water). This arrangement ensures total reflection from silicon in both cases. PARRATT 32 (BENSC, Berlin) software was employed to fit the reflectivity data. In the dry state, a three-layer model was used, while a two-layer and parabolic decay model was used to fit the data in the wet state.

## Results

Figure 1 shows the SLD profiles for the dry layers. NR data were fitted to a three-layer model using the PARRATT 32 software: $SiO_2$, the initiator layer, and the polymer layer. The SLDs of Silicon, $SiO_2$, the initiator layer, and air were kept constant at the bulk values. All other parameters were allowed to vary to satisfy the minimum sum of squares criterion. The various polymer layer thicknesses are also in good agreement with the values obtained by ellipsometry. The roughness parameters show that the $SiO_2$ and initiator layers are relatively smooth. They are consistent with our previous AFM measurements.

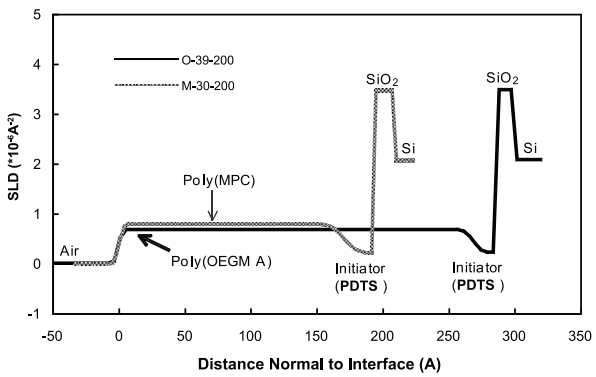


**Fig 1.** SLD profiles calculated using the best-fit data for surfaces.

The main objective of the present work was to investigate the conformational differences between poly(OEGMA) and poly(MPC) grafts in water, the medium most relevant to biomedical applications. Pure $D_2O$ was chosen since it provides good neutron contrast for poly(OEGMA) and poly(MPC). Based on these considerations, the parabolic

profile equation was used to fit the wet state data in the present work. The SLD profiles in $D_2O$ and in null-SLD water are shown in Figure 2. A noteworthy feature of the SLD profiles is the dramatic jump between the initiator layer and the innermost polymer film, suggesting that the initiator layer acts as a hydrophobic barrier, impermeable to water. From the SLD profiles, the polymer volume fraction as a function of distance through the film can be calculated. The polymer volume fraction profiles in $D_2O$ for all the surfaces are shown in Figure 3. It is difficult to compare quantitatively the swelling behavior of poly(OEGMA) and poly(MPC) brushes in water because the polymer chains have different molecular distributions and graft densities. However, it appears that both poly(OEGMA) and poly(MPC) chains swell significantly in water, indicating strong interactions of these polymers with water.

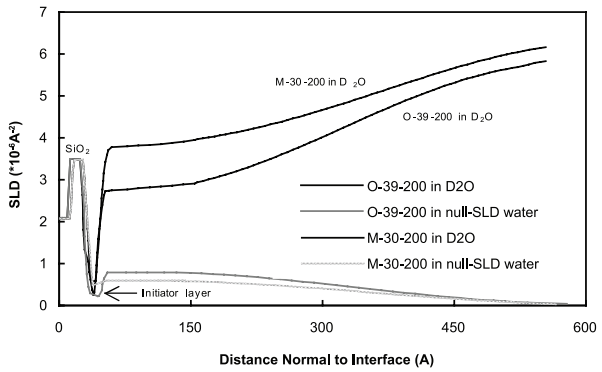


**Fig 2.** SLD profiles for surfaces in $D_2O$ and in null-SLD water.

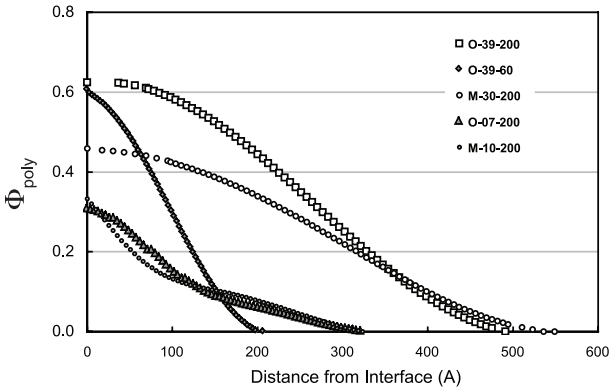


**Fig 3.** Polymer volume fraction profiles for surfaces in $D_2O$.

## Conclusion

We investigated the structures of grafted poly(OEGMA) and poly(MPC) layers on silicon substrates (dry and wet state) using neutron reflectometry. For the dry surfaces, estimates of thickness and roughness from neutron reflectometry data are consistent with ellipsometry and AFM data, respectively. In the wet state, the best-fit NR data for the surfaces in $D_2O$ and null-SLD water are in agreement. The parabolic model, with a stretched exponent, adequately describes the polymer fraction in the layer as a function of distance from the surface for both high and low graft densities. From estimates of the average number of water molecules per EO or PC moiety, it appears that the "water barrier" to protein adsorption is provided mainly by water in the bound state.

## Publication

Wei Feng, Mu-Ping Nieh, Shiping Zhu, John L. Brash, Thad A. Harroun, and John Katsaras. Characterization of biocompatible acrylate polymer brushes bearing oligo(ethylene glycol) and phosphorylcholine side chains in water by neutron Reflectometry. Biointerphases. 2:34-43, 2007.

# Polarised Neutron Reflectometry Measurements on a $YBa_2Cu_3O_7$ / $La_{2/3}Ca_{1/3}MnO_3$ Superlattice at Different Positions of the Hysteresis Loop

**J. Hoppler [1,2], H. Fritzsche [3], J. Stahn [2], Ch. Niedermayer [2], V.K.Malik [1], A.Drew [1], G. Cristiani [4], H.-U. Habermeier [4], B. Keimer [4], and C. Bernhard [1]**

[1] Department of Physics and Fribourg Center for Nano Materials, University of Fribourg, Fribourg, Switzerland CH-1700

[2] Laboratory for Neutron Scattering, Swiss Federal Institute of Technology, Zurich and Paul Scherrer Institute, Villigen, Switzerland CH-5232

[3] Canadian Neutron Beam Centre, National Research Council, Chalk River Laboratories, Chalk River, ON, Canada K0J 1J0

[4] Max-Plank Institute for Solid State Research, Stuttgart, Germany D-70569

Polarised neutron reflectometry (PNR) measurements have been used to determine the magnetisation reversing process of a superlattice with 8 $YBa_2Cu_3O_7$ (256 Å) / $La_{2/3}Ca_{1/3}MnO_3$ (256 Å) double layers when driving a hysteresis loop from $H_{appl}$ = –7 T to +7 T at T = 5 K. Due to the experimental set-up, only one branch of the hysteresis loop was accessible with the neutrons while a sample magnetisation in both direction was possible: Any zero field point in the neutron flight path would depolarise them, which limits in case of a fixed guide field and a fixed polariser the accessible field range to fields in only one direction. Additional limitations can occur if the stray fields of the magnet become larger than the guide field, leading to zero field points in the neutron flight path.

In our case, we needed access to a very broad field range, as a high magnetic field of about 7 T is needed to saturate the ferromagnetic layers and as the coercive field of Hcoerc = 0.0282 T is relatively small. We used a guide field installed from the polariser to the magnet coils, which compensated the stray field of the magnet in the case of small applied fields ($H_{appl}$ < 0.1 T). In the case of larger fields ($H_{appl}$ ≥ 0.1 T), a different set-up was used: The neutrons were kept polarised by the stray field of the magnet, which needed to be along the same direction as the guide field in the small-field set-up. This means the accessible field direction at the sample position was opposite to the accessible field direction in the small-field set-up. In the large-field set-up, the neutrons were kept polarised within the cryomagnet by driving the two helmholtz coils in asymmetric mode (different currents in the two coils) to avoid any zero magnetic field point in the neutron flight path. Due to this field arrangement, the neutrons performed a spin turn of π on their way through the magnet to the sample position [1]. This large-field set-up could not be used for small fields because the guide field to turn the neutron spin on the way through the magnet becomes too small. Therefore, the measurements presented here were performed at two sides of the hysteresis loop. The sample was first cooled to 5 K in zero field and then saturated in a magnetic field of $H_{appl}$ = +7 T. The reversing process has then been investigated in the negative field range to fields down to -0.053 T in the small-field set-up. After a saturation at -7 T, measurements at increasing field strengths from +0.1 T to +6 T have been performed to access the larger field strengths of the hysteresis loop in the high-field set-up. Hysteresis effects have then been investigated at the same applied fields after the saturation in +7 T. One additional measurement was performed at +0.008 T in order to get an insight in the magnetic profile almost in remanence.

The magnetisation reversed mainly between $H_{appl}$ = –0.023 T and -0.033 T which corresponds well to the macroscopically measured coercive field of $H_{coerc}$ = –0.0282 T. During the reversing process, no additional Bragg peaks appeared and no double-step edge of total reflection was observed (see Figure 1). The first observation excludes the possibility of single layers reversing their magnetisation one after the other, while a uniform rotation of the layer magnetisation or of large magnetic domains as described in [2] could be excluded by the latter observation.

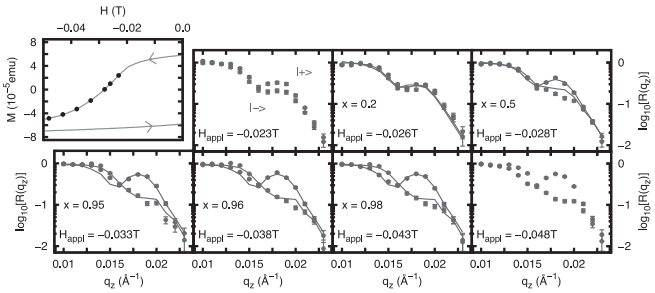


**Fig. 1** *Top left: Hysteresis loop as measured by macroscopic magetometry measurements. The black dots are the points where the reflectivity curves shown in the rest of the figure have been taken. Rest: Reflectivity curves measured at different magnetic fields showing the reversion of the magnetisation. The Reflectivity curves measured in the range of $H_{appl}$ = –0.023 T to $H_{appl}$ = –0.048 T could be reproduced with Equation 1. The dots with error bars show the measurements while the lines show the linear combination.*

Theoretical reflectivity curves from model magnetic field profiles were calculated and compared with the measurements. No matching field profile was found for the measurements with an applied field in the range of $H_{appl}$ = –0.026 T to -0.043 T where the magnetisation reversion mainly takes place, even though it is possible in this field range to reproduce the measurements with a linear combination of the curves measured at -0.023T and -0.048T with the formula:

1). $$R^{+/-} = (1-x)\,R^{+/-}_{-0.023T} + x\cdot R^{+/-}_{-0.048T}.$$

Here $R^+$ and $R^-$ indicate the reflectivities for spin up and spin down neutrons, respectively (Figure 1). The representation of the transition from $H_{appl}$ = –0.023 T to –0.048 T as a linear combination is a strong indication that there are large magnetic domains reversing their magnetisation one after the other. These domains scatter incoherently between each other as no average field profile could be found when modelling. Therefore these domains must be larger than the lateral neutron coherence length of about 100 µm.

At higher fields, theoretical models were found to reproduce the measured data reasonably well. Figure 2 shows reflectivity curves taken at 0.1 T after saturation in -7 T and +7 T, respectively and at 0.4 T after saturation in -7 T. For all curves, very similar models were found with a magnetisation of about 0.61 T in $La_{2/3}Ca_{1/3}MnO_3$. After saturating in -7 T, a 12.5 Å thick $La_{2/3}Ca_{1/3}MnO_3$ layer at the interfaces contains an anti-parallel oriented magnetisation of -0.043T at $H_{appl}$ = 0.1 T and no magnetisation at $H_{appl}$ = 0.4 T. After saturation in +7 T, the nonmagnetic layer persists at $H_{appl}$ = 0.1 T, even with a thickness of 15 Å.

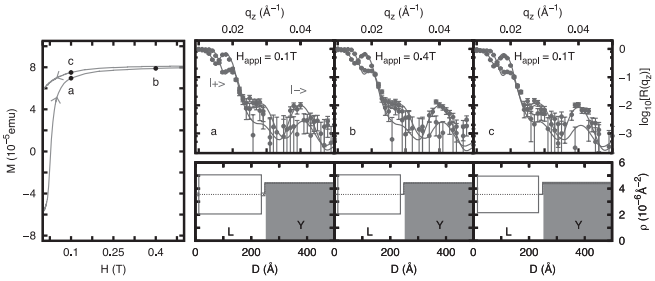


***Fig. 2*** *Left: Hysteresis loop measured with macroscopic magnetometry with the field positions where PNR curves were measured. (a,b) Reflectivity curves as measured at $H_{appl}$ = 0.1 T and 0.4 T after saturation in -7 T compared to the calculated models. (c) Reflectivity curves as measured at $H_{appl}$ = 0.1 T after saturation in +7 T compared to the calculated model. Models: Depth profile of the potential seen by the $|-\rangle$ and $|+\rangle$ neutrons (grey and black). The models contain a reduced density for the two top layers.*

After saturation in +7 T, a small anti-parallel moment of -0.022 T was observed in $YBa_2Cu_3O_7$. The anti-parallel moment in $YBa_2Cu_3O_7$ could be resulting from pinned vortices that developed at high fields in order to expel the external field of the superconductor. The nonmagnetic or anti-parallel oriented layer at the $La_{2/3}Ca_{1/3}MnO_3$ interfaces has been described in earlier publications as a possible magnetisation profile at small applied fields of a few 10 mT [3].

### References


[1] H. Fritzsche, Rev. Sci. Instrum. **76**:115104 (2005)

[2] F. Radu et al., Phys. Rev. B **71**:214423 (2005)

[3] J. Stahn et al., Phys. Rev. B **71**:145059(R) (2005)

# Neutron Reflectometry Study of Hydrogen Desorption in Destabilized MgAl Alloy Thin Films

**H. Fritzsche [1], M. Saoudi [1], J. Haagsma [2], C. Ophus [2], E. Luber [2], C. T. Harrower [2], and D. Mitlin [2]**

[1] Canadian Neutron Beam Centre, National Research Council, Chalk River Laboratories, Chalk River, ON, Canada K0J 1J0

[2] Chemical and Materials Engineering, University of Alberta and National Institute for Nanotechnology, National Research Council Canada, Edmonton, AB T6G 2H7

Magnesium-based hydrogen storage is emerging as one of the most viable options for automotive applications since both elemental magnesium and magnesium hydrides are relatively inexpensive and $MgH_2$ holds 7.6 wt% hydrogen. The critical problem with magnesium-based storage materials is their unacceptably high charging and discharging temperature due to a relatively large negative heat of hydride formation. Mostly, approaches to modify the temperature have consisted of creating nanocrystalline hydrides by using high-energy ball milling and catalysts. Only recently, cosputtering of Mg and Al has been used to destabilize the Mg matrix and create nanocrystalline and amorphous films.

The films were cosputtered onto a Si(100) substrate with a native oxide layer of about 1 nm thickness. The MgAl films had a thickness of about 50 nm and were covered with a 10 nm thick Pd layer in order to facilitate the hydrogen uptake. The films were absorbed with hydrogen in a dedicated high-pressure furnace at 430 K for 20 h at 6.8 MPa.

The neutron reflectometry experiments were performed on the newly commissioned D3 reflectometer. Figure 1 shows the experimental data for a $Mg_{0.7}Al_{0.3}H_y$ film (a) before hydrogen absorption, (b) after hydrogen absorption (y = 1.1) and (c) after complete hydrogen desorption at 448 K (y = 0). The fits, displayed as solid lines, were calculated using the software PARRATT32. The changes in the film structure due to hydrogen uptake can be best visualized by plotting the scattering length density (SLD) profile, i.e. the SLD along the surface normal z of the film. The SLD profiles corresponding to the fits are shown in Figure 1 as insets. By comparing the SLD profiles before and after hydrogen absorption, you can easily conclude an expansion of about 20% for both, the Pd and MgAl layer. The amount of hydrogen absorbed into the MgAl layer can be determined from the decrease in the SLD of the unsorbed film due to the negative scattering length of the hydrogen [1]. From the SLD values of Figure 1b we can calculate a hydrogen content of 110 at.% or 4.1 wt%, respectively, in the $Mg_{0.7}Al_{0.3}$ film. At a temperature of 448 K (Fig. 1c) the hydrogen is completely desorbed.

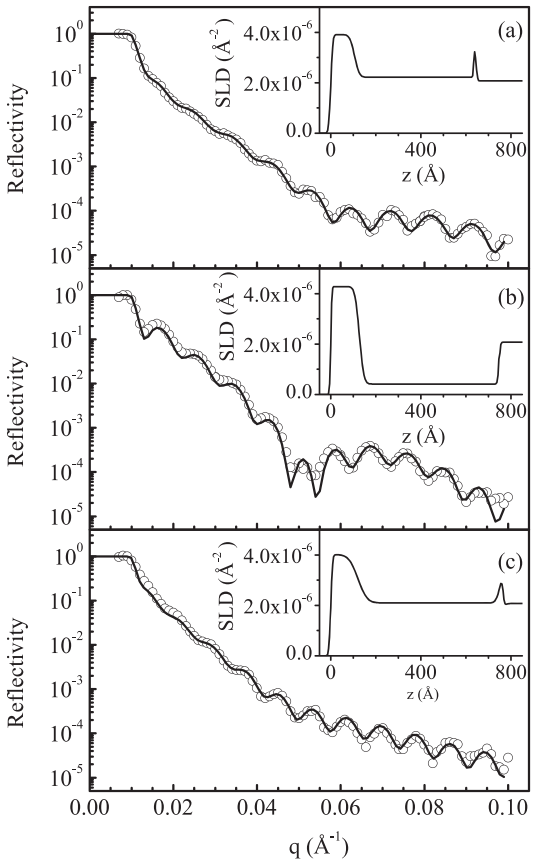


**Fig. 1** Reflectivity curve of a Pd-covered $Mg_{0.7}Al_{0.3}H_y$ thin film on a Si substrate (a) before hydrogen absorption (y = 0) measured at 295 K, (b) after hydrogen absorption (y = 1.1) measured at 295 K, and (c) after hydrogen desorption measured at 448 K (y = 0). The open circles represent experimental data, the solid lines represent fits, and the insets show the corresponding SLD profile.

### References

[1] H. Fritzsche, M. Saoudi, J. Haagsma, C. Ophus, E. Luber, C. T. Harrower, and D. Mitlin, Appl. Phys. Lett. 92, 121917 (2008)

# Index of Authors

NRC Canadian Neutron Beam Centre
ANNUAL REPORT 2007
Centre canadien de faisceaux de neutrons
RAPPORT ANNUEL

http://neutron.nrc-cnrc.gc.ca